NTNU
Norwegian University of
Science and Technology

Stress analysis of a monopile foundation under the hammering loads

Rui Xu

Wind Energy
Submission date: July 2017
Supervisor: Zhen Gao, IMT
Co-supervisor: Eliz-Mari Lourens, Delft University of Technology

Norwegian University of Science and Technology
Department of Marine Technology

Structural analysis of the gripper device during the hammering process of an offshore wind turbine monopile

Rui Xu

July 2017

MASTER THESIS

Delft University of Technology &

Norwegian University of Science and Technology

Supervisor 1: Professor Andrei Metrikine

Supervisor 2: Professor Zhen Gao

Supervisor 3: Dr. Zhiyu Jiang

Supervisor 4: Dr. Peter Meijers

Abstract

The installation of monopile is a very important process in offshore wind turbine construction. During the monopile being driven down by hydraulic hammer, huge energy transfers from hammer to pile, which may cause monopile inclination. In order to keep the monopile steady in horizontal direction, a gripper device is applied between the monopile and installation vessel. The gripper contacts with monopile by four hydraulic cylinders. In the most time, the hydraulic cylinder contacts with the smooth surface on the monopile, and it only bears axial load. While, the monopile is welded piece by piece, its surface is not perfectly smooth due to welds. The welds collide with the hydraulic cylinder and induce a vertical force on the hydraulic cylinder, which may damage the hydraulic cylinder.

This thesis analyzes the installation of monopile by HLV and hydraulic hammer. It presents modelling and calculation for the collision problem between welds and hydraulic cylinder. A finite element model for monopile, welds and gripper is built in Abaqus CAE. The external loads including hammer load, soil resistance and cylinder force is obtained from hand calculation or previous thesis and then applied into the finite element model. The effects of changing different parameters (such as welds thickness, hammer energy, initial penetration depth etc.) is carried out for analyzing the method for reducing the gripper stress during colliding.

Preface

This thesis presents the work done by Rui Xu for the Master thesis, in order to obtain the MSc in wind energy degree in NTNU and MSc in offshore engineering and dredging in TU Delft. The work was carried out during spring 2017, in Trondheim. The supervisor was Prof. Andrei Metrikine (TU Delft), Prof. Zhen Gao (NTNU), Dr. Zhiyu Jiang (NTNU), Dr. Peter Maijers (TU Delft.)

Acknowledgements

I want to give my sincere thinks to my master thesis committee: Prof. Andrei Metrikine, Prof. Zhen Gao, Dr. Zhiyu Jiang and Dr. Peter Maijers. I gain a lot from Andrei's deep knowledge, experience and great enthusiasm and discipline in scientific research. Gao always uses his wide knowledge, thorough mind and patience to guide me into the right path. Zhiyu is always helpful, and, with his genius thought, he can always point out what makes my thesis better. I am grateful for Peter who gives me great comment on my master thesis and follows my work.

I am also grateful for Wilson Guachamin Acero for the excellent discussion about soil pile interaction. I appreciate previous supervisor Prof. Eliz-Mari Lourens' valuable discussion and comments for my thesis.

Finally, I want to give my deepest thanks to my family in China and my girlfriend Jingyi for the great support on my study and life.

Rui Xu
July 2017
Trondheim, Norway

Contents

List of Figures

List of Tables

List of Symbol

Roman

A_0	Cross section area of the structure
A_{pile}	Acceleration of pile
A_f	Total area where friction occurs
$A_{f,i}$	Inner friction area
A_t	Cross sectional area of the pile tip
$A_{t,s}$	End bearing area of inner soil
c	Cohesion
C_0	Stress wave propagate velocity
d	Penetration depth
	Length between exhaust ports and anvil
ds	Infinitesimal distance
D	Pile diameter
D_i	Inner diameter of pile
D_{rotor}	Diameter of the wind turbine
e	Coefficient of restitution
E_e	Explosive energy
E_k	Kinematic energy
E_T	Total energy transferred to anvil
f	Unit skin friction capacity
$f_{z,c}$	Friction coefficient for clay
$f_{z,s}$	Friction coefficient in sand
F	Explosive force
F_{imp}	Impact force on pile due to hammering
$F_{h,max}$	Maximun force on anvil
F_{yield}	Yield force

G_{pile}	Gravity of the pile
h	Lifted height of ram
J	Dimensionless empirical constant
k	Initial modulus of subgrade reaction
K	Coefficient of lateral earth pressure
L_{pile}	Pile length
M_{pile}	Mass of pile
N	Normal force
N_q	Dimensionless bearing capacity factor
p	Total pressure
	Lateral resistance
p_0	Pore pressure
$p^{'}$	Effective pressure
p_u	Ultimate unit lateral bearing capacity of soft clay
P	Power of the wind turbine
q	Unit end bearing coefficient
Q_f	Friction resistance on the pile lateral surface
$Q_{f,i}$	Inner friction
Q_t	Tip resistance at the pile tip
$Q_{t,s}$	Bearing capacity of inner soil
R_s	Total soil resistance along the pile
s_u	Undrained shear strength
S_{pile}	Pile movement
t_e	Time when the force on anvil is decreased to zero
T	Friction force
V_{pile}	Velocity of pile
W_R	Weight of ram
X	Depth below soil surface
XR	Depth below soil surface to bottom of reduced resistancezone

y	Lateral deflection
z_{end}	Stop point of one penetration
z_{start}	Starting point of one penetration

Greek

α	Dimensionless factor
	Angle of slope
γ	Effective unit weight of soil
δ	Angle of internal friction(or friction angle)
δ	Friction angle between sand and pile wall
κ	Reduction factor for flexural buckling
λ	Reduced slenderness ratio
ξ	Efficiency of hammer
σ'_0	Average effective stress
σ'_1	Larger normal effective stress
σ'_3	Smaller normal effective stress
σ'	Effective normal stress
σ'_v	Effective overburden pressure at the point of calculation
σ_{xx}	Effective stress
σ'_{xx}	Horizontal effective stress
τ_f	Critical shear stress
ϕ	Friction angle
ψ	Dilatancy angle

List of Acronym

CPHP	No new energy policies and higher fossil fuel prices
DP	Dynamic position EU
European Union	
EWEA	European Wind Energy Association
HLV	Heavy lift vessel
HRRP	High share of renewable energy and lower fossil fuel prices
OWEZ	Offshore Windfarm Egmond aan Ze
RNA	Rotor nacelle assembly
SPIV	Self-propelled installa-tion vessel

Chapter 1

Introduction

1.1 Introduction to wind energy

With abundant and accessible energy resource, wind energy industry has a large potential to become a reliable energy resource and contributes large proportion to the total energy production. The installed power capacity in Europe from 2004 to 2014 is shown in Figure 1.1. It can be seen that over the past 15 years, the wind energy in Europe has experienced a remarkable growth. In 2000, wind energy met 2.4% of the EU's electricity demand thanks to 12.9 GW of installed capacity. By 2014, 128.8 GW of wind capacity had been installed, enough to meet 10.2% of the EU's electricity demand. The scalability of wind energy has helped it emerge as a viable alternative to fossil fuels for power gen eration. During the 10 years (2004-2014), the wind energy has grown approximately four times. This trend is set to continue according to the EWEA's aim, which wind 2 energy should account for at least 43-45% of all renewable energy produced by 2030 [7].

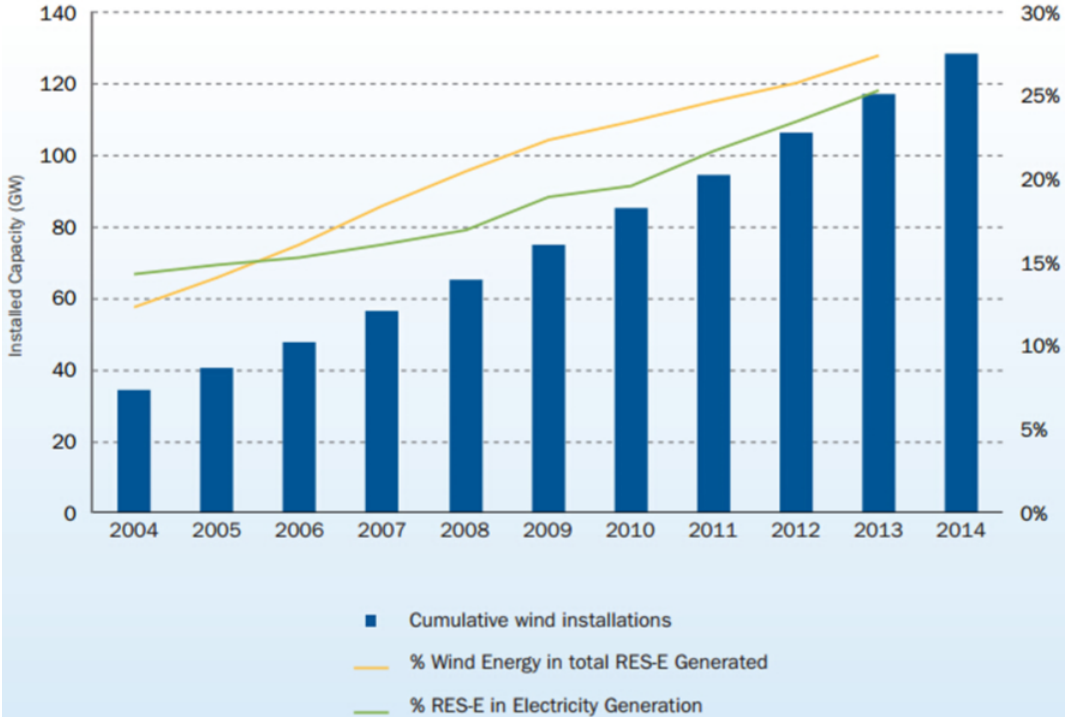

Figure 1.1: Total installed power capacity in EU

1.2 Offshore wind energy

The high quality of wind resource (large wind speed, low turbulence) and ideal location (without causing aesthetics and noise problem) in offshore area makes offshore wind energy become more and more popular. The offshore wind power has been rapidly growing in recent years, Figure 1.2. The cumulative offshore wind installation in 2015 is 11 GW. According to EWEA's aim, it will be 40 GW offshore wind installation in 2020, which is approximately four times of cumulative offshore wind installation in 2015.

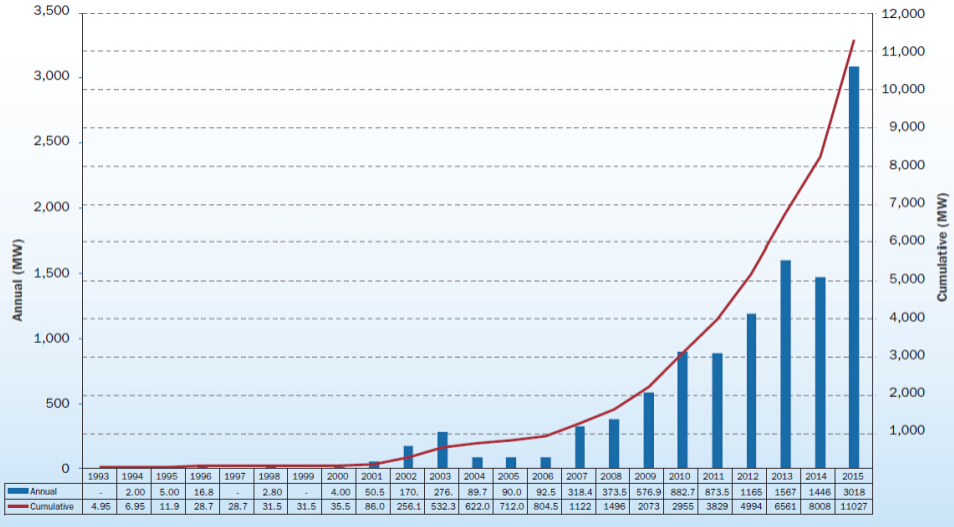

	1993	1994	1995	1996	1997	1998	1999	2000	2001	2002	2003	2004	2005	2006	2007	2008	2009	2010	2011	2012	2013	2014	2015
Annual	-	2.00	5.00	16.8	-	2.80	-	4.00	50.5	170.	276.	89.7	90.0	92.5	318.4	373.5	576.9	882.7	873.5	1165	1567	1446	3018
Cumulative	4.95	6.95	11.9	28.7	28.7	31.5	31.5	35.5	86.0	256.1	532.3	622.0	712.0	804.5	1122	1496	2073	2955	3829	4994	6561	8008	11027

Figure 1.2: The cumulative offshore wind installation

1.2.1 Foundation

There are mainly two kinds of offshore wind turbine foundation: bottom founded and floating structure, Figure 1.3 and Figure 1.4 respectively. The offshore foundation can be further categorized according to [1].

Figure 1.3: Bottom founded structure [1]

Monopile: The monopile support structure is a simple design by which the tower is supported by the monopile, either directly or through a transition piece, which is a transitional section between the tower and the monopile. The monopile continues down into the soil and the structure is made of steel tubes. The appropriate water depth for this structure ranging from 0 to 25

metres.

Jacket: The jacket structure can be represented as forth structure in Figure 1.3. Jacket structure normally has three or four legs connected by K- or X- brace. This structure is make of steel tubes. The tower of wind turbine is located in center of the jacket structure. This type of structures are well suited for sites with water depth ranging from 20 to 50 metres.

Gravity based: The gravity based structure is made of concrete. The foundation has very large density which make it able to stand on the seabed stably. The decommissioning of gravity based foundation is much more difficult than steel foundation, so it is normally less used than steel foundation. The appropriate water depth of gravity based foundation is from 0 to 25 metres.

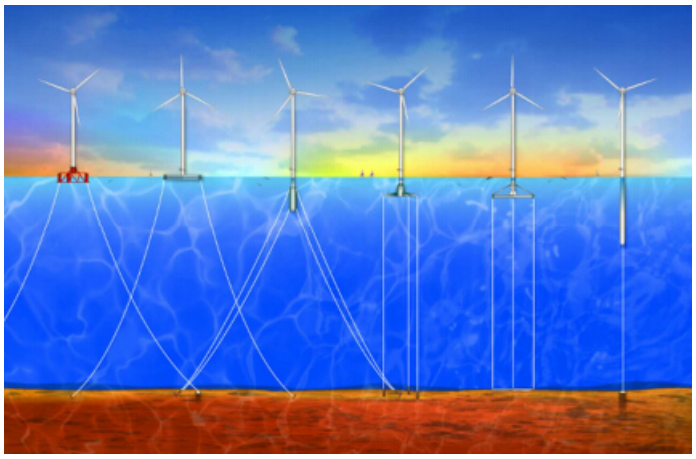

Figure 1.4: Floating structure [1]

Floaters: The floater is basically a floater kept in position by mooring chains and anchors. In addition to keeping the floater in place, the chains have the advantage that they contribute to dampen the motions of the floater. The installation is simple since the structure can be towed to the site and then be connected by the chains to the anchors. The anchors can be fluke anchors, drag-in plate anchors, pile anchors and suction anchors, depending on the actual seabed condition. This structure is suitable for working at large water depth.

Tension leg platform: In Figure 1.4, the forth, fifth and sixth structure are all tension leg plat-

forms. This structure has a floater submerged by means of tensioned vertical anchor legs. The base structure helps dempen the motions of the structural system. The installation is simple as the same reason for floaters. THe structure can be disconnected from the tension legs and floated to shore in case of major maintenance or repair of the wind turbine. This structure is suitable for working at large water depth.

1.2.2 Wind turbine

The wind turbine consists of rotor, nacelle and tower. The rotor rotating around its center (hub), and the gear connected with rotor rotates together with the rotor. The gear box transfers the rotation, at the same time, it convert the low speed rotation into high speed rotation, which is more suitable for the generator.

Figure 1.5: Wind turbine

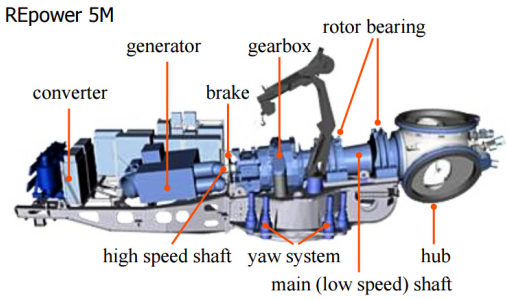

Figure 1.6: Components in nacelle

1.2.3 Challenges

Together with the advantages, the offshore wind industry should also face the challenges due to harsh environment in offshore area. The wind and wave load in offshore area is larger than on-shore area, so the structure should have better reliability. The harsh offshore environment makes wind farm construction process very costly both in time and economy. Inappropriate operation may cause bad construction condition leading to poor productivity and reliability for offshore wind turbines, even worse, damaging the installation equipment. So, an analysis in wind farm installation is very important in offshore wind farm design.

1.3 Introduction to wind turbine installation

Together with the fast grow-up demand for offshore wind energy, the offshore foundation equipment undergoes rapidly increasing in demand. These installation equipment usually has strong capability of strength and large dimension, which makes them capable for working in harsh environment and working with huge offshore structure. Meanwhile, the high performance of these equipment result in a very expensive leasing price, and the price keeps increasing due to wind farm construction moving further away from the coast.

In recent years, companies and scholars have been developing efficient methodology to lower the installation costs of offshore wind farm. Tomas Gintautas [8] adopt an updated methodology of weather window prediction using two physical model of operational vessel and equipment in SIMA. The response gives an optimized probability of operation failure, which is less than the maximum allowable probability of failure, and the two model allow 57% and 47% more operational hours during the test period. Lin Li [4] used a coupled model for monopile and installation vessel and analysis the motion and response during lowering the monopile through the wave zone down to the sea bed. The simulation found the monopile inclination during installation due to coupled motion, wind and wave dynamic loads and vessel shielding effect on monopile. It gives the maximum compression load from gripper to monopile, which corrects the monopile inclination.

This section will introduce the methodology for construction of offshore wind turbine, and then it will focus on the monopile installation, coupled motion and response of monopile and installation vessel during monopile installation. Load for correcting monopile inclination provided by hydraulic cylinder is calculated during the pile penetration. This work is done by Lin Li as a doctoral thesis.

1.4 Installation equipment

1.4.1 Vessel

The installation vessel can be categorized by: liftboats, Jack-up barges, Self-propelled installation vessels (SPIVs), heavy lift vessels (HLVs) [9]. HLVs, which include barge-shaped or semi-

submersible hulls with very high lifting capacity and do not employ a hull-elevating system, is used in this thesis. Usually this kind of vessel uses mooring or dynamically positioned (DP) system to keep itself in-place. Figure 1.7 shows a typical shape of HLVs.

Figure 1.7: HLVs (SMIT's Taklift 4)

1.4.2 Hammer

The hammer is chosen as IHC S-1200 Hydrohammer, Figure 1.8. The key figure is described as Table 1.1. This hammer has three main components: ram, anvil and sleeve. During monopile driving, the ram is lifted for 1 meter and then the dropped to the pile head. The dropping acceleration can be adjusted by hydraulic liquid in the hammer. By adjusting the dropping acceleration, the kinematic energy in the ram can vary from 120 kJ to 1200 kJ. The anvil acts like a cushion, which has a function of protection against the explosive load induced by ram impact. The sleeve fastens the monopile with the hammer and keeps the monopile-ram in a straight line.

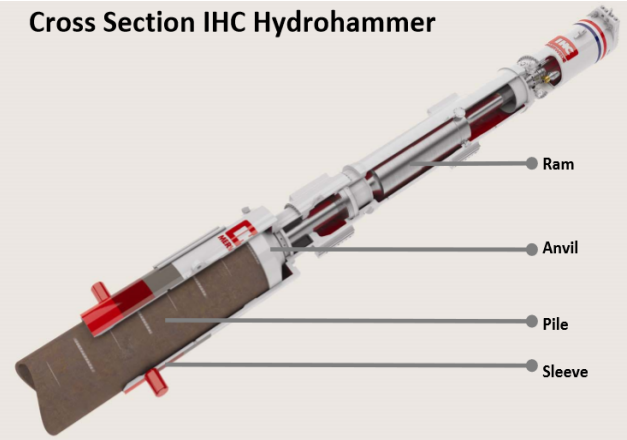

Figure 1.8: IHC S-1200 Hydrohammer

Ram weight [t]	60
Ram lift [m]	1
Ram acceleration downward [m/s^2]	2g
Ram speed at anvil [m/s]	6.33
Energy [kJ]	120-1200
Cycle rate [blow/min]	40
Contact time [ms]	4.5
Speed of shock wave in pile [m/s]	5200

Table 1.1: Key parameters of IHC S-1200 Hydrohammer

1.4.3 Gripper

A gripper device is shown in Figure 1.9. It includes a circular frame and 4 hydraulic cylinders. The cylinder contact with the monopile by a roller, which is placed at the inner end of cylinder. It can provide large compression and tension force parallel to the piston rod direction. The gripper device plays an important role during monopile lowering and driving process by correcting the inclination of monopile, avoiding huge hammer load damaging the system.

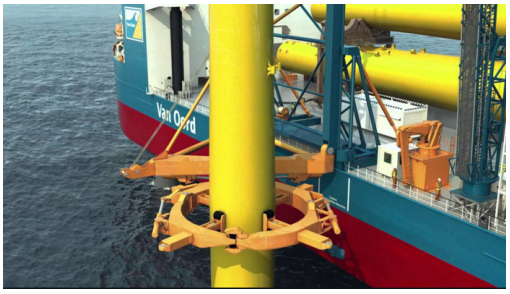

Figure 1.9: Gripper

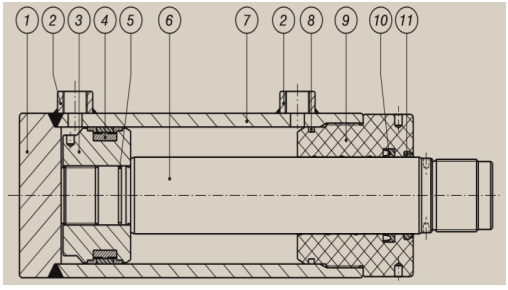

Figure 1.10: Cross-section view of a hydraulic cylinder

The hydraulic cylinder can be seen in Figure 1.9 between the circular frame and monopile. A cross-section view of the cylinder is shown in Figure 1.10. The components for this cylinder are:

1	Bottom	7	Cylinder body
2	Connection	8	O-ring
3	Piston	9	Cylinder cover
4	Piston seal	10	Piston rod seal
5	O-ring	11	Dirt wiper
6	Piston rod		

The capacity of pushing force should be taken into consideration when choosing a hydraulic cylinder for monopile installation. The maximum pushing force should be large enough so that it can bear the load caused by coupled motion of monopile and vessel. According to [10], the dimension of the chosen cylinder is shown in Table 1.2.

Table 1.2: Dimension of chosen cylinder

dimension		a rea			A/C	theoretical forces at a mechanical efficiency of 100%					
bore	piston rod	piston area	rod area	ring area	pistonarea/ringarea	pushing force			pulling force		
						100 bar	210 bar	320 bar	100 bar	210 bar	320 bar
mm	mm	cm^2	cm^2	cm^2		kN	kN	kN	kN	kN	kN
250	140	490.9	153.9	336.9	1.46	491	1031	1571	337	708	1 078

1.5 Wind farm construction methodology

1.5.1 Procurement and delivery

Procurement and delivery involves all types of equipment necessary for wind turbine installation work. It includes meteorological instruments, wind turbine components (tower, nacelle, hub, blade), electric equipment (cable, transformer). The turbines are delivered to the staging area and preparing the be assembled.

1.5.2 Assembly

Wind turbine blades and nacelles can be pre-assembled in the staging area on-shore or piece by piece assembled offshore by crane. The factor for choosing the strategy for assembly problem is making the cost minimum, which may influenced by sea states and the property of turbine components. By reducing the number of offshore lifts, the the time required by the installation

vessel will decline but the lifting capacity requirements will increase. At the extreme, a complete turbine assembly will require one lift using a heavy-lift vessel [11].

1.5.3 Wind turbine installation

After the turbines are assembled in the staging area, they are placed in installation vessels by crane. The installation vessel should be neither too empty, which causes increasing transporting times between onshore base and offshore target area, nor too full, which may causes large loads on vessel and collision between components.
The vessels should wait in harbor before the appropriate sea state for installation comes. After it sailing to the target area for offshore wind turbine, installation should begin following the process flow:

- Installation of the foundation , transition piece and scour protection;
- Installation of the turbine tower, nacelle and blade
- Installation of the inner-array cables and scour protection

1.6 Monopile installation

Monopile installation is an essential procedure in wind farm construction. The huge impact by the hydraulic hammer acting on the monopile may create unexpected damage in this system. In order to optimize the reliability and effectiveness of this procedure, analysis for the coupled monopile-vessel system and monopile driving process should be carried out.

The monopile installation procedure can be divided into three phases:

- **Up-ending:** the monopile is lifted at one end by a crane on vessel. The crane lifts the monopile totally in the air and, then, moves it to the proper location. A gripper device is used to keep the monopile stable. Another method to up-ending the monopile is first sealed the monopile and make it float on the sea. Then lifting one end of the monopile and filling water in it, the monopile will totally sink into the sea eventually. In this thesis, the first method is applied;

- **lowering:** the crane lower the monopile downward through wave zone and then to the sea bed. The monopile will penetrate the sea bed for a certain depth by self-weight. Due to wind and wave loads, the monopile and the vessel can be treated like a coupled motion system. The monopile's motion created a inclination, which makes the monopile not perfectly vertical. In most cases, the inclination during both lowering and driving phase should not exceed 0.5^o to 1^o depending on the monopile's size and driving equipment [12].

- **Driving:** after the monopile self-penetration, hydraulic hammer is placed on the top of the monopile and keep driving it to the expected depth. After penetrating a certain depth, the soil can totally support the monopile laterally, so the gripper device is usually retrieved after a certain penetration depth. There are two kinds of hammer: hydraulic hammer, which uses a ram to impulse the monopile; vibration hammer, which creates vibration on monopile. This thesis will focus on the hydraulic hammer.

Chapter 2

Problem statement

2.1 Aim and scope

During the driving phase of monopile, the welds on the monopile's surface will collide with the gripper device. In order to analyze whether the gripper is damaged in this situation, a finite element model including the monopile with welds and the gripper device is built in Abaqus. The load on the monopile and gripper, for example: hammer load, soil resistance and cylinder force, is applied on the finite element model as external loads. Then, a complete finite element model for the monopile installation is ready for calculating the stress on the gripper during colliding with welds.
The aim for each chapter is shown below:

- **Chapter 2** introduces the collision problem and the external loads on the monopile and gripper system.
- **Chapter 3** gives the theoretical background for calculating the external loads, analyzing the stress wave and theory for Abaqus modelling.
- **Chapter 4** calculates the external loads based on theory in chapter 3.
- **Chapter 5** shows how to build the model in Abaqus.
- **Chapter 6** gives several load cases for parametric study.

2.2 Introduction to problem

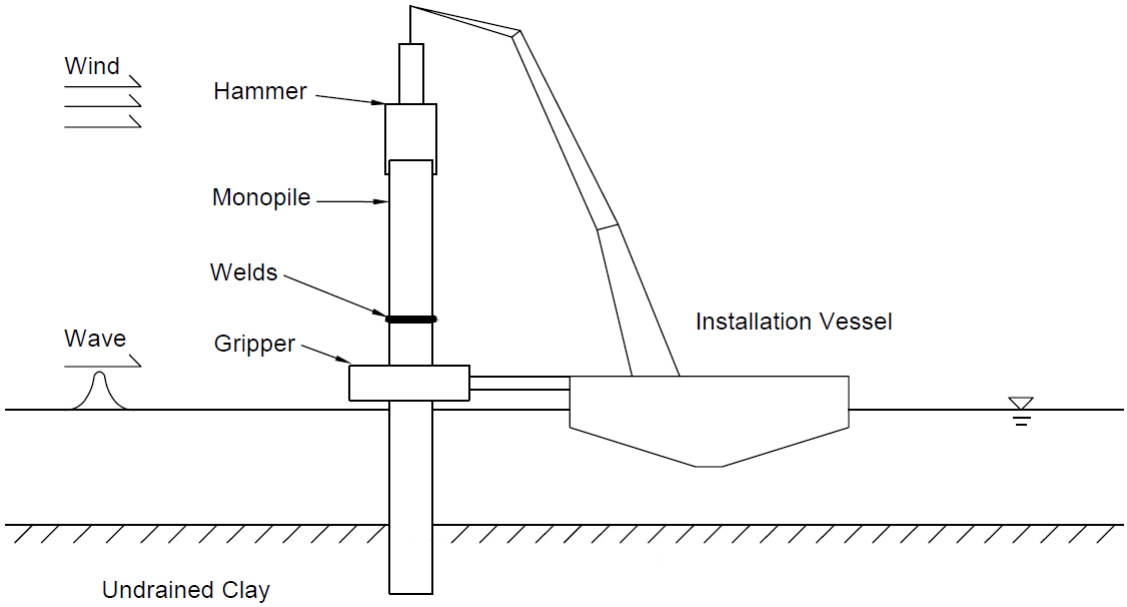

Figure 2.1: Senario of monopile installation

Among the three phases for monopile installation in chapter 1.6, the driving phase is the most dangerous phase. If the monopile has inclination, there will be a large stress on the structure. Even worse, it will cause a bad installation condition for wind turbine.

In order to correct the inclination for the monopile, a gripper device is placed between the monopile and the installation vessel, shown in Figure 2.1. The gripper will support the monopile laterally and keep the monopile steady during the driving phase. In the most cases, the gripper contacts with the smooth surface of the monopile. While, the monopile is welded piece by piece, and there is imperfection on the surface of the monopile due to welds. The welds moves down together with the monopile and it can strike the gripper. This thesis analyzes whether the collision between welds and gripper can cause damage to the structure.

The gripper device has been introduced in section 2.2.3, which contains a circular frame and four hydraulic cylinders. A close view of the hydraulic cylinder is shown in Figure 2.2. The unit for the dimension in the figure is mm. The hydraulic cylinder here contains: a simplified roller (later the difference will be compared with and without simplification of the roller), a piston, a cylinder and a piston support structure. Hydraulic liquid is filled in the room between the piston

and the cylinder to provide axial compressive force for the piston. The cylinder and the piston support structure are fixed at the right end. The hydraulic cylinder is a long and thin structure.

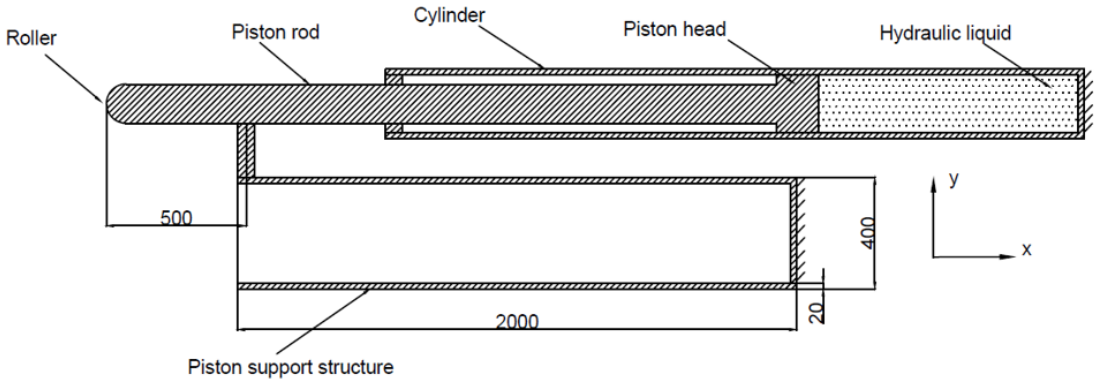

Figure 2.2: Hydraulic cylinder

A detailed view for the contact between welds and piston is shown in Figure 2.3. During lowering of the monopile, in the most case, the piston (supported by gripper) connects with the smooth monopile surface, shown in left figure of Figure 2.3. A pre-compression load is applied by the piston in order to hold the monopile standing still. In this case, the contact force (represented by CF in the figure) works in the x direction. However, the surface of monopile is not perfectly smooth because it is welded piece by piece. Welds acts like a protrusion on the monopile's surface. Together with the the downward motion of monopile, the welds will strike the piston, which is a totally different situation from contact between piston and smooth monopile' surface, shown in right figure of Figure 2.3. When the welds strike the roller, the contact force (CF) changes direction. The contact force should always stay normal to the contact surface, so it will induce a vertical force on the piston. The piston has a large stiffness along axial direction, but relatively low stiffness along transverse direction due to slenderness. So, there is a possibility that the strike from welds to piston damages the gripper device. The stress on this system should be analyzed to check whether or not the piston and hydraulic cylinder can bear the strike load when it collides with welds on monopile.

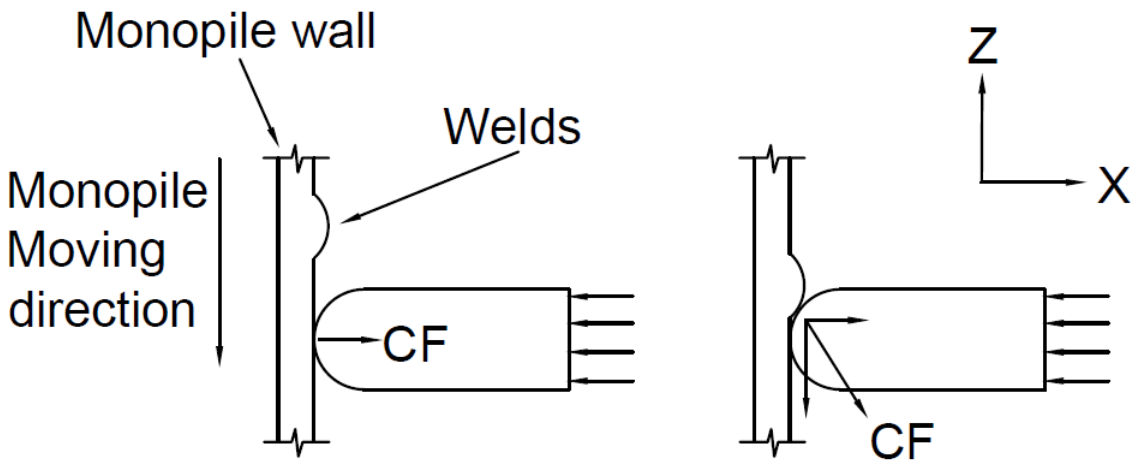

Figure 2.3: Close view of monopile contact with piston

2.3 Method

The procedure to solve the monopile installation procedure is shown in Figure 2.4. At first, the external loads, which is hammer loads, soil resistance and cylinder force, should be estimated by hand calculation or by literatural review. Then, insert these external force to the monopile gripper system and build a finite element model in Abaqus. The monopile motion, the gripper response and maximum stress can be calculated by the Abaqus model.

The external loads is defined as:

- **Simplified soil resistance:** the soil resistance on the submerged area of monopile is changing depending on the penetration depth. It is very important for calculating the motion of monopile.
- **Simplified hammer load:** the hammer load on the top of the monopile for different hammer drop energy and soil resistance should be estimated. It is very important for calculating the motion of monopile.
- **Cylinder force:** the compressive load provided by hydraulic cylinder induced by relative motion between monopile and installation vessel. The wind and wave can induce motion of monopile and installation vessel. While the monopile is hanging by the lift string

and gripper is working, the motion of monopile and installation vessel are coupled. The relative motion between monopile and installation vessel will induce a time varying compressive force on the connector (gripper) between them, which is called cylinder force.

- **Note:** The wind and wave loads acting directly on the monopile is very small when compared with other external loads, so they can be neglected.

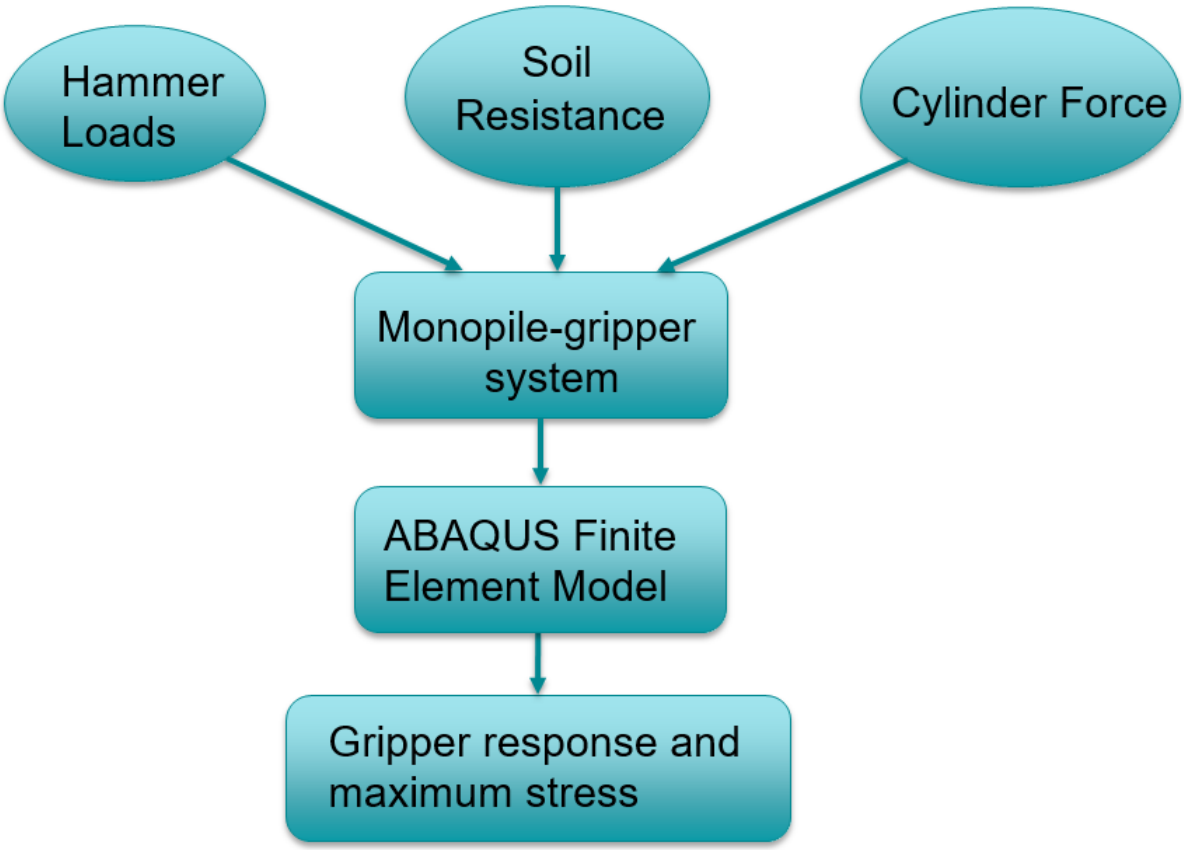

Figure 2.4: Procedure for solving the monopile installation problem

2.4 Previous study

Nahian, Nishat Al has built a finite element model (Figure 2.5) for analyzing the stress in gripper device during hammering process. In this model, the monopile is simplified as a piece of monopile wall, which contains welds. The initial condition adding to the monopile is set as constant downward velocity. The boundary condition for the cylinder is fixed at the right end. The normal behavior for all contact pair is set as "hard" contact. There is no friction behavior

between the roller and monopile, but, for the contact pair between piston and cylinder, friction exists.

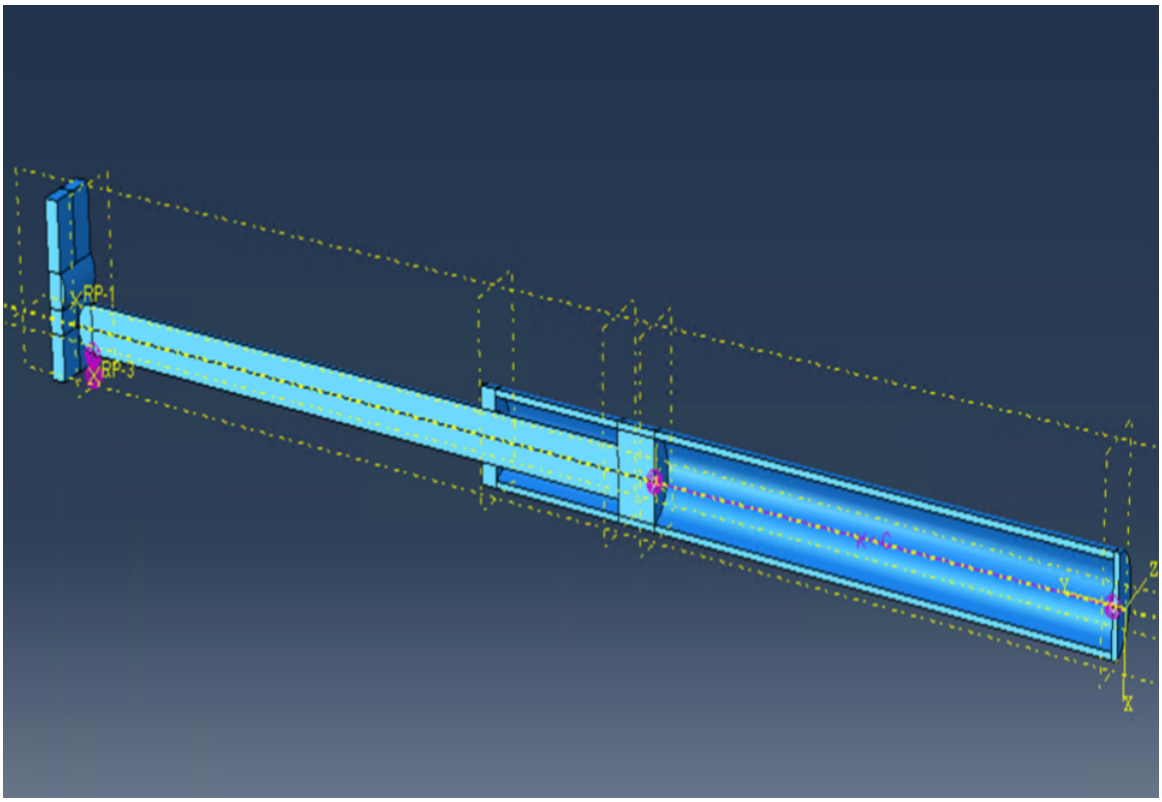

Figure 2.5: Finite element model by Nishat [2]

At first, the point which supports the spring near the monopile (K1) has a roller boundary condition. Some cases are carried out: changing the monopile speed for 0.4, 0.6, 0.8 m/s; changing the welds capping for 10 mm, 20 mm; changing the roller size for 50 mm, 70 mm; changing the spring representing for hydraulic liquid. The work he has done shows that the speed of the Monopile does not affect the result of the analysis that much. With roller boundary condition at the end of the spring K1, changing welds height(capping) from 20 mm to 10 mm, decreases max stress both at piston and seal by around 4% while stress at roller remains same. Decreasing the roller size increases the stress concentration at the roller. Figure 2.6 shows the stress at the cylinder seam during monopile moving downward when K1 is supported by roller. The maximum stress is similar after changing the capping size. The difference is that, due to large welds capping, the contact duration for blue curve (capping 20 mm) is much longer than the red curve

(capping 10 mm).

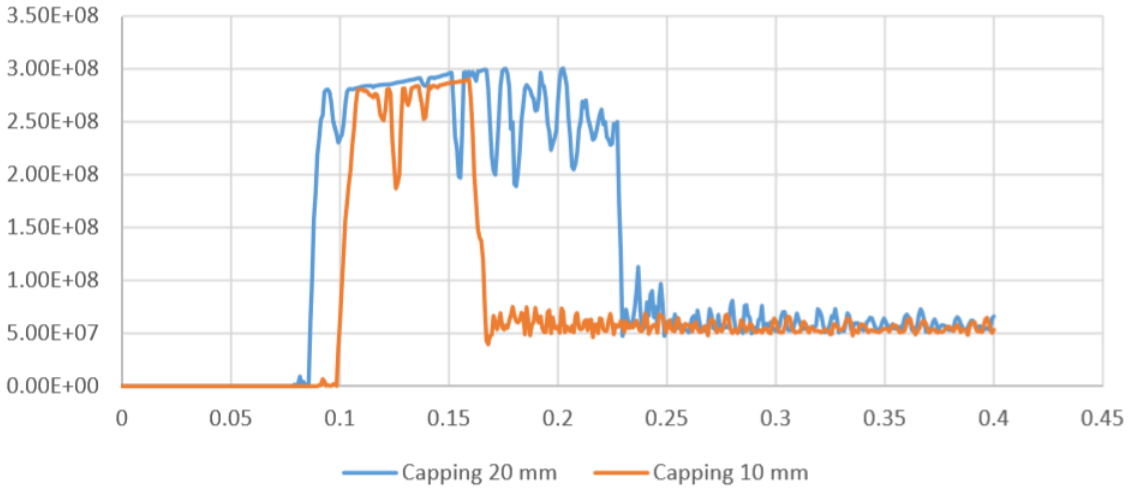

Figure 2.6: MP displacement (m) vs stress (Pa) at cylinder seal with roller support by Nishat [2]

Then replacing the roller boundary condition with fixed boundary condition, the result showns that maximum stress both at seal and piston declines around 50% than that of roller BC of K1. With Fixed BC at k1, changing welds height from 20 to 10 has decreased the maximum stress at both cylinder and piston by around 70% but stress at roller remains same. Decreasing the welds height to 5 mm will decrease the stress concentration further. Figure 2.7 shows the stress at the cylinder seam during monopile moving downward when the boundary condition for K1 is fixed support. Different from the above case, not only the contact duration for red curve (capping 20 mm) is larger than the blue curve (capping 10 mm), but also the maximum stress for red curve is much larger than the blue curve.

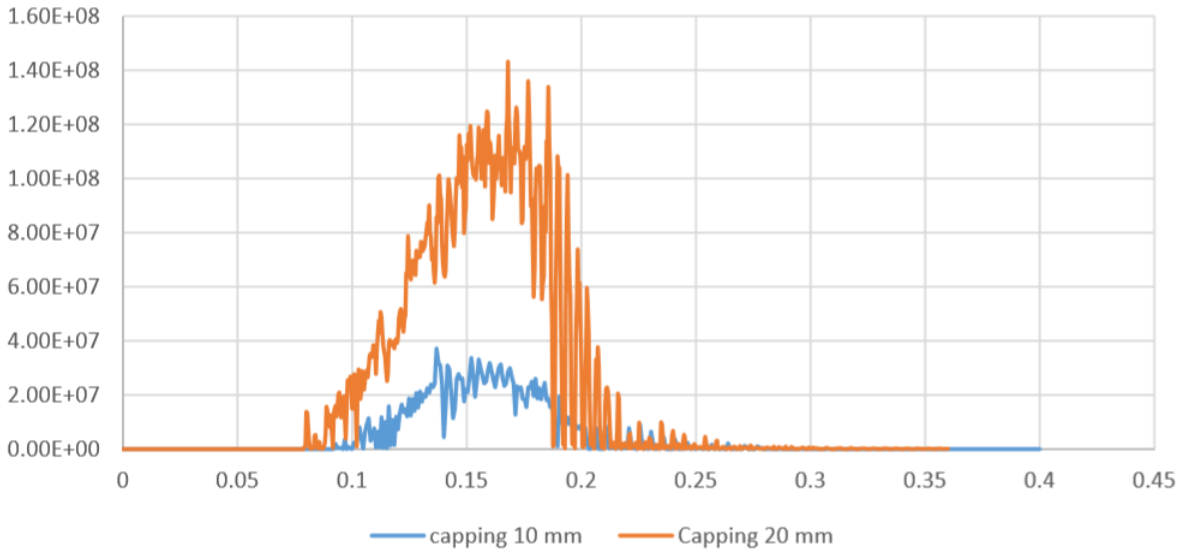

Figure 2.7: MP displacement (m) vs stress (Pa) at cylinder seal with fixed support by Nishat [2]

The Nishat's results are capable of reflecting the behavior of gripper device during constant monopile movement. However, in the real case, the monopile is moving downward by several jerks due to stress wave propagation. For each jerk, the welds strikes the piston at least once. The motion of the piston should not be the same with which caused by constant monopile motion. Furthermore, the longitudinal stress wave will cause longitudinal strain, and then, because of Poisson's ratio, it will cause horizontal strain for the monopile surface. The horizontal deformation of monopile surface acts like a protrusion moving up and down and strikes the piston. Taking consideration of above reason, a whole model contains monopile, soil resistance, hammer load, welds and gripper device should be built to analyzing this problem further.

Chapter 3

Theoretical background

3.1 Soil resistance

3.1.1 Classification

The soil in offshore environment is commonly classified in four types based on the particle size: clay, silt, sand and gravel [13]. Clay and sand can be called fine-grained, which has low permeability. Sand and gravel can be called coarse-grained, which has high permeability. The range of each soil type is presented as Figure 3.1.

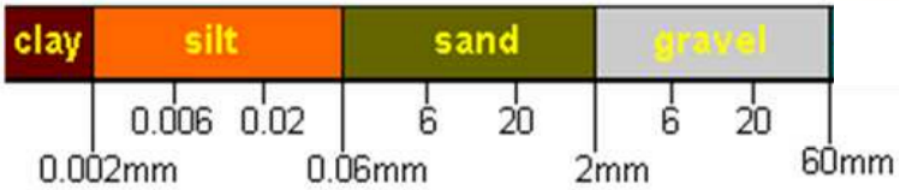

Figure 3.1: Range of different soil types [3]

3.1.2 Undrained behavior

A saturated soil sample consists of both solid particles and pore water (the water in solid particles interval), Figure 3.2. The saturated soil can be devided into two conditions: 1) drained condition; 2) undrained condition. For a soil contains large soil particle, like sand and gravel, the pore water can flow out of the soil from intervals, which is called drained condition. For a

soil contains small soil particle, like clay, the pore water can not penetrate from the internal, which is called undrained condition.

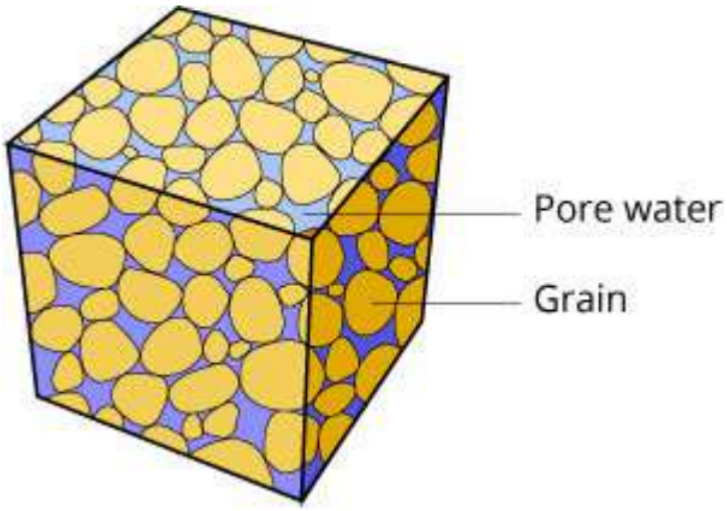

Figure 3.2: Description of a soil sample [3]

In a drained condition, compressing the soil sample will not excite rising of pore water, because the water flow out. So, the total pressure equals to the pressure acting directly on soil particles.

While, in a undrained condition, compressing the saturated soil, the pressure in the pore water (pore pressure) increasing with the effective pressure, which act directly at soil particles.

$$p' = p - p_0 \tag{3.1}$$

where,

p' = the effective pressure,

p = the total pressure,

p_0 = the pore pressure.

3.1.3 Axial capacity

The axial soil resistance can be divided into friction resistance and end-bearing resistance. The ultimate soil resistance for a pile at certain penetration depth can be calculated by API standard. However, during installation, the real soil resistance would decrease because of distortion of adjacent soil and excessive pore pressure. This soil behavior is very hard to model. For simplicity, the soil resistance during monopile installation is calculated as the same way as ultimate soil resistance.

Ultimate bearing capacity

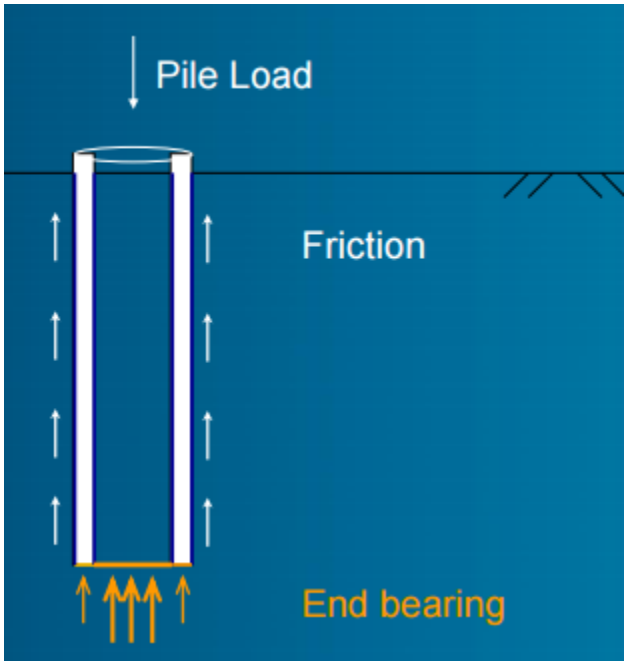

Figure 3.3: Force on a pile due to soil resistance

In this report, the ultimate bearing capacity is calculated using the API RP 2A-WSD [14]. The ultimate bearing capacity represents for the maximum axial load provided by soil to hold the pile in-place and stand stable. For a monopile foundation, the axial capacity consists of the friction resistance on the pile lateral surface and the end-bearing resistance at the pile toe.

$$Q_a = Q_f + Q_t = f A_f + q A_t \tag{3.2}$$

where,

Q_f = friction resistance on the pile lateral surface,

Q_t = tip resistance at the pile toe,

f = unit skin friction capacity,

A_f = total area where friction occurs,

q = unit end bearing capacity.

A_t = Cross sectional area of the pile toe.

The soil property in this thesis is undrained soft clay. The equation for calculating axial capacity for clay is presented below.

Axial capacity for clay

For clay, the unit skin friction capacity f can be derived as:

$$f = \alpha s_u \tag{3.3}$$

where,

s_u = undrained shear strengh of the soil at the point of calculation,

α = a dimensionless factor.

The α can be calculated by the equations:

$$\begin{aligned} \alpha &= 0.5\Psi^{-0.5} \qquad \Psi \leq 1.0 \\ \alpha &= 0.5\Psi^{-0.25} \qquad \Psi > 1.0 \end{aligned} \tag{3.4}$$

It should be noticed that α should be always not larger than 1.

Ψ can be calculated as:

$$\Psi = \frac{s_u}{\sigma'_v} \tag{3.5}$$

The unit end bearing coefficient q for clay is:

$$q = 9 s_u \tag{3.6}$$

Plug

In a open ended pile, the inside area of pile is filled with soil. The inside soil has a downward force due to inner surface friction from pile, as well as a upward force due to the soil beneath pile tip. If the inner surface friction from pile is larger than the end bearing capacity due to the soil beneath pile tip, the inside soil will move together with the pile, which plug occurs.

This phenomenon occurs mostly at a large pile penetration depth. The area where inner friction occurs $A_{f,i}$ increasing linearly with the penetration depth while the end bearing area of inner soil $A_{t,s}$ is constant.

$$A_{f,i} = \pi D_i d \tag{3.7}$$

$$A_{t,s} = \pi D_i^2 / 4 \tag{3.8}$$

where

D_i = the inner diameter of pile,

d = penetration depth.

So, the inner friction $Q_{f,i}$ and end bearing capacity of inner soil $Q_{t,s}$ is:

$$Q_{f,i} = f \pi D_i d \tag{3.9}$$

$$Q_{t,s} = q \pi D_i^2 / 4 \tag{3.10}$$

With unit skin friction capacity f and unit end bearing capacity q change little with penetration depth, plug will happen after a certain penetration depth. But at the beginning of pile penetration, the inner friction is so small that plug can be neglected.

3.2 Theory of rigid pile model

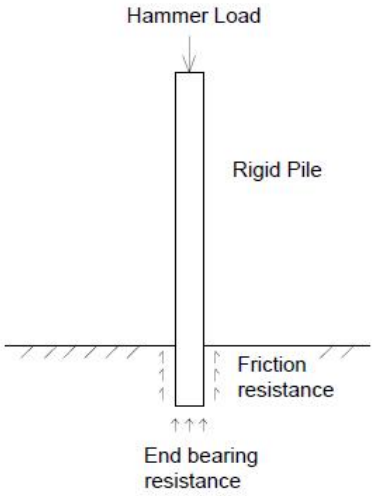

Figure 3.4: Senario of rigid pile model

In order to know the hammer load on the pile top, a rigid pile model is built. Assuming the pile is rigid, the hammer-pile-soil interaction can be solved using the Newton's law, conservation of energy and conservation of momentum.

During one penetration, the pile starts to move when the impact force acts on the pile top. After penetrating a certain depth ds, it will stop due to soil resistance. The forces acting on the soil is hammer load, gravity and soil resistance. According to conservation of energy, the total effective energy transferred to the pile plus the work done by gravity equals to the work done by soil resistance:

$$E_e + M_{pile} \cdot \mathrm{d}s = \int_{z_{start}}^{z_{end}} R_s(z) \cdot \mathrm{d}z \tag{3.11}$$

where,

$E_e = \xi \cdot E_{tot}$, the effective energy transferred to pile,

R_s = the total soil resistance along the pile,

z_{start} = starting point of one penetration,

z_{end} = stop point of one penetration.

ξ is the efficiency of hammer. When the ram hit the pile top, the kinematic energy from hammer can not completely transfer to pile[15]. Some of the energy is lost by thermal radiation and some

of the energy is stored in the ram. The ratio of energy transfer can be influenced by anvil property, pile diameter and thickness. The research in ξ can be found according to F Rausche[16]. For simplicity, the mass of hammer components except the ram (includes anvil, pile etc.) is denoted as M_c, and the mass of ram is denoted as M_r. The energy transferred to the pile can be calculated as:

$$E_e = E_{tot}\frac{M_r + e^2 M_c}{M_r + M_c} \tag{3.12}$$

where,

e = coefficient of restitution(varying in different situation).

F Rausche has done several tests to find the energy transfer ratio from ram to pile. According to his test result, the larger a ram weight, the less energy it transfers to the pile. For a large pile weight to hammer weight ratio, it can be assumed that 60% of the ram's kinematic energy will be transferred to pile. So, 60% of the total hammer drop energy is used as effective energy in this calculation. Knowing the starting point of one penetration, R_s can be calculated using API standard (as described in chapter 5.3). So, with the calculated soil resistance and the total effective energy, the penetration depth due to single impact can be calculated by Equation 3.11.

Then, using the simplified time series of impact load, the total force on pile can be calculated by summing up the impact load, soil resistance and gravity of the pile. The friction between gripper and pile should be included but it is so small that can be neglected.

$$F_{tot} = F_{imp}(t) + G_{pile} - R_s(t) \tag{3.13}$$

where,

$F_{imp}(t)$ = impact force on pile due to hammering,

G_{pile} = the gravity of the pile.

The magnitude of impact force $F_{imp}(t)$ is unknown at present. In order to calculate the total force on pile, the peak value of $F_{imp}(t)$ can be assumed as F_p. Then, the impact force can be

represented as:

$$F_{imp}(t) = \begin{cases} \frac{2F_p}{t_{end}} \cdot t & 0 \le t \le \frac{t_{end}}{2} \\ \\ -\frac{2F_p}{t_{end}} \cdot (t - t_{end}) & \frac{t_{end}}{2} < t < t_{end} \end{cases} \tag{3.14}$$

where,

t_{end} = time when impact force on pile dies out.

With the total force on pile, the acceleration of pile can be calculated by Newton's law:

$$A_{pile}(t) = F_{tot}(t)/M_{pile} \tag{3.15}$$

where,

M_{pile} = mass of the pile.

In general, the pile does not have a initial velocity before contact with hammer. The velocity of the pile can be calculated by integrating the pile acceleration along time:

$$V_{pile}(t) = \int_0^t A_{pile}(t)\mathrm{d}t \tag{3.16}$$

The pile movement can be calculated by pile velocity:

$$S_{pile}(t) = \int_0^t V_{pile}(t)\mathrm{d}t \tag{3.17}$$

At the beginning of impact, the impact force is much larger than the soil resistance. The pile will move downward with a rapidly increasing acceleration after contact with the hammer, then the acceleration will decrease. The accelerate process will last for a very short time until the impact force dies out, and, at this time, the speed of the pile reaches its maximum value. After that, the acceleration of the pile will turn upward due to the soil resistance. At the end, the pile stops. The time when the pile stop t_{stop} can be found in the relationship between the pile speed at t_{end} and

the pile acceleration at t_{end}:

$$t_{stop} = V_{pile}(t_{end}) / A_{pile}(t_{end}) \tag{3.18}$$

The total distance of pile settlement calculated by Equation 3.17 should be equal to the settlement calculated by Equation 3.11:

$$S_{pile}(t_{stop}) = ST \tag{3.19}$$

where,

$ST = z_{start}$-z_{end}, the monopile penetration calculated by Eq. 3.11 During the upon procedures, the hammer load peak value is unknown. Several initial guess for hammer load peak value should be made and inserted in upon calculation. When the result converge, the certain peak value is valid.

3.3 Cylinder force during monopile installation

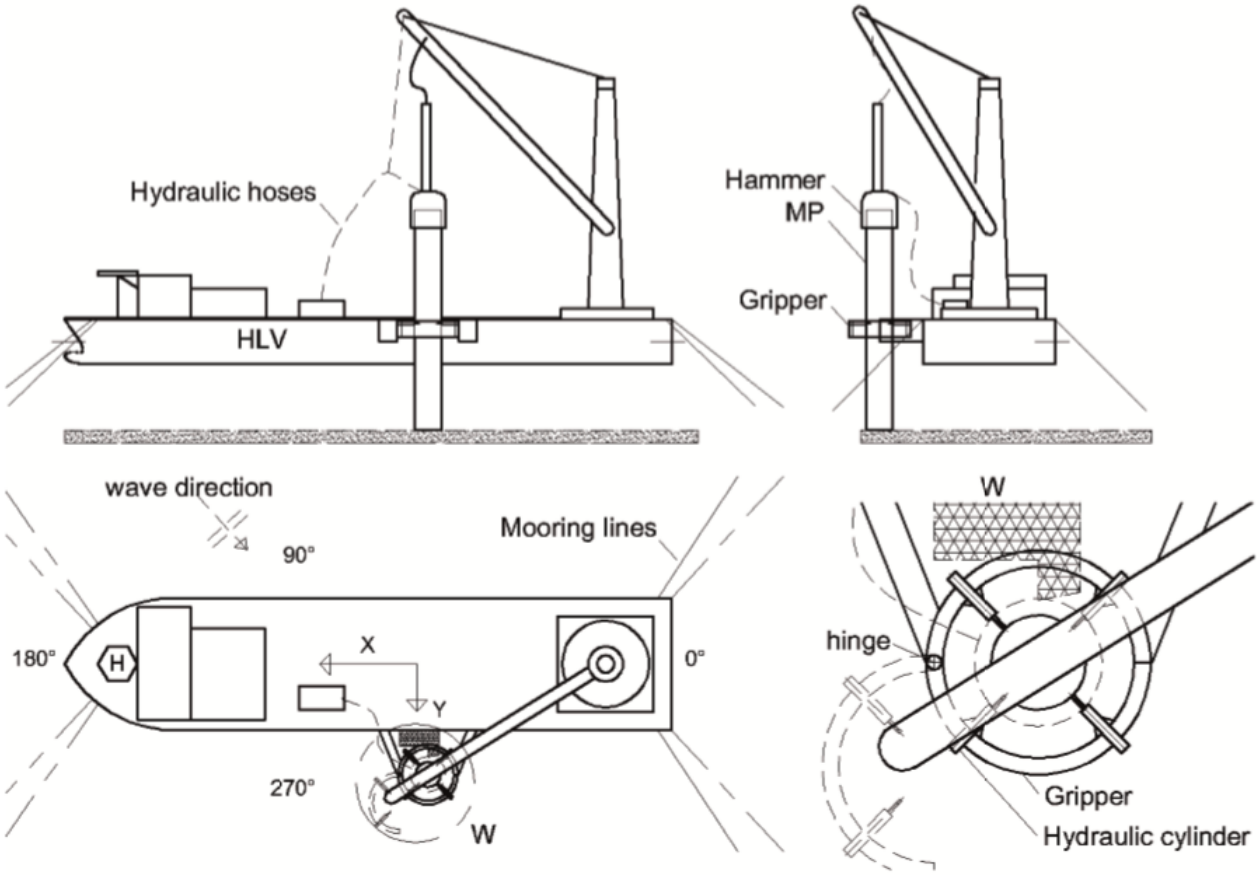

Figure 3.5: The system setup by Lin Li [4]

Considering the monopile-vessel system, Figure 3.5, the monopile is connected with gripper, which allows monopile to move along z-direction and rotation but not in x, y-direction. The gripper can be assumed as a cantilever beam, which has a fixed end on the vessel. Due to the environmental loads (mainly wave) on this system, the motion of vessel and monopile can be excited. The amplitude of the motion of monopile is small because soil can support it laterally against the wind and wave load. While, the gripper couples the motion of monopile and vessel. The motion of vessel with large amplitude can create large loads on the gripper.

Lin Li [4] has built a coupled model is this system in SIMA considering the vessel's shield effect on monopile. The paper analyzes the motion and dynamic responds with various monopile penetration (floating, 2 m, 4 m, 6 m and 8 m penetration) and various soil properties. The result is shown in Figure 4.7.

3.4 Stress wave theory

3.4.1 Introduction to stress wave

In classical mechanics, when a free body is acted upon by an external force, the whole body is assumed to be affected by the force immediately, and moves with an acceleration, given by Newton's Second Law ($F = ma$). Clearly, this is a simplification , since it is impossible for the message that a load has been applied to travel throughout the body instantaneously, but it is usually OK for the types of forces typically encountered in everyday civil engineering.

This may however, be a gross oversimplification when a structure is subjected to a rapidly changing load, such as that caused by hydraulic hammer. In the real world, the pile does not act like a rigid structure when bearing loads with large amplitude. It acts more like a series of springs: part of the structure close to the point of application of the load can be highly stressed, while a more distant area is still unaware of any loading having occurred. The message that loading has occurred is carried from the point of application to other parts of the structure by stress waves and the purpose of this lecture is to take a look at some simple properties and uses of elastic stress waves. Stress wave theory should be applied to solve pile driving problem. The idea of applying the wave equation to pile driving first came from D.V. Issacs (1931) [17]. E.A.L. Smith (1960) [18] proposed a numerical solution to investigate the effects of such factors as ram weight, ram velocity, cushion and pile properties, and the dynamic behavior of the soil during driving, which contribute to the widespread interests in this method. This chapter will introduce stress wave theory and discuss the stress wave in monopile during pile driving.

3.4.2 One-dimensional elastic stress wave propagation

Consider a rapidly changing force being applied axially, on one end of a long thin homogenous straight rod, shown in Figure 3.6.

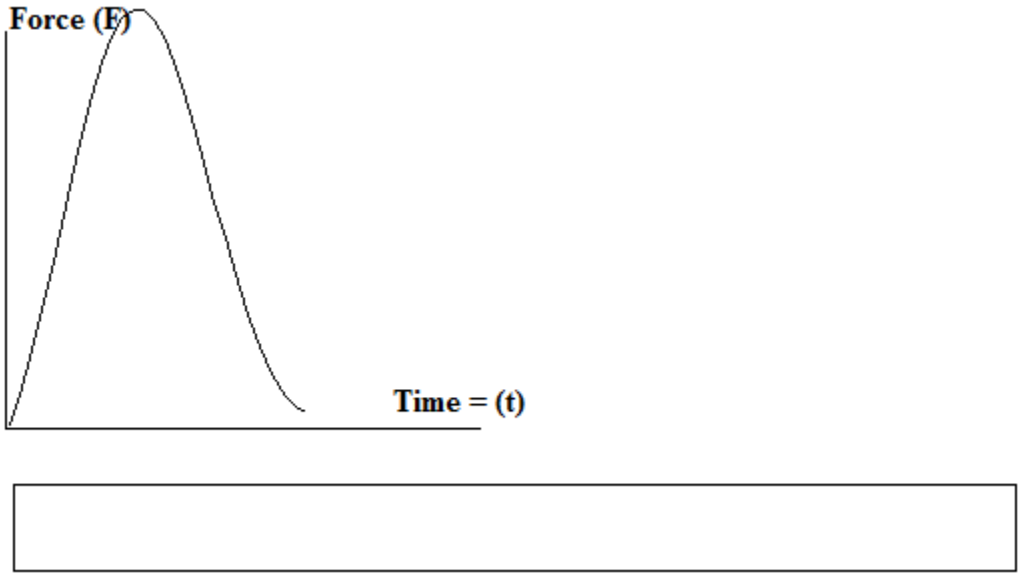

Figure 3.6: Transient force applied on one end of a rod

The particle bearing the force will displace a short distance and only disturb the next particle. By this means, the stress propagates in the rod and reaches the far end of the rod.

3.4.3 Propagation velocity

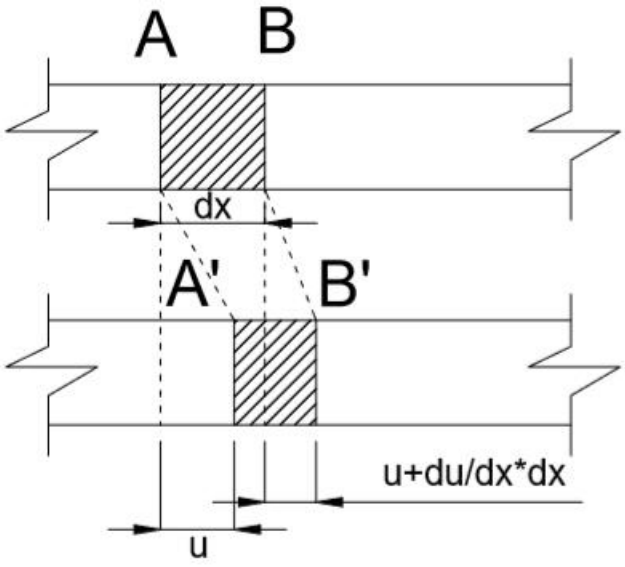

Figure 3.7: Element displacement in a rod

Assuming a stress wave is propagating from left to right. Looking at a element with the length dx:

The point A is displaced to the point A', and point B is displaced to the point B' due to the passage of stress wave. u is the particle displacement. The new length of the element is:

$$\mathrm{d}x + (u + \frac{\partial u}{\partial x}\mathrm{d}x) - u = \mathrm{d}x + \frac{\partial u}{\partial x}\mathrm{d}x \tag{3.20}$$

The axial strain ε_x in the element is the change of length divided by the original length:

$$\varepsilon_x = \frac{(\mathrm{d}x + \partial u/\partial x \cdot \mathrm{d}x) - \mathrm{d}x}{\mathrm{d}x} = \frac{\partial u}{\partial x} \tag{3.21}$$

Assuming the structure remains elastic, and applying the Hooke's Law:

$$\sigma_x = E \cdot \varepsilon_x = E \cdot \frac{\partial u}{\partial x} \tag{3.22}$$

where,

σ_x = axial stress,

E = Young's Modulus.

The total force acting on the element A'B' is the force acting on face B' minus the force acting on face A':

$$(\sigma_x + \frac{\partial \sigma_x}{\partial x}\mathrm{d}x)A_0 - \sigma_x A_0 = \frac{\partial \sigma_x}{\partial x}\mathrm{d}x A_0 \tag{3.23}$$

where,

A_0 = cross section area of the structure.

The mass of the element is $(\rho A_0 \mathrm{d}x)$ and the axial acceleration is $(\partial^2 u/\partial t^2)$. ρ is the density of the structure. Applying the Newton's Second Law:

$$\rho A_0 \mathrm{d}x \frac{\partial^2 u}{\partial t^2} = \frac{\partial \sigma_x}{\partial x}\mathrm{d}x A_0 \tag{3.24}$$

Substitute Eq. 3.22 to Eq. 3.24 :

$$\rho \frac{\partial^2 u}{\partial t^2} = E \frac{\partial^2 u}{\partial x^2} \tag{3.25}$$

Eq. 3.25 can be rewritten as:

$$\frac{\partial^2 u}{\partial t^2} = C_0^2 \frac{\partial^2 u}{\partial x^2} \tag{3.26}$$

This is the well known wave equation. C_0 describes the velocity with which a stress wave propagate in a material, and it can be expressed as:

$$C_0 = \sqrt{E/\rho} \tag{3.27}$$

It can be seen that the stress wave propagation velocity is only determined by the material property. For steel, the Young's modulus and density can be set as 2.1×10^{11} Pa and 7850 kg/m^3 respectively. Applying Eq. 3.27, the stress wave propagation velocity in steel is:

$$C_{0,steel} = \sqrt{2.1 \times 10^{11}/7850} = 5172.2 \qquad [\text{m/s}] \tag{3.28}$$

The pile's length (L_{pile}) is 55 m, so the time (T_0) which stress wave passes from one end to the other is:

$$T_0 = \frac{L_{pile}}{C_{0,steel}} = \frac{55}{5172.2} = 0.0106 \qquad [\text{s}] \tag{3.29}$$

3.4.4 Relation between particle velocity and stress

Rewrite Eq. 3.27 as:

$$\sqrt{E} = C_0 \sqrt{\rho} \tag{3.30}$$

Insert Eq. 3.30 to Eq. 3.21:

$$\sigma_x = C_0 \sqrt{E\rho} \cdot \frac{\partial u}{\partial x} \tag{3.31}$$

C_0 is the wave propagation velocity, which can be represented as:

$$C_0 = \frac{\partial x}{\partial t} \tag{3.32}$$

By substitution from Eq. 3.32, Eq. 3.31 becomes:

$$\sigma_x = \sqrt{E\rho} \cdot \frac{\partial x}{\partial t} \frac{\partial u}{\partial x} = \sqrt{E\rho} \cdot \frac{\partial u}{\partial t} = \sqrt{E\rho} \cdot v \tag{3.33}$$

The v is the particle velocity. It can be seen that the axial stress is proportional to the particle velocity v, because both E and ρ are constant.

3.4.5 Reflection of one-dimensional stress wave

Assuming an incident wave (σ_I) is propagating from left to right in a long rod. When it hit the discontinuity, some of the wave is reflected (σ_R) back and propagating toward the left side. Some of the wave is transmitted (σ_T) through the surface and continue propagate toward the right side. Applying equilibrium of force at the surface of discontinuity:

$$A_1 \cdot (\sigma_I + \sigma_R) = A_2 \cdot \sigma_T \tag{3.34}$$

where,

A_1 = the cross section area of left rod,

A_2 = the cross section area of right rod.

There is no separation occur on the surface of discontinuity, so the particle velocity at two sides should be equal:

$$v_I - v_R = v_T \tag{3.35}$$

v_I, v_R and v_T is the particle velocity induced by incident wave, reflected wave and transmitted wave respectively. Applying Eq. 3.33 to v_I, v_R, v_T:

$$v_I = \sigma_I / \sqrt{E_1 \rho_1}, \qquad v_R = \sigma_R / \sqrt{E_1 \rho_1}, \qquad v_T = \sigma_T / \sqrt{E_2 \rho_2} \tag{3.36}$$

where,

E_1 = the Young's modulus of left rod,

ρ_1 = the density of left rod,

E_2 = the Young's modulus of right rod,

ρ_2 = the density of right rod.

and insert to Eq. 3.35:

$$\frac{\sigma_I}{\sqrt{E_1 \rho_1}} - \frac{\sigma_R}{\sqrt{E_1 \rho_1}} = \frac{\sigma_T}{\sqrt{E_2 \rho_2}} \tag{3.37}$$

This equation can be reformed as:

$$\sigma_R = \sigma_I - \frac{\sqrt{E_1\rho_1}}{\sqrt{E_2\rho_2}} \cdot \sigma_T \tag{3.38}$$

Substituting Eq. 3.38 to Eq. 3.34:

$$A_1(\sigma_I + (\sigma_I - \frac{\sqrt{E_1\rho_1}}{\sqrt{E_2\rho_2}} \cdot \sigma_T)) = A_2\sigma_T \tag{3.39}$$

After simplification, the transmitted stress can be represented as:

$$\sigma_T = \frac{2\sqrt{E_2\rho_2} \cdot A_1}{\sqrt{E_1\rho_1} \cdot A_1 + \sqrt{E_2\rho_2} \cdot A_2} \cdot \sigma_I \tag{3.40}$$

Substituting Eq. 3.40 to Eq. 3.34, the reflected stress can be written as:

$$\sigma_R = \frac{\sqrt{E_2\rho_2} \cdot A_2 - \sqrt{E_1\rho_1} \cdot A_1}{\sqrt{E_1\rho_1} \cdot A_1 + \sqrt{E_2\rho_2} \cdot A_2} \cdot \sigma_I \tag{3.41}$$

If the rod have a free end at the right side, then E_2, ρ_2 is zero. According to above equations, the transmitted stress is zero. The reflected stress have the same magnitude but opposite sign with incident stress. In physics it means that, if a compressive wave is a incident wave, it will become a tensile wave after reflected from free end. Although the stress changes sign, it still make particle move toward right. The different is that, for compressive wave, the left particle 'push' the right particle to the right direction, but, for the tensile wave, the right particle 'pull' the left particle to the right direction.

The theoretical displacement for a particle on the rod is shown in Figure 3.8. The particle moves toward by several jerks and it only moves when it is encountered with the stress wave. During the gap between encounter of stress wave, the particle should have zero displacement.

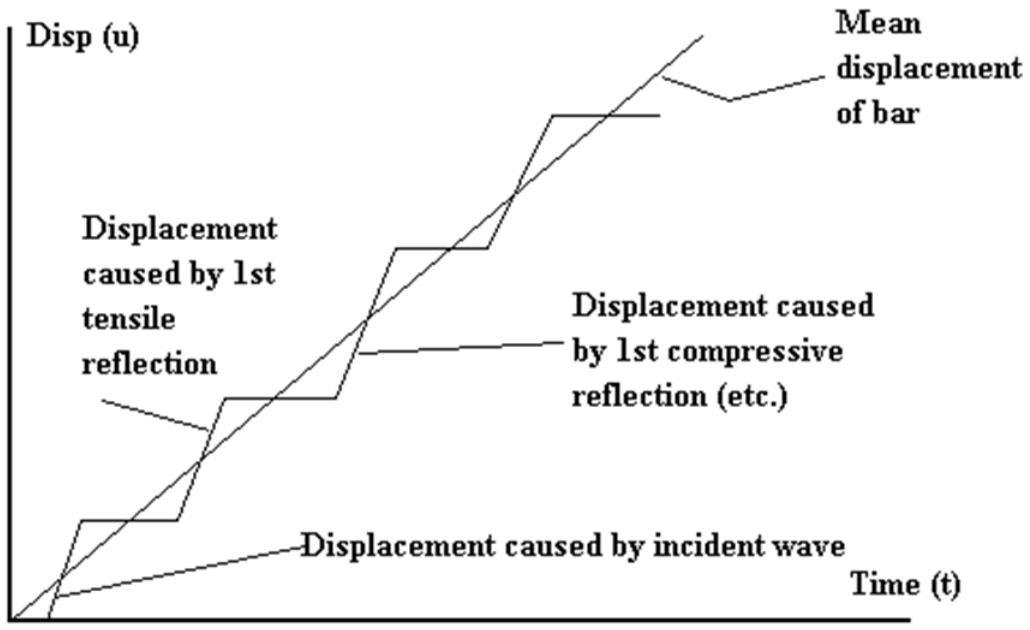

Figure 3.8: Displacement of a particle with free-end boundary condition

3.5 Theory for contact and interaction in Abaqus

A 3D object may contact on a (or a series of) shared point(s) or surface(s). Contact mechanics, developed based on the continuum mechanics and mechanics of materials, is a theory to describe pressure and adhesion (normal) and friction (tangential) stresses that arise during shared point/surface contact between deformable bodies [5].

The types of contact can be defined as general contact (a single contact definition that can cover many or all region of a model) and contact pairs (a unique contact definition can be applied between the chosen surfaces). In this thesis contact pairs are used in the model.

To define a contact pair, one must indicate which pairs of surfaces may interact with one another or which surfaces may interact with themselves. Contact surfaces should extend far enough to include all regions that may come into contact during an analysis; however, including additional surface nodes and faces that never experience contact may result in significant extra computational cost (for example, extending a slave surface such that it includes many nodes that remain separated from the master surface throughout an analysis can significantly increase memory usage unless penalty contact enforcement is used). Every contact pair is assigned a contact for-

mulation (either explicitly or by default) and must refer to an interaction property.
When a contact pair contains two surfaces, the two surfaces are not allowed to include any of the same nodes and you must choose which surface will be the slave and which will be the master. For simple contact pairs consisting of two deformable surfaces, the following basic guidelines can be used:

- The larger of the two surfaces should act as the master surface.
- If the surfaces are of comparable size, the surface on the stiffer body should act as themaster surface.
- If the surfaces are of comparable size and stiffness, the surface with the coarser mesh should act as the master surface.

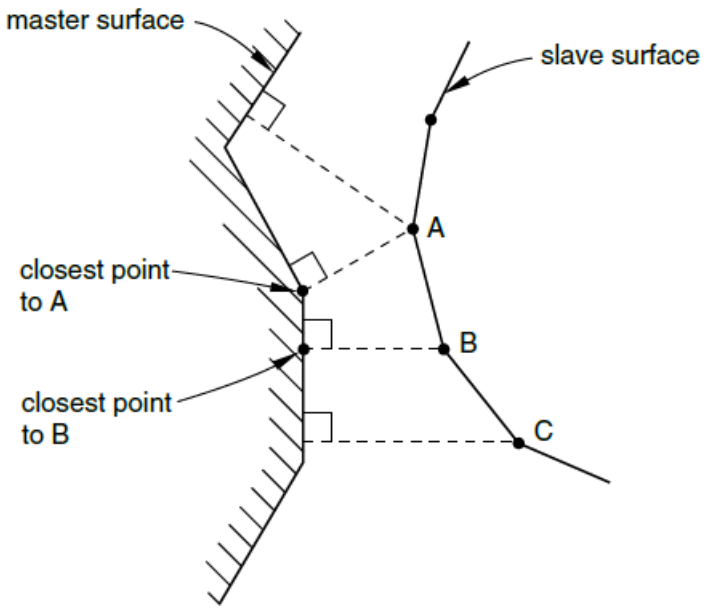

Figure 3.9: Node-to-surface contact discretization [5]

Abaqus/Standard provides several contact formulations. Each contact formulation is automatically selected (or may be altered by user) based on:

- Choice of contact discretization: node-to-surface contact discritization and surface-to-surface contact discretization

- Tracking approach: have considerable impact on how contact surfaces interact and selected to be:
  - Finite sliding: most general case
  - Small sliding: despite the state of deformation assumes little sliding between contact pairs is assumed
- Assignment of master and slave roles to contact surfaces. General contact algorithm in Abaqus/Standard uses finite-sliding, surface-to-surface contact formulation by default.

Abaqus/Standard uses conditional constraints to enforce contact between interacting surfaces. The location and conditions of these constraints may vary based on the type of contact discretization. In traditional node-to-surface discretization each slave node interacts with a point of projection on the master surface on the opposite side of the contact interface (a single slave node interacts with a group of master nodes) with following characteristics:

- Slave nodes are constrained not to penetrate master surface.
- Nodes of master surface can, in principle, penetrate into the slave surface.
- Contact direction is selected based on the normal of master surface.
- only information needed for a slave surface node are i) its location, and ii) surface area associated to it. Thus, the slave surface can be defined as a group of nodes—a node-based surface.
- Node-to-surface discretization is available even if a node-based surface is not used in a contact pair definition

In surface-to-surface contact discretization the shape of both master and slave surfaces are considered, therefore it provides more accurate results than node-to-surface discretization. In surface-to-surface discretization:

- contact conditions are enforced in an average sense over regions nearby slave nodes rather than only at individual slave nodes.

- the averaging regions are approximately centered on slave nodes, so each contact constraint will predominantly consider one slave node but will also consider adjacent slave nodes.
- some penetration may be observed at individual nodes; however, large, undetected penetrations of master nodes into the slave surface do not occur
- the contact direction is based on an average normal of the slave surface in the region surrounding a slave node
- is not applicable if a node-based surface is used in the contact pair definition

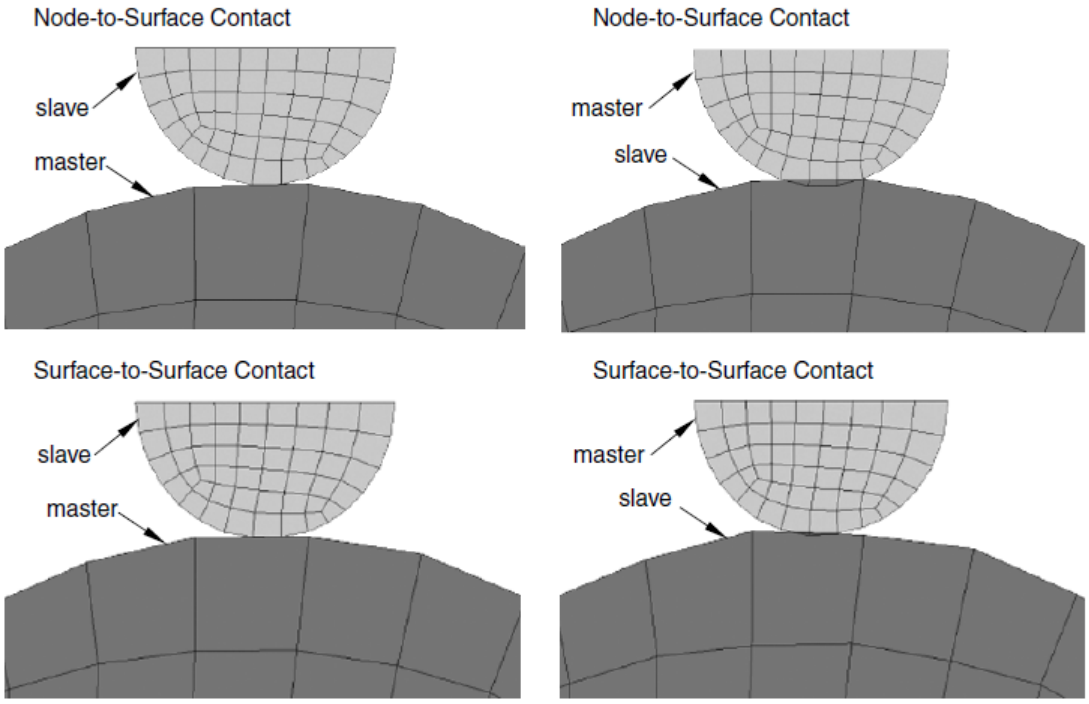

Figure 3.10: Comparison of contact enforcement for different master-slave assignments with node-to-surface and surface-to-surface contact discretizations [5]

3.6 Theory for natural frequency extraction in Abaqus

3.6.1 Overview of natural frequency extraction

Using ABAQUS narutal frequency extraction, the natural frequency and the corresponding mode shapes of a finite element system can be extracted. This procedure includes initial stress and load stiffness effects due to preloads and initial conditions if geometric nonlinearity is accounted for in the base state, so that small vibrations of a preloaded structure can be modeled. It should be noticed that this procedure solves the eigenfrequency problem only for symmetric mass and stiffness matrices; the complex eigenfrequency solver must be used if unsymmetric contributions, such as the load stiffness, are needed [19].

3.6.2 Equations for natural frequency extraction

The eigenvalue problem for the natural frequencies of an undamped finite element model is:

$$(-\omega_n^2 M^{MN} + K^{MN})\phi^N = 0 \tag{3.42}$$

where,

ω_n = the natural frequency,

M^{MN} = the mass matrix, which is symmetric and positive definite,

K^{MN} = the stiffness matrix, which includes initial stiffness effects if the base state included the effects of nonlinear geometry,

ϕ^N = the eigenvector,

M, N = degrees of freedom.

When K^{MN} is positive definite, all eigenvalues are positive. Rigid body modes and instabilities cause K^{MN} to be indefinite. Rigid body modes produce zero eigenvalues. Instabilities produce negative eigenvalues and occur when you include initial stress effects.

Chapter 4

Calculation for external loads

4.1 Soil resistance

4.1.1 Soil property

For simplicity, the soil in this thesis is chosen as undrained clay. The soil properties is shown in Table 4.1. Its self weight is 20 kN/m^3. The undrained shear strength S_u is 1000 N/m^2, and it increases by 4000 N/m^2 going each meter deeper.

Table 4.1: Soil properties

Soil Weight (γ)	20000	N/m^3
Shear strength ($S_{u,top}$)	1000	N/m^2
Friction angle (ϕ)	0	^{o}
Dilatancy angle (ψ)	0	^{o}
Increase in cohesion ($S_{u,inc}$)	4000	N/m^2/m

4.1.2 Result

The unit soil resistance and total soil resistance is shown in Figure 4.1. The unit resistance represents for the resistance in 1 m^2 of the monopile's surface. From the left figure, it can be seen that the unit friction resistance is much less than the unit end-bearing resistance. In contrast, the total friction resistance is much larger than the total end-bearing resistance, shown in the middle figure. It is because that the lateral surface of the submerged monopile, which the friction resistance acts on, increases with the penetration depth while the cross sectional area, which

the end-bearing resistance acts on, remain constant.

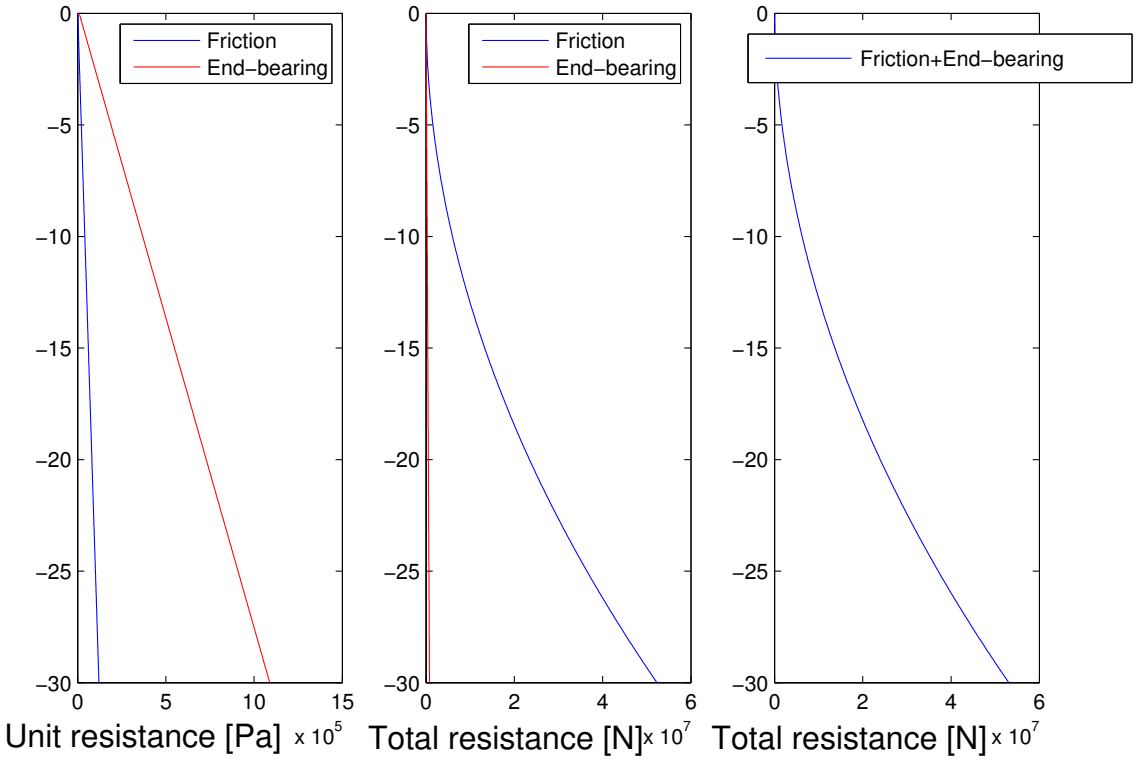

Figure 4.1: Unit and total soil resistance in diffenrent depth

4.2 Hammer load

4.2.1 Result

Figure 4.2 describe the response of pile during hammering when drop energy is 200 kJ and initial penetration is 10 m. The first figure shows the relationship between total force and time. The hammer load peak value is 1.25 MN. The soil resistance is so small that can not be observed in the figure. The acceleration of pile is shown in the second figure, the peak value of acceleration is 380.3 m/s^2. The acceleration after hammer load ended is 10.3 m/s^2. The third figure depicts the velocity of the pile. The velocity first goes larger rapidly then decreases slowly. Its amplitude is relatively small due to short time of acceleration. The pile settlement is shown in the forth figure. It can be seen that most of the pile penetration is done after the hammer load dies out.

The final settlement is 0.0364 m.

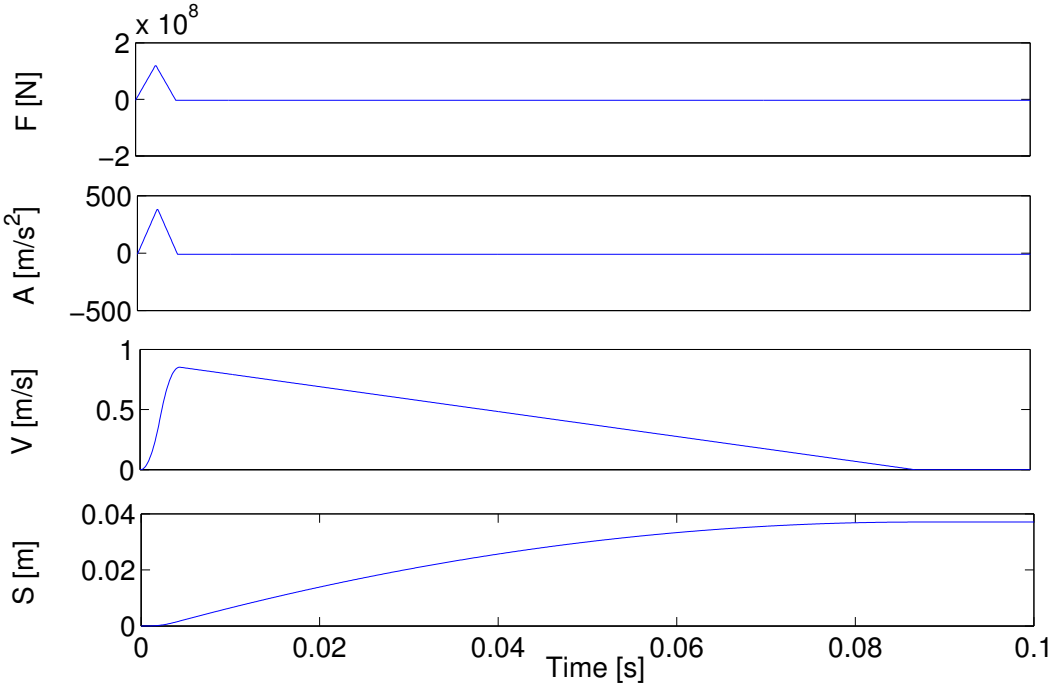

Figure 4.2: A case of pile motion

The pile motion can be influenced by changing the initial penetration and hammer drop energy. Several comparison cases has been carried out using different drop energy: 200 kJ, 250 kJ, 300 kJ, 350 kJ, 400 kJ, 450 kJ, 500 kJ, 550 kJ, 600 kJ; and different initial penetration: 7 m, 8 m, 10 m, 15 m, 20 m, 25 m, 29 m(pile penetrates soil 7 m by self weight). The result is shown in Table 4.2.

It can be seen that, with the increasing of the initial penetration, the soil becomes harder and more difficult to penetrate. Taking hammer drop energy 200 kJ as an example, when initial penetration is 7 m, the settlement is 0.3485. When initial penetration changes to 29 m, the settlement is 0.0026 m. When pile goes deeper, the hammer load peak value is increasing, which causes larger stress in the pile. When pile stress reaches its yield limit, the pile will fail, which will be discussed later in the next section.

Comparing the result with the same initial penetration but different hammer drop energy, for example 200 kJ and 250 kJ drop energy at 10 m initial penetration, using larger drop energy can

make pile penetrate deeper, while it induces larger stress in the pile. So, considering time consumption and safety of structure, using a large hammer drop energy in a safe range for structure is beneficial.

Table 4.2: Pile penetration parameters in different drop energy

$z_{initial}$ [m]	F_p [MN]	S_{pile} [m]	t_{stop} [s]	$z_{initial}$ [m]	F_p [MN]	S_{pile} [m]	t_{stop} [s]
200 kJ				250 kJ			
7	1.22	0.3485	0.7959	7	1.36	0.4652	0.9495
8	1.23	0.1038	0.2387	8	1.37	0.1366	0.2805
10	1.25	0.0364	0.0851	10	1.39	0.0465	0.0971
15	1.32	0.0112	0.0278	15	1.46	0.0141	0.031
20	1.43	0.0057	0.0154	20	1.57	0.0072	0.017
25	1.56	0.0035	0.0105	25	1.7	0.0044	0.0114
29	1.68	0.0026	0.0084	29	1.83	0.0032	0.0091
300 kJ				350 kJ			
7	1.49	0.5194	0.9671	7	1.61	0.5692	0.983
8	1.5	0.1621	0.3034	8	1.62	0.1870	0.3244
10	1.52	0.0557	0.1057	10	1.64	0.0649	0.1139
15	1.6	0.0169	0.0338	15	1.71	0.0197	0.0363
20	1.7	0.0086	0.0184	20	1.82	0.0100	0.0197
25	1.83	0.0053	0.0123	25	1.95	0.0062	0.0131
29	1.95	0.0039	0.0097	29	2.07	0.0045	0.0103
400 kJ				450 kJ			
7	1.72	0.5520	0.8908	7	1.83	0.6593	1.0038
8	1.73	0.1996	0.3236	8	1.84	0.2355	0.3599
10	1.75	0.0724	0.1188	10	1.86	0.0831	0.1285
15	1.83	0.0224	0.0384	15	1.93	0.0254	0.0408
20	1.93	0.0114	0.0208	20	2.03	0.0129	0.022
25	2.06	0.0070	0.0138	25	2.16	0.0079	0.0145
29	2.19	0.0051	0.0108	29	2.29	0.0058	0.0113
500 kJ				550 kJ			
7	1.93	0.7006	1.0113	7	2.02	0.7398	1.019
8	1.93	0.2590	0.3753	8	2.03	0.2821	0.39
10	1.95	0.0922	0.1351	10	2.05	0.1013	0.1414
15	2.03	0.0282	0.0429	15	2.12	0.0310	0.0449
20	2.13	0.0143	0.023	20	2.23	0.0158	0.024
25	2.26	0.0088	0.0151	25	2.36	0.0097	0.0157
29	2.39	0.0064	0.0118	29	2.48	0.0071	0.0122

600 kJ			
7	2.11	0.7773	1.0244
8	2.12	0.3048	0.4031
10	2.14	0.1103	0.1473
15	2.21	0.0338	0.0468
20	2.31	0.0172	0.025
25	2.45	0.0106	0.0163
29	2.57	0.0077	0.0126

4.2.2 Check

Yield check: Elastic-plastic material can have a permanent deformation if applying stress exceed the yield stress. The material for monopile is W50 carbon steel. For a pile which thickness within 40-100 mm, the yield stress is 325 MPa. The force applied on top of the monopile should not exceed:

$$F_{yield} = S_{yield} \cdot A = 234.8 \quad \text{MN} \tag{4.1}$$

Comparing the yield limit with the result in section 8.1.2:

- None of the peak value for 200 kJ hammer drop energy exceeds the yield limit.
- Some of the peak value at relatively deep start point for 400 kJ hammer drop energy exceeds the yield limit.
- Most of the peak value of impact force for 600 kJ hammer drop energy exceeds the yield limit.

4.2.3 Installation time

Using the data from Table 4.2, the relationship between initial penetration and settlement in each hammer drop energy can be fitted by curve, shown in Figure 4.3. The dots represent for the data in Table 4.2.

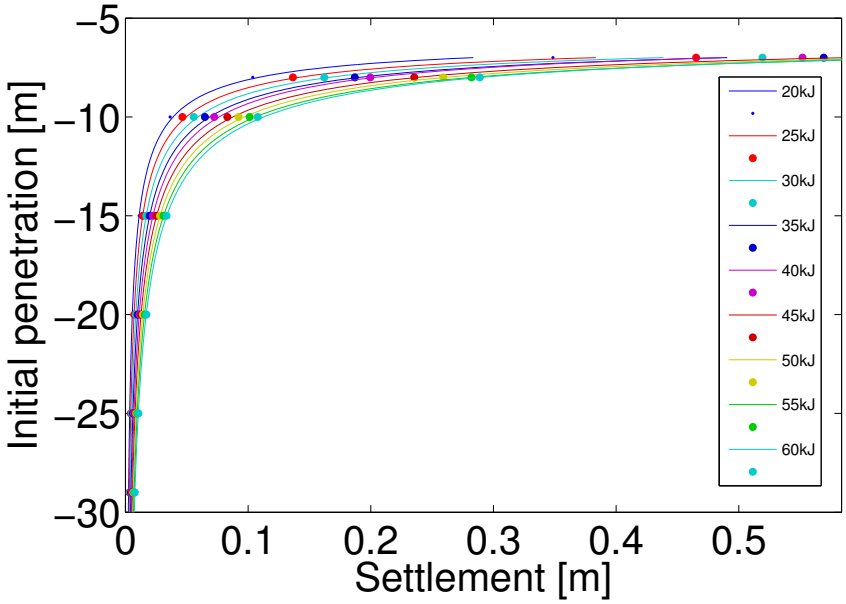

Figure 4.3: Pile settlement along initial penetration depth in different hammer drop energy

A power function is used for the curve fitting:

$$z = a \cdot ST^b + c \tag{4.2}$$

where,

z = initial penetration,

ST = pile settlement,

a, b, c = parameters in curve fitting.

Values for curve fitting parameters is shown in Table 4.3. The goodness of curve fitting is represented as sum squared error (SSE).

Table 4.3: Curve fitting parameters for settlement vs initial penetration

Hammer drop energy	a	b	c	SSE
200 kJ	-0.5420	-0.6307	-5.8000	9.039e-2
250 kJ	-0.6228	-0.6307	-5.8600	8.082e-2
300 kJ	-0.7103	-0.6281	-5.808	7.164e-2
350 kJ	-0.7942	-0.6257	-5.76	6.404e-2
400 kJ	-0.8887	-0.6212	-5.608	5.795e-2
450 kJ	-0.9532	-0.6215	-5.672	5.215e-2
500 kJ	-1.029	-0.6196	-5.631	4.740e-2
550 kJ	-1.103	-0.6177	-5.591	4.325e-2
600 kJ	-1.191	-0.6141	-5.452	4.026e-2

The fitted curve for hammer force peak value vs initla penetration is shown in Figure 4.4. In order to avoid yield in structure, the force should not exceed 234.8 MN, which is depicted in the figure as a dash line.

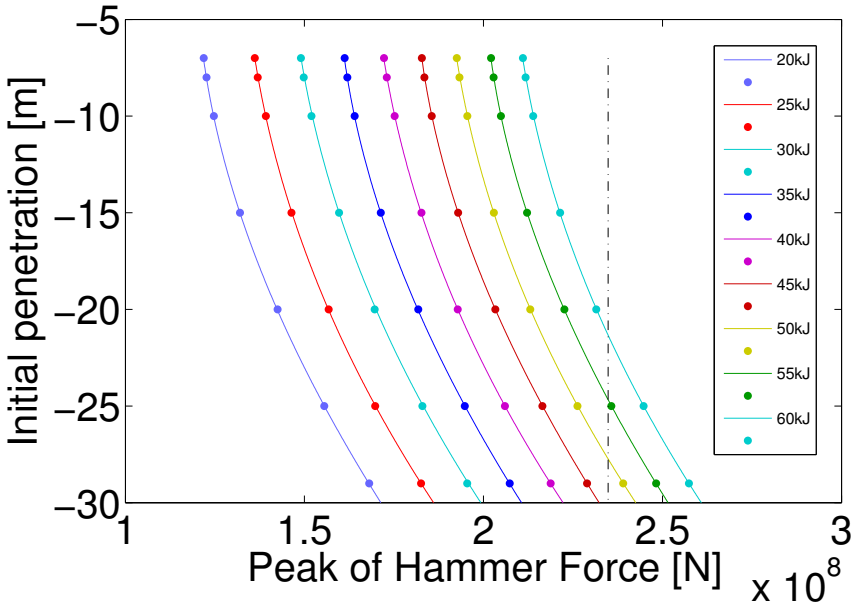

Figure 4.4: Hammer load peak value along initial penetration depth in different hammer drop energy

The function used in this curve fitting is a third order polynomial function:

$$F_p = p1 \cdot z^3 + p2 \cdot z^2 + p3 \cdot z + p4 \tag{4.3}$$

where,

F_p = hammer load peak value,

$p1, p2, p3, p4$ = curve fitting parameters.

The curve fitting parameters is shown in Table 4.4.

Table 4.4: Curve fitting parameters for hammer load peak value vs initial penetration

Hammer drop energy	p1	p2	p3	p4	SSE
200 kJ	323.1	75610	269500	120100000	1.444e10
250 kJ	-128.8	51660	-109900	132800000	3.3535e10
300 kJ	-66.74	53380	-130700	145500000	7.787e10
350 kJ	296.7	74280	253900	159400000	2.398e10
400 kJ	-125.2	51510	-126100	168700000	1.485e10
450 kJ	326.6	75860	275500	181100000	5.372e9
500 kJ	-68.62	55060	-57360	189400000	1.638e10
550 kJ	302.6	74870	268600	200400000	1.012e10
600 kJ	-26.13	56730	-39320	207900000	2.516e10

The maximum energy in each depth is calculated by linear interpolation, shown in Figure 4.5 blue curve. In the other case, if the energy can not change, the maximum energy should not cause stress larger than the yield limit at all initial penetration depth, shown in Figure 4.5 black curve.

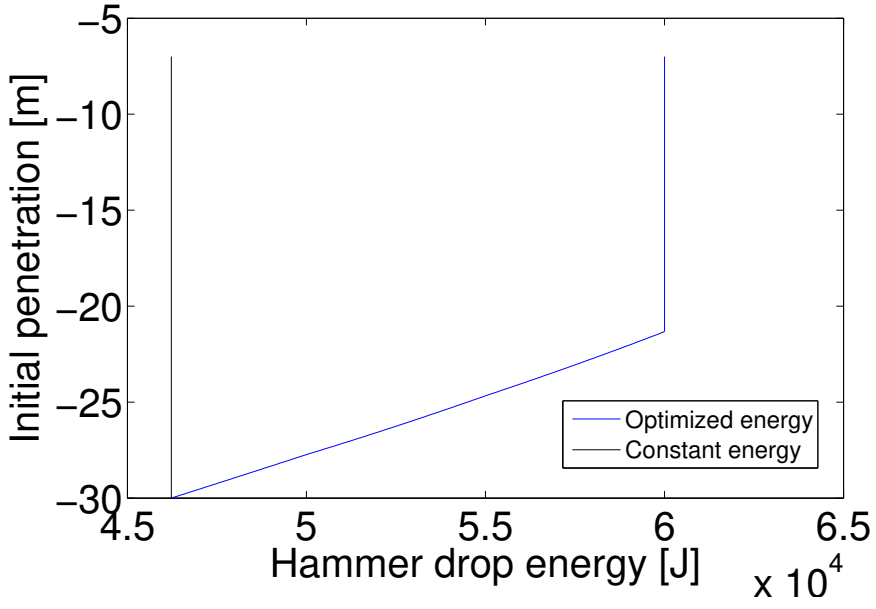

Figure 4.5: Maximum energy along initial penetration depth

According to the different energy strategy used in driving process, the pile settlement for one

blow at different initial penetration depth can be calculated, shown in Figure 4.6.

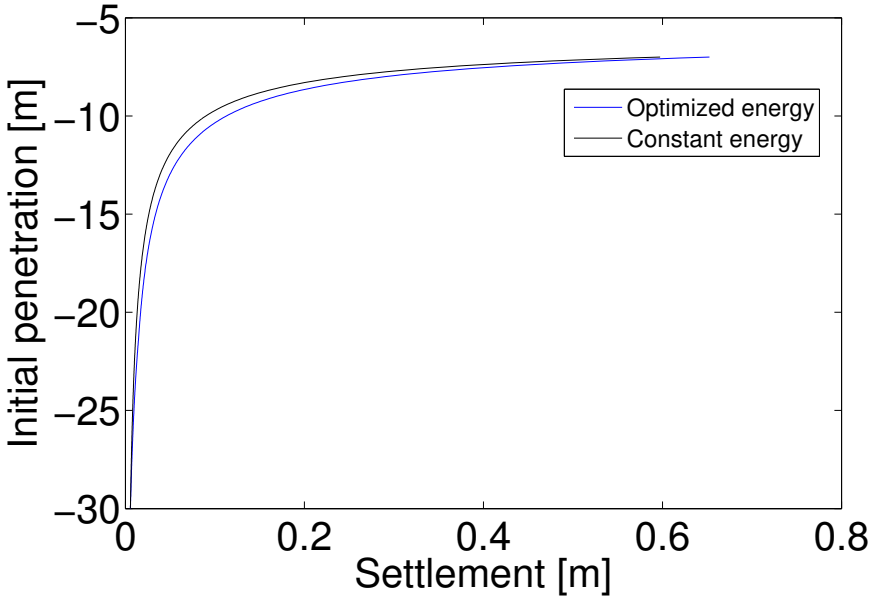

Figure 4.6: Pile settlement for changing and constant drop energy along initial penetration depth

The total blow times for driving a pile from -7 m to -30 m can be counted using upon data. For constant energy, the total blow times is 1663. For optimized energy, the total blow times is 1415. The blow speed for the chosen hammer is set as 40 blow/minute according to product manual. The total driving time can be calculated as:

$$T_{driving,const} = 1663/40 \times 60 \approx 2495 \quad [s]$$

$$T_{driving,optim} = 1415/40 \times 60 \approx 2123 \quad [s]$$

where,

$T_{driving,const}$ = total driving time for constant drop energy,

$T_{driving,chang}$ = total driving time for optimized drop energy.

Compare the two installation time from, it is can be seen that increasing the drop energy can reduce the installation time by 372 s, which is approximately 15% of the total installation time.

4.3 Cylinder force result from Lin Li

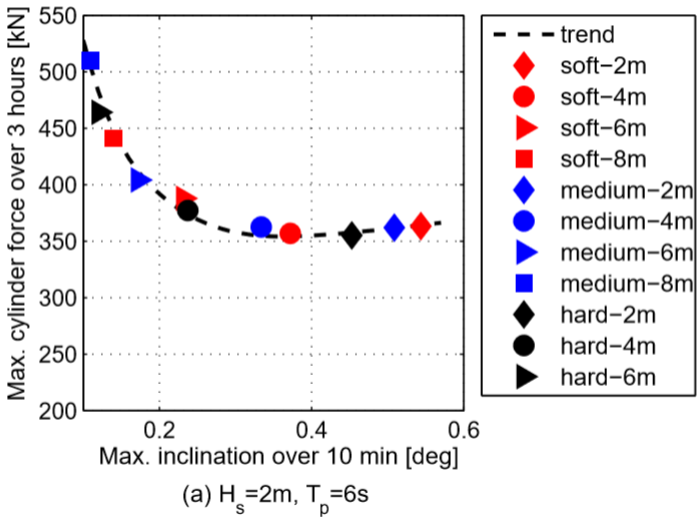

Figure 4.7: Lin Li's result of extreme cylinder force in 3 hours versus MP maximum inclination in 10 min for different soil properties and different penetrations[4]

The cylinder force is the maximum force between the monopile and hydraulic cylinder on gripper. It can be seen that when the inclination angle decreases due to monopile going deeper, the extreme cylinder force increases. Changing the soil property from soft to hard, the trend remains the same, but the value for maximum inclination decreases and the value for extreme cylinder force increases.

This thesis uses undrained soft clay for calculation, which corresponding to the soft soil in Figure 4.7. The environmental load for different initial penetration depth can be obtained from the figure. Taking 8 m pile penetration with soft soil as an example (marked with red square in the figure), the maximum cylinder force over 3 hours is around 450 kN, and the maximum inclination over 10 min is around 0.1 degree. It can be seen that the maximum inclination is very small, so it can be neglected during calculation.

Chapter 5

Finite element model

5.1 Introduction to Abaqus

This section will use Abaqus to solve elastic pile model. Abaqus FEA (formerly ABAQUS) is a software suite for finite element analysis and computer-aided engineering, originally released in 1978 [20]. This software is widely used for structure and fluid analysis in the automotive, aerospace, and industrial products industries. The Abaqus product suite consists of five core software products:

1. Abaqus/CAE, or "Complete Abaqus Environment". It is a software application used for both the modeling and analysis of mechanical components and assemblies (pre-processing) and visualizing the finite element analysis result.

2. Abaqus/Standard, a general-purpose Finite-Element analyzer that employs implicit integration scheme.

3. Abaqus/Explicit, a special-purpose Finite-Element analyzer that employs explicit integration scheme to solve highly nonlinear systems with many complex contacts under transient loads.

4. Abaqus/CFD, a Computational Fluid Dynamics software application which provides advanced computational fluid dynamics capabilities with extensive support for preprocess-

ing and postprocessing provided in Abaqus/CAE.

5. Abaqus/Electromagnetic, a Computational electromagnetics software application which solves advanced computational electromagnetic problems.

5.2 Abaqus modelling

5.2.1 Geometry and material model

Monopile

The monopile has a diamater of 4.6 m and thickness of 0.05 m. The inner diameter is 2.275 m and the outer diameter is 2.325 m. The length of the monopile is 55 m. Figure 5.1 shows the cross section of the monopile. Because of the symmetric geometry, a quarter of the monopile is built in Abaqus.

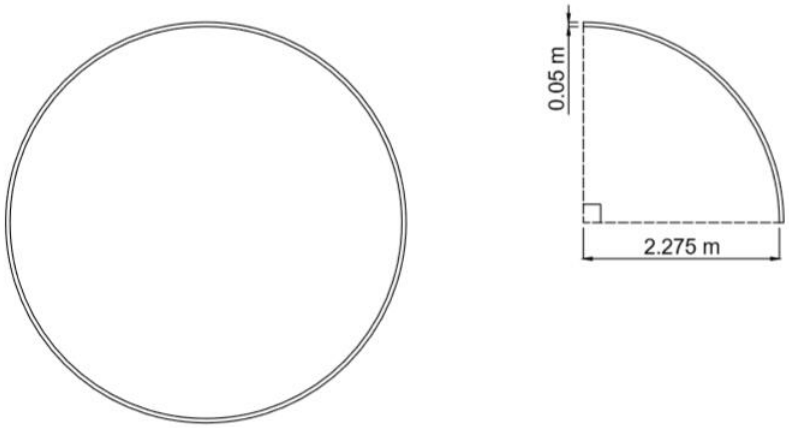

Figure 5.1: The geometry of pile

The monopile is modelled by solid element. It is built by: first, drewing a cross section area of the monopile and then extruding the area 55 m along z-axis. Then, this part is assigned with steel material type (ρ=7850 kg/m^3, E=210 GPa, ν=0.3, plastic behavior in Table 5.1) and homogeneous solid section. The reason for using solid element instead of shell element is that shell structure

will have relatively large distortion and hard to converge when bearing lateral loads, because it is assumed no normal stress in lateral direction.

Table 5.1: Plastic stress-strain relationship for steel [6]

Plastic strain	Plastic stress [MPa]
0	325
0.0052	357.2
0.0119	384.4
0.0185	404.9
0.0258	427.6
0.0349	450.3
0.0451	466.2
0.0669	486.7
0.0832	495.9
0.1019	500.5
0.1200	505.1
0.1369	505. 2

welds

The welds is designed according to AWS [21] and IACS 47 [22] standard. The welding approach is single "V" groove weld. The geometry of welds is shown in Figure 5.2. It is modelled as solid element in ABAQUS. The strength of the welds is not analyzed in this thesis, so the property for welds is assigned as the same with the monopile.

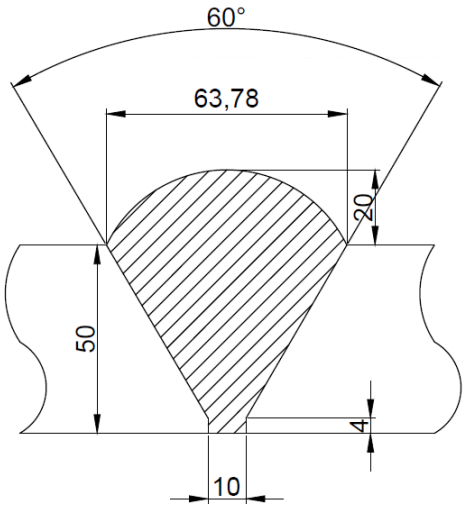

Figure 5.2: Geometry of welds

Hydraulic cylinder

The simplified hydraulic cylinder is shown in Figure 5.3. It cantains two parts: a cylinder fixed in right end, and a piston assembled in the cylinder. In the chamber between bottom of the piston and inner surface of cylinder, hydraulic liquid should be modelled, which provide hydraulic pressure equal in each direction of the inner surface. However, it is hard to model the liquid in finite element software. A spring K-1 instead of hydraulic liquid is built for simplifying calculation. The piston is supported by a hollow square beam. The beam is fixed at the right end. The beam can be simplified as a spring K-2. Its stiffness is calculated in Appendix C.

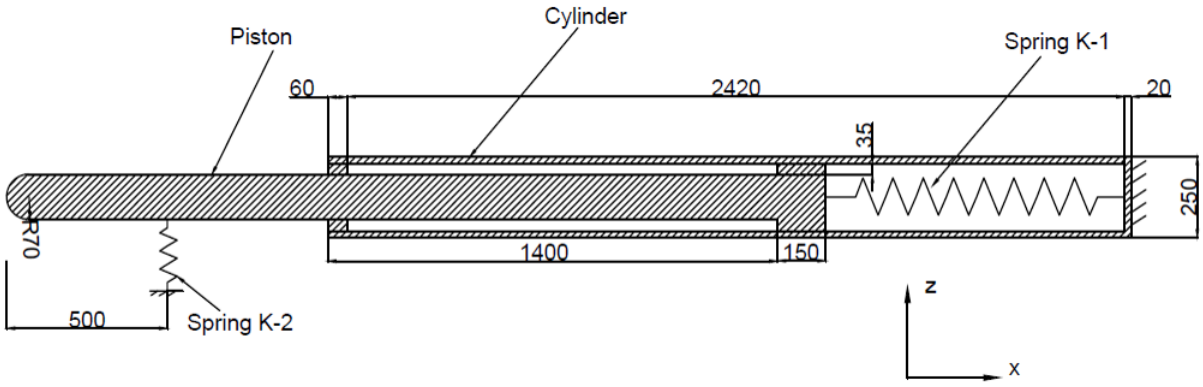

Figure 5.3: Support structure for piston in gripper device

5.2.2 Loads

Hammer load

The hammer load is a impulse load added as a pressure on the pile top. The shape of the load is added in "Amplitude" section by tubular, which has the same shape with the hammer load in section ???, but the peak value is one. The shape function for the hammer load is:

$$\begin{cases} 400 \cdot t & ,0 < t \leq 2.25 \times 10^{-3} \\ -400 \cdot t + 2 & ,2.25 \times 10^{-3} < t \leq 4.5 \times 10^{-3} \\ 0 & ,4.5 \times 10^{-3} < t \end{cases}$$

The magnitude of the pressure is the peak value divided by the cross section area of the pile.

Soil resistance

In soil-structure interaction problem, it is common to model a continuum soil volume. A large soil volume should be modelled to reduce the boundary effect. The soil volume's diameter can be set as 10-30 times of the monopile's diameter. This method has the advantage of percisely analyzing the soil behavior, but, because of the large soil volume, the calculation process is very time consuming. It is necessary to simplify the soil model for calculating more cases. A model contains friction force (representing friction soil resistance) and pressure (representing end-bearing resistance) instead of continuum soil model is built in ABAQUS.

Friction resistance is calculated by API recommended value for undrained clay, which is the same as chapter 3.3. Friction parts, which has a shape of quarter circular ring, contact with the monopile's surface. Normal pressure is added on the surface of friction parts and pushes the parts towards monopile. Interaction including normal and friction behavior is added on the contact surface of friction parts and monopile surface. To express the variations of friction resistance alone depth, the total friction resistance is discretized into several parts along vertical direction. Each part provide friction force equals to the desired friction resistance at the contact area.

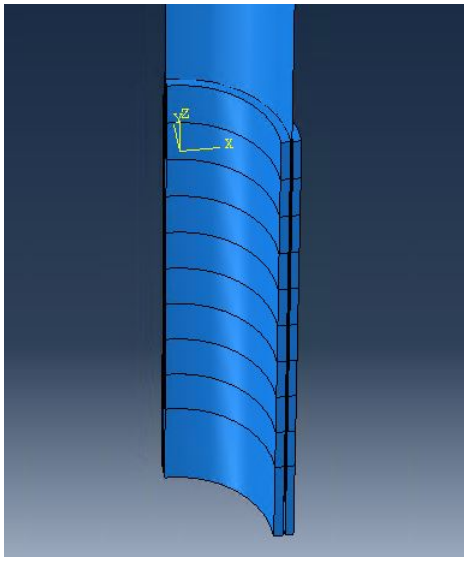

Figure 5.4: The discretized friction parts

End-bearing resistance is calculated by API recommended value for undrained clay. It is

added as pressure at pile toe. Although the unit end-bearing resistance is changing when pile moving downward, it can be assumed constant during one blow because of the small penetration depth.

Spring-K1

Before adding the spring, two coupling constraint should be applied to the bottom surface of piston and cylinder in order to distribute the point load to the total surface, Figure 5.5 and Figure 5.6. The control point if located at the centre of the circular surface for both constraint. The coupling type is set as structural distributing. The constrained degrees of freedom is UR1, UR2, UR3. Other parameters are set as default.

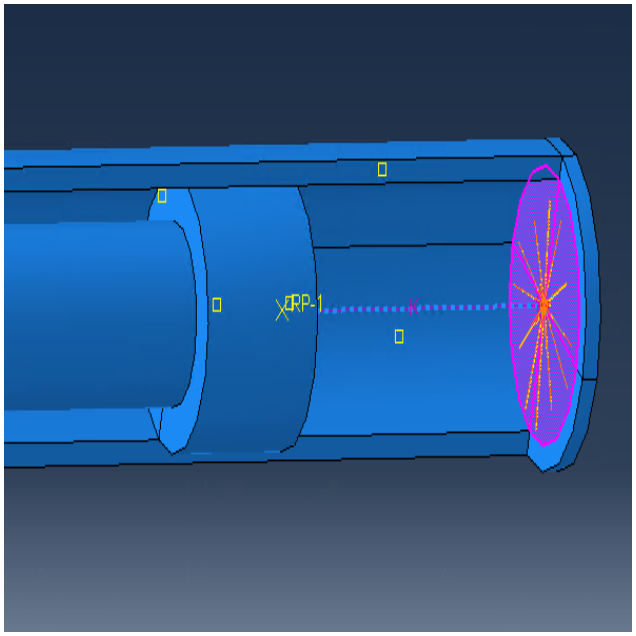

Figure 5.5: Coupling constraint for piston bottom surface

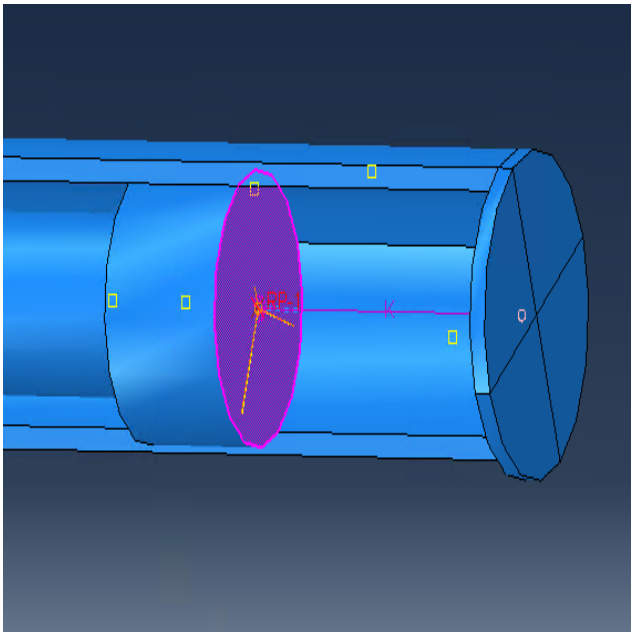

Figure 5.6: Coupling constraint for cylinder bottom surface

A spring is created between the two control points, shown in Figure 5.7. The spring axis is "follow line of action". The spring stiffness is 3×10^7 N/m. No damping is applied.

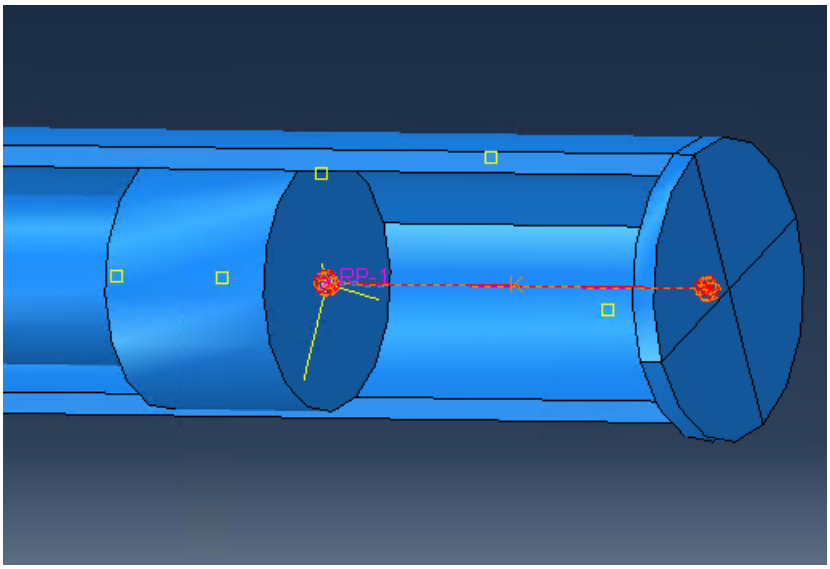

Figure 5.7: Spring K-1

Spring-K2

A structural distributing coupling is applied at one end of the spring-K2, shown in Figure 5.8. The other end of the spring-K2 is connected to a fixed reference point just below the coupling control point. The spring-K2 is shown in Figure 5.9. The axis is set as "Follow line of action". The spring stiffness is 4.89×10^7 N/m. No damping is applied.

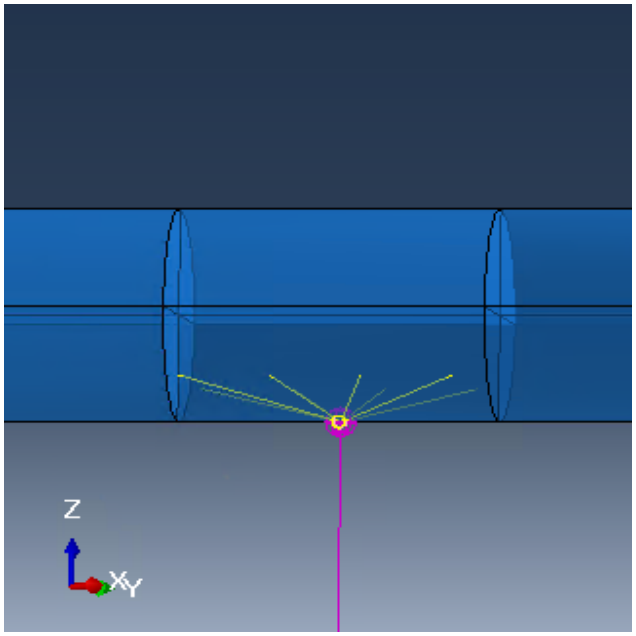

Figure 5.8: Coupling constraint for spring-K2

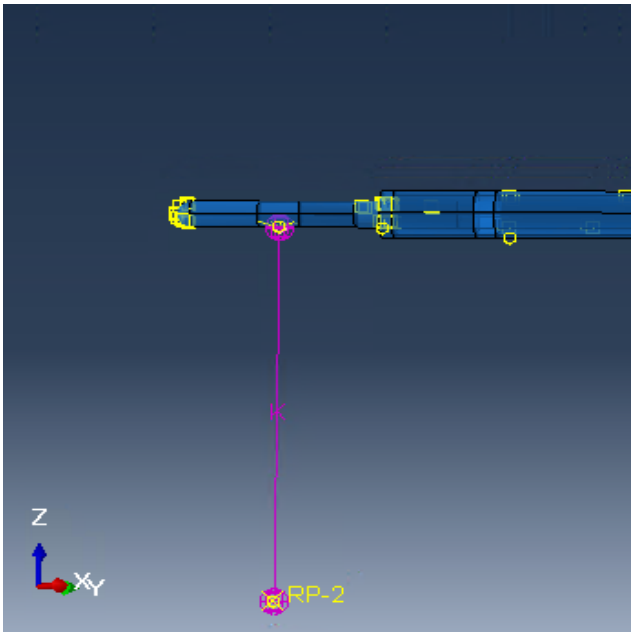

Figure 5.9: Spring K-2

5.2.3 Assembly

The figure of assembly is shown in Appendix D.

5.2.4 Boundary condition

The monopile has two symmetric boundary conditions, shown in Figure 5.10 and Figure 5.11. The X-symmetric boundary condition requires $U1 = UR2 = UR3 = 0$, which means that the particles at this boundary can not have displacement on x direction, and rotation on y and z direction. The Y-symmetric boundary condition requires $UR1 = U2 = UR3 = 0$, which does not allow particles at this boundary to move on y direction and rotate on x and z direction.

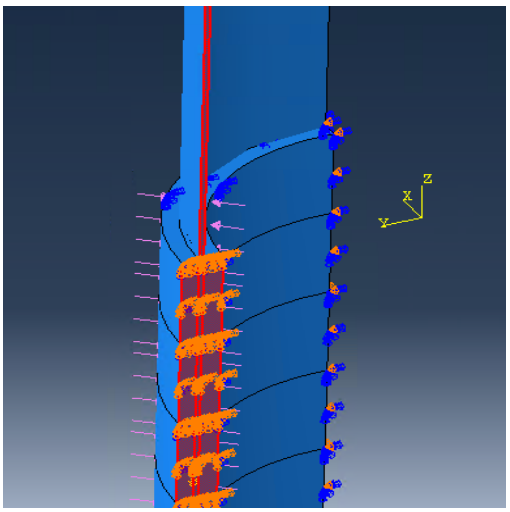

Figure 5.10: X-symmetric

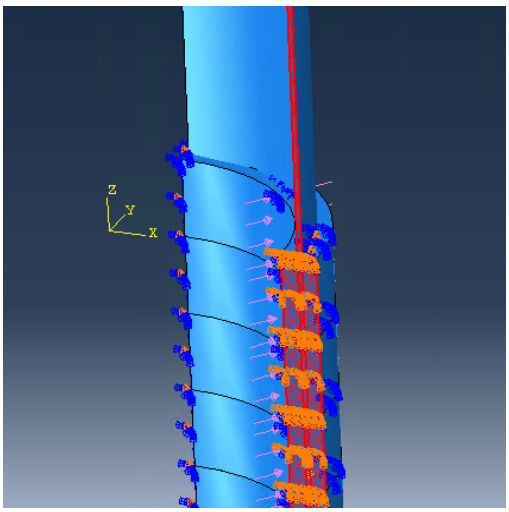

Figure 5.11: Y-symmetric

The friction parts have boundary condition at the up, bottom and side surface. The boundary condition for up and bottom surfaces has four constrained degree of freedom: $U3 = UR1 = UR2 = UR3 = 0$. This boundary condition ensures that the friction parts only have displacement in x-y plane. The side surface has boundary condition: $UR1 = UR2 = UR3 = 0$, which makes the rotation of the friction part to be zero.

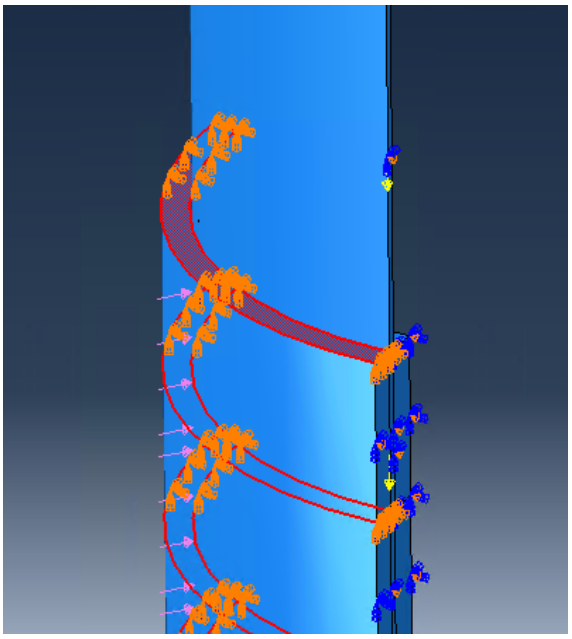

Figure 5.12: Top and bottom boundary condition

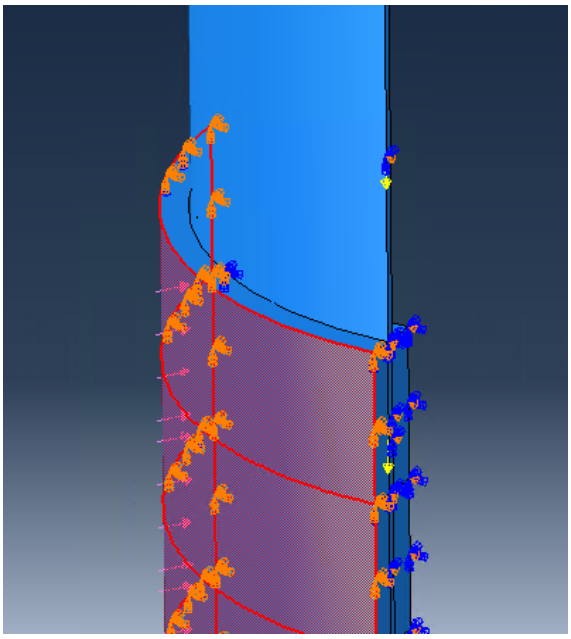

Figure 5.13: Side boundary condition

5.2.5 Interaction

The friction parts contact with the monopile's outer surface. In Abaqus, surface to surface contact pairs are used. There are two contact properties at the contact surface: normal behavior and tangential behavior. "Hard" contact is used for normal behavior. For tangential behavior, the friction formulation is set as penalty. The friction coefficient equals to 0.3 as most used in soil-structure interaction problems. Finite sliding tracking approach is applied. Figure 5.14 shows a contact pair between the first friction part and monopile outer surface. The first surface is marked as red color and the second surface is marked as pink color. This is chosen by the mesh size of the two contact surface. The mesh size in the first surface should be larger than which in the second surface.

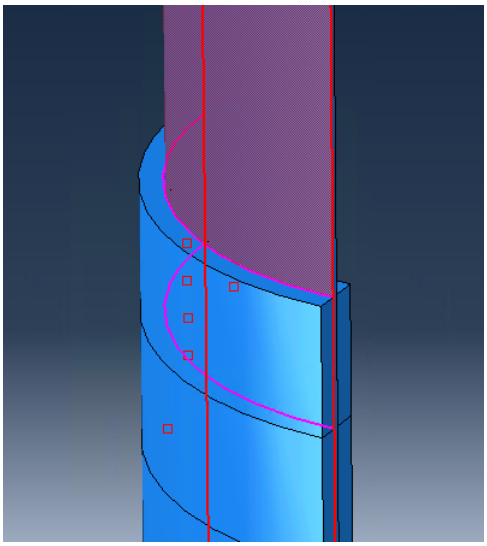

Figure 5.14: Friction part and monopile contact pair

The piston rod contact with inner surface of cylinder. Surface to surface contact pairs are applied at the contact surface. "Hard" contact is used for normal behavior and penalty friction formulation with finite sliding is used for tangential behavior. The friction coefficient is set as 0.1 for lubricated steel-steel friction. Figure 5.15 shows the contact pair between piston head and inner surface of cylinder. Figure 5.16 shows the contact pair between piston rod and cylinder seal. The first and second contact surface is marked as red and pink respectively.

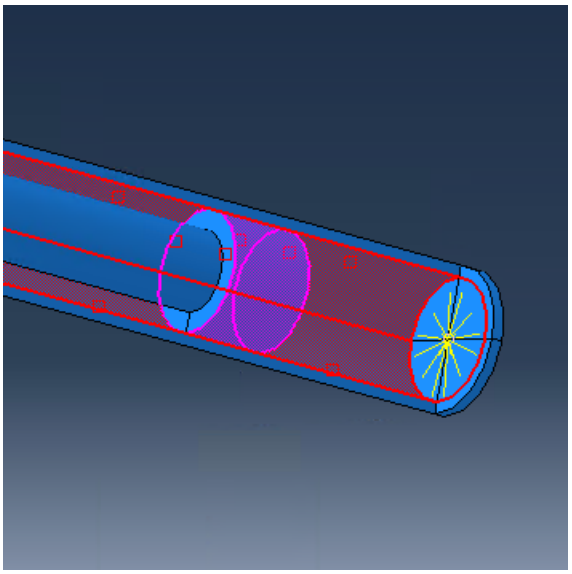

Figure 5.15: Contact between piston head and cylinder inner surface

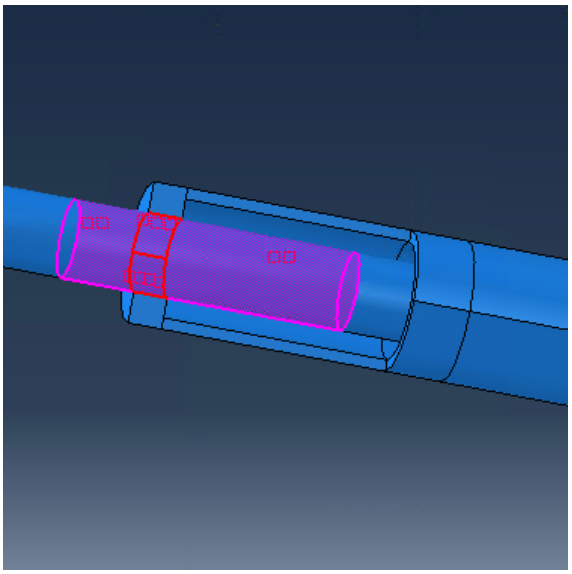

Figure 5.16: Contact between piston rod and cylinder seal

The piston roller contact with the lateral surface of monopile. Surface to surface contact pairs are applied at the contact surface. "Hard" contact is used for normal behavior. This contact is through roller, so the friction can be ignored. From Figure 5.17, Figure 5.18 and Figure 5.19, the contact surfaces can be seen and they are marked the same as before.

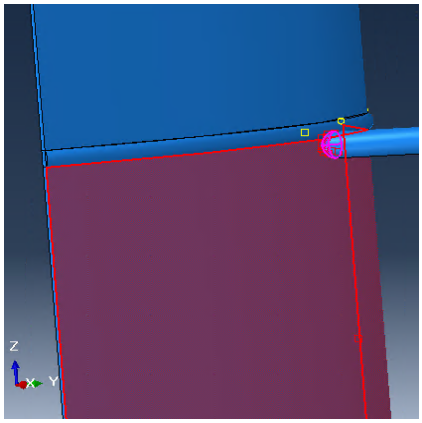

Figure 5.17: Contact between roller and pile

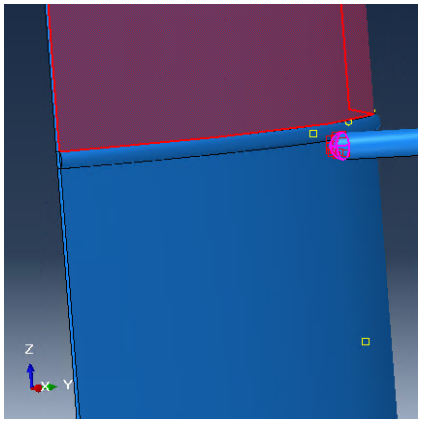

Figure 5.18: Contact between roller and pile

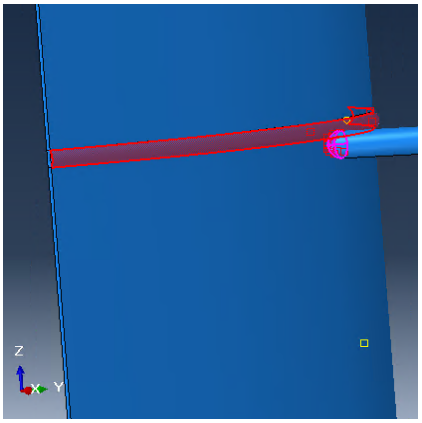

Figure 5.19: Contact between roller and welds

The interaction in the model can be summarized as Table 5.2.

Table 5.2: Summary of contact properties

Contact pair	Discretization	Normal behavior	Tangential behavior		
Friction part-pile	Surface to surface	Hard	Penalty	finite sliding	0.3
Piston head-cylinder	Surface to surface	Hard	Penalty	finite sliding	0.1
Piston rod-cylinder	Surface to surface	Hard	Penalty	finite sliding	0.1
Roller-pile	Surface to surface	Hard	-	-	-
Roller-welds	Surface to surface	Hard	-	-	-

5.2.6 Mesh

The element type is C3D8R (Continuum, 3D, 8 node, Reduced integration), which has a shape of linear brick and property of hourglass control [23].

The thickness of welds is very small, and the shape of the welds' cross section area is semi-circle, which is hard to represent by brick element. To capture the shape of the welds' cross area precisely, small element size should be used, which is 0.008 m.

It can be seen in Figure 5.20 that the curved surface in welds is represented by 12 small flat surface.

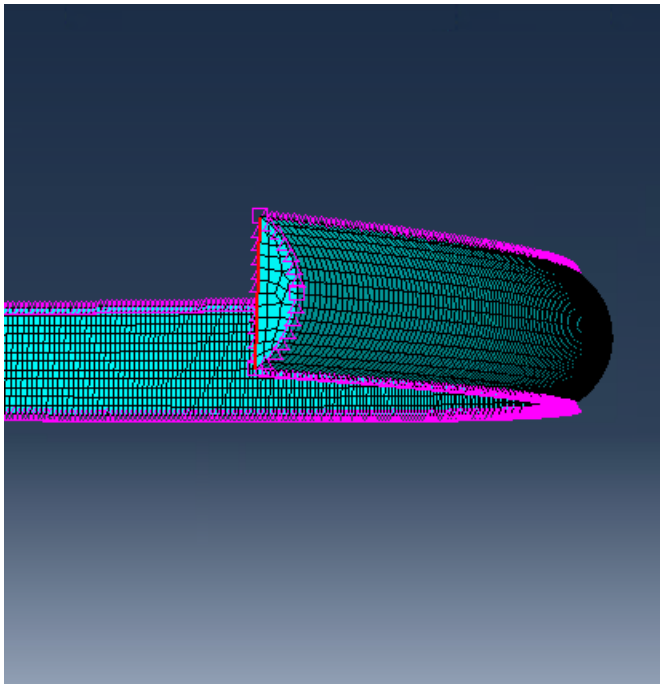

Figure 5.20: welds mesh

The mesh for the monopile is shown in Figure 5.21. Except for the area which contacts with welds, the monopile's surfaces are seeded by global size. The global mesh size for monopile will be studied in sensitivity check. Due to very fine mesh on welds, the area contact with welds on monopile should be meshed finer than other area, in order to capture the contact behavior between monopile surface and welds, Figure 5.22. The mesh size for contact area is 0.008 m.

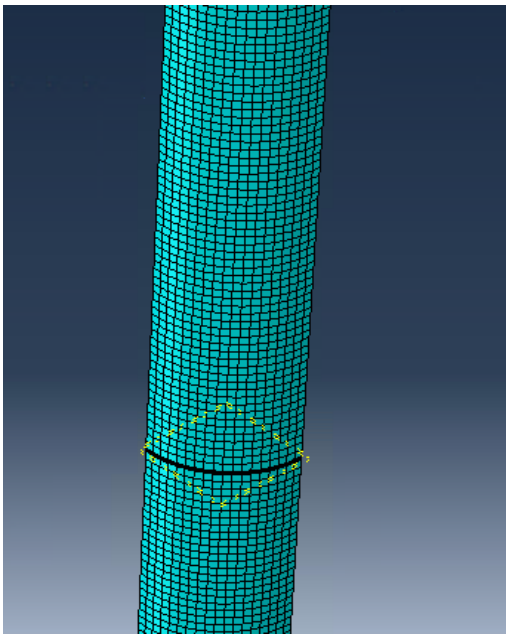

Figure 5.21: Monopile mesh

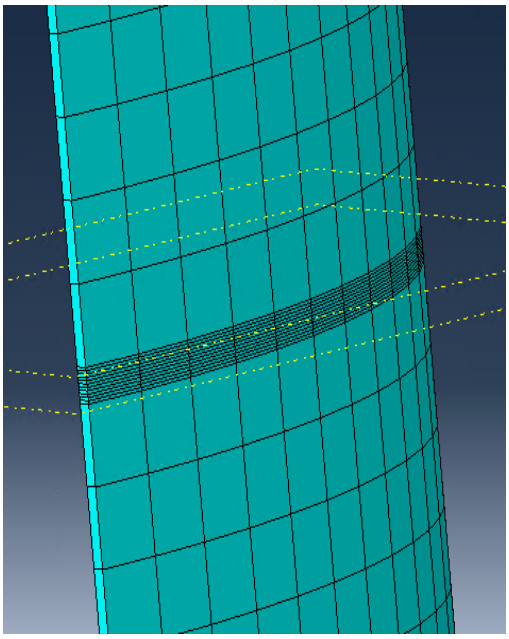

Figure 5.22: Monopile contact area (with welds) mesh

There are three contact area on the surface of piston: one with monopile and welds; two with cylinder. The mesh for these area should be very fine to capture the contact behavior. Three datum plane are created to help meshing. The first datum plane is located at the connection between hemisphere and piston rod. The second and third datum plane is located 0.1 m before and behind the contact area of piston rod and cylinder seal. The mesh size for hemisphere is 0.004 m. The mesh size for contact area of piston and cylinder is 0.01 m.

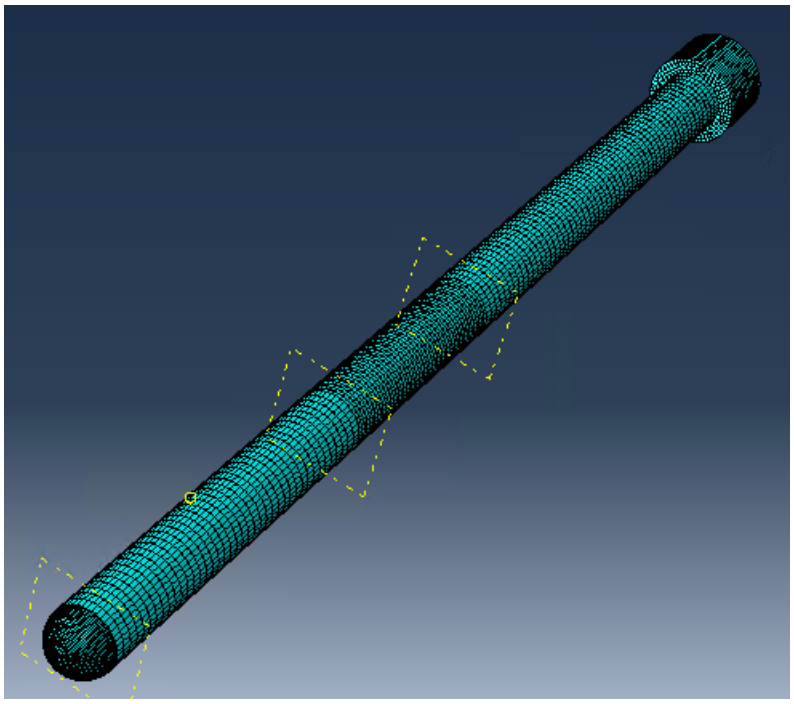

Figure 5.23: Piston mesh

The mesh size for friction part is 0.1 m, shown in Figure 5.24.

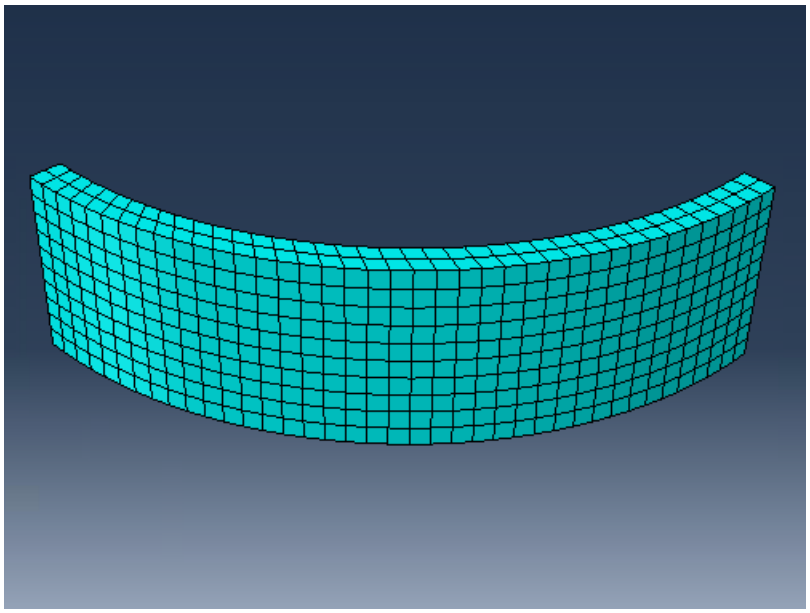

Figure 5.24: Friction part mesh

The mesh size for cylinder is 0.02 m, shown in Figure 5.25

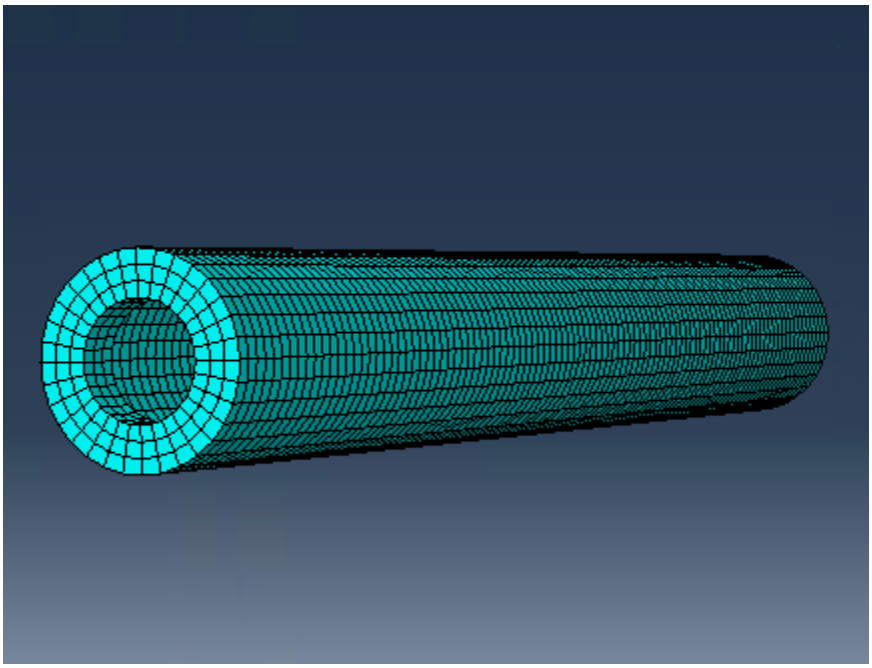

Figure 5.25: Cylinder mesh

5.2.7 Mesh sensitivity check

In order to verify whether the mesh size is appropriate for calculation, a mesh sensitivity check should be carried out. In mesh sensitivity check, the mesh size for contact area will not change due to high fineness of mesh size. The global mesh size for different parts will be changed by five level: very coarse, coarse, medium, fine, very fine. The control parameter is von Mises stress at a point on cylinder and the nearest point on piston, shown in Figure 5.26. This point contacts with the lowest point of piston. It will bear the largest load during piston vibration, so it has the largest possibility to fail.

The global mesh size for each part and each coarseness level is shown in Table 5.3. It can be seen that changing the mesh size from "very coarse" level to "coarse" level, the corresponding stress on piston will change from 0.412 GPa to 0.245 GPa (changing 40 %), which does not satisfy the convergent requirement. Changing mesh size from "coarse" level to "medium" level, the corresponding stress on piston changes from 0.245 GPa to 0.244 GPa (changing 0.4 %), and the corresponding stress on cylinder changes from 0.157 GPa to 0.159 GPa (changing 1.2 %). So, during following calculation, the global mesh size is chosen as "coarse" level, which provides great preciseness and time efficiency.

Table 5.3: The global mesh size for different part and coarseness level and corresponding stress

Coarseness level	Monopile	Piston	Cylinder	Soil piece	Mean von Mises stress	
					Piston [GPa]	Cylinder [GPa]
Very coarse	0.5	0.05	0.03	0.17	0.412	0.230
Coarse	0.4	0.04	0.03	0.17	0.245	0.157
Medium	0.3	0.03	0.03	0.17	0.244	0.159
Fine	0.2	0.02	0.02	0.1	0.244	0.160
Very fine	0.1	0.02	0.01	0.05	0.245	0.158

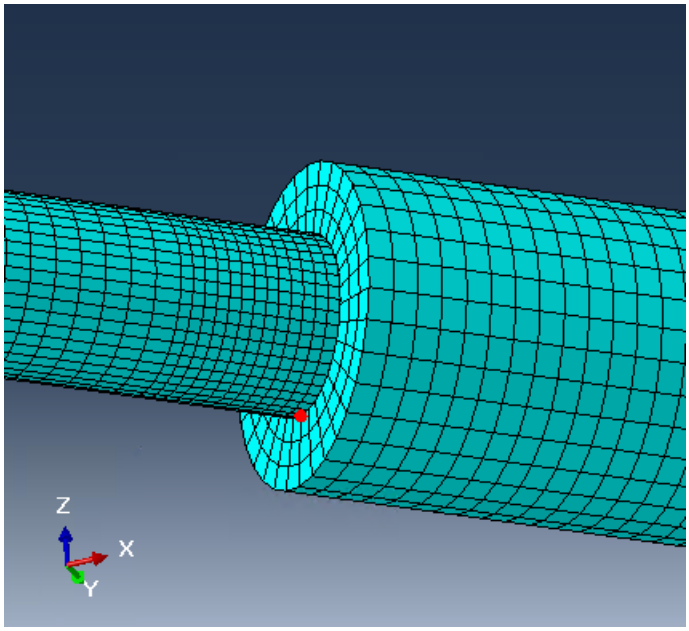

Figure 5.26: The chosen point

5.3 Eigenmodes analysis

5.3.1 Natural frequency for piston-cylinder assembly

Using step "Frequency" in "Linear perturbation" procedure type, the eigenfrequency for the piston-cylinder assembly model is shown in Table 5.4.

Table 5.4: Natural frequency for piston-cylinder assembly

Mode No.	Natural frequency [Hz]
Mode 1	70.62
Mode 2	104.76
Mode 3	169.51
Mode 4	206.64
Mode 5	267.35
Mode 6	275.97

The first and second corresponding eigenmode shapes are shown in Figure 5.27 and Figure 5.28 respectively. The first eigenmode shape depicts a bending motion of piston in x-y plane. The second eigenmode shape depicts a bending motion of piston in vertical plane. The color represents for the magnitude of displacement. In these two eigenmode shapes, it can be seen that the left end of the piston has the maximum displacement. The cylinder is almost stand still except for a small displacement at the connection area with piston.

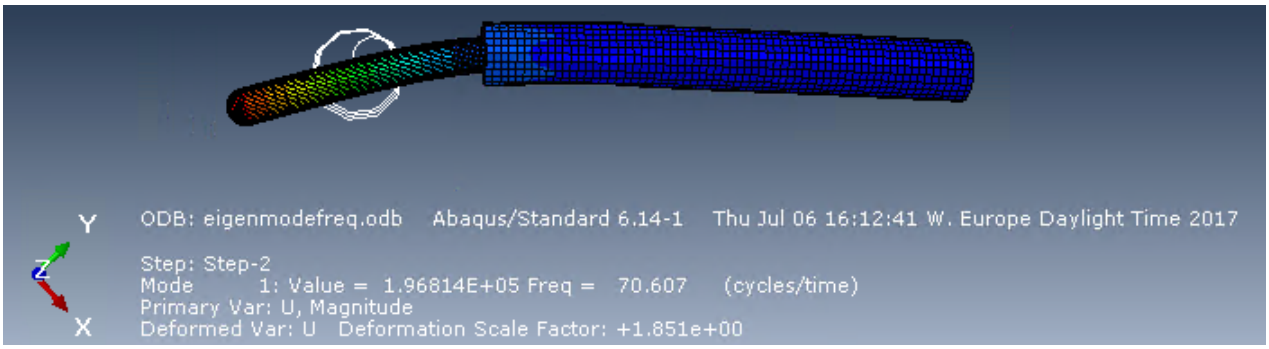

Figure 5.27: The first eigenmode shape of piston-cylinder assembly (view from top)

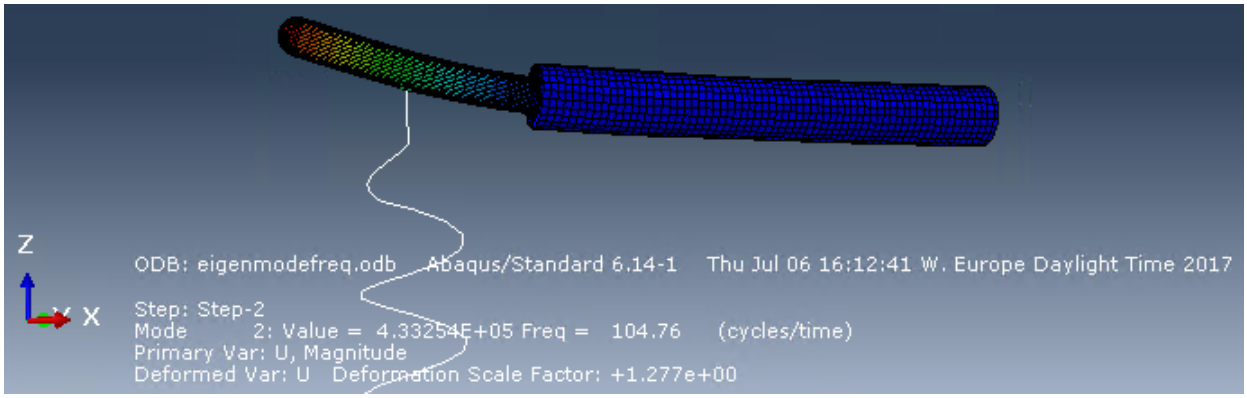

Figure 5.28: The second eigenmode shape of piston-cylinder assembly (view from side)

The motion following first eigenmode shape will occur only if there is horizontal bending disturbance. In the piston-welds colliding problem, vertical load and horizontal axial load on the piston are the dominant loads, and horizontal bending load will not occur. So, the first eigenmode shape will not be concerned as an important mode shape. The second eigenmode shape will play a dominant role in the colliding procedure between piston and welds because the colliding load is in vertical direction, which will be proved later. Besides the second eigenmode shape, the forth, the fifth eigenmode shape also depicts the vertical motion of piston-cylinder assembly. The higher eigenmode shapes involves cylinder buckling and higher eigenmode shapes of piston. Because of high natural frequency, they contributes less to the motion of the system than the second eigenmode shape. The higher eigenmode shapes can be founda in Appendix A.

5.3.2 Axial vibration natural frequency

The axial vibration of the piston can be treated as a rigid body vibration with spring support. The equation of motion for this vibration is:

$$-\omega_n^2 M_{piston} + K_1 = 0 \tag{5.1}$$

where,

M_{piston} = the mass of the piston,

K_1 = the stiffness of spring K1.

Rearrange the Eq. 5.1, the natural frequency for the piston axial vibration can be derived as:

$$\omega_n = \sqrt{K_1 / M_{piston}} = 301.1 \qquad \text{[rad/s]} \tag{5.2}$$

5.3.3 Natural frequency for soil supported monopile

Using the same method with section 5.3.3, the natural frequency for the soil supported monopile can be estimated. Most of the eigenmode shape for the monopile only have deformation in horizontal direction, which does not contribute much for the vertical piston vibration. These kinds of eigenmode shapes is not concerned in the calculation. These natural frequencies and corre-

sponding eigenmode shapes can be found in Appendix B.

There is one eigenmode shape that discribes the vertical deformation of the monopile, shown in Figure 5.29. This is the ninth eigenmode shape. The natural frequency for this eigenmode shape is 28.71 Hz (180.39 rad/s). In this eigenmode shape, the particles on monopile only have in-plane vibration.

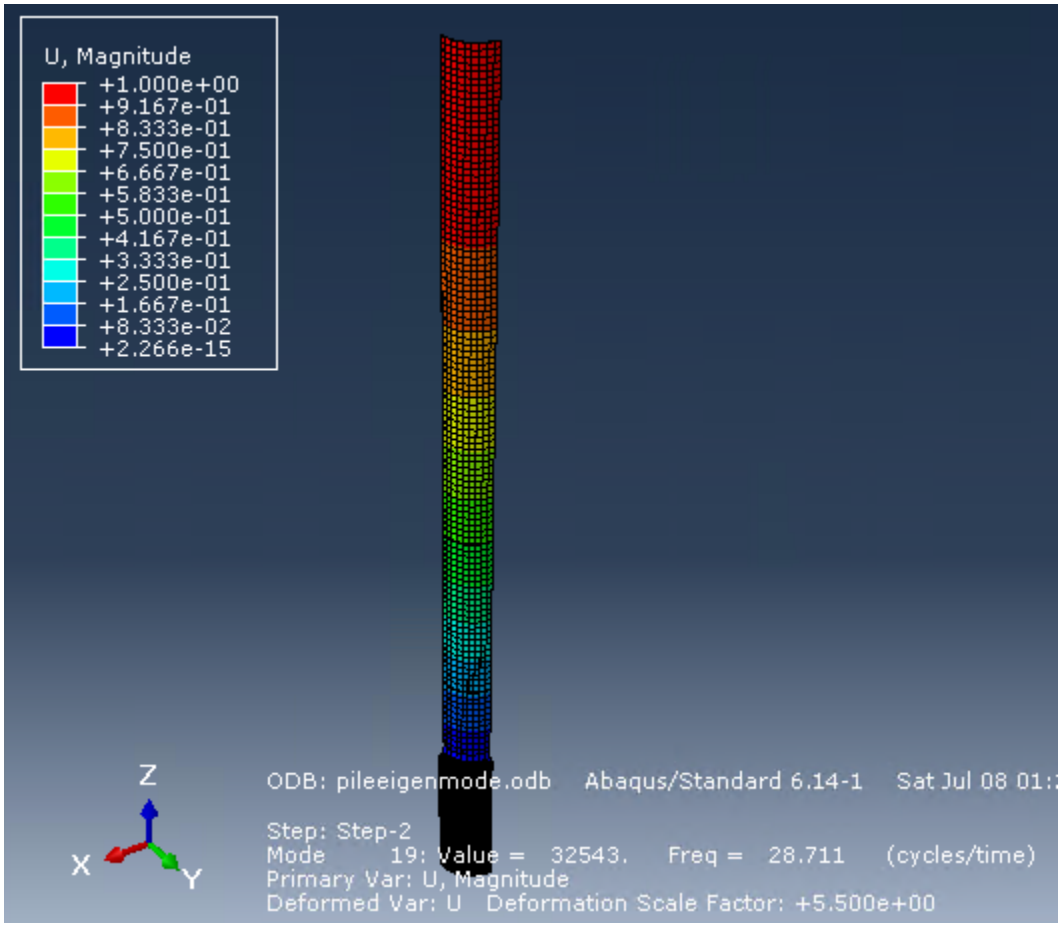

Figure 5.29: The ninth eigenmode shape for the soil supported monopile

5.4 Piston decay test

In order to analyze the piston motion and natural frequency, two piston decay tests should be carried out: 1) one in vertical direction, Figure 5.30; 2) the other in horizontal direction,Figure 5.31. A concentrated force is applied at the roller (the left point on the piston), which has a constant amplitude of 17000 N with duration of 0.005 s in vertical load decay test, and 25000 N with

duration of 0.01 s. The load amplitude in vertical decay test is smaller than which in horizontal load test for protecting the structure from yielding. In vertical load decay test, the force direction is along -z axis. In horizontal load decay test, the force direction is along the axial direction of piston. It should be noticed that the friction between the piston and the cylinder is removed in horizontal load decay test in order to eliminate the mean offset, which will induce redundant peak in the motion spectrum.

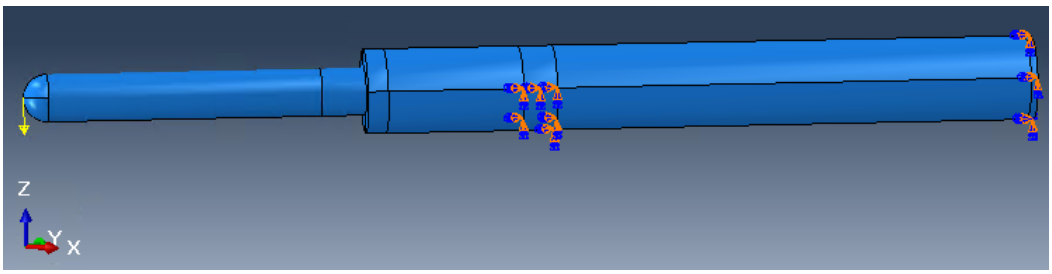

Figure 5.30: Vertical load decay test model

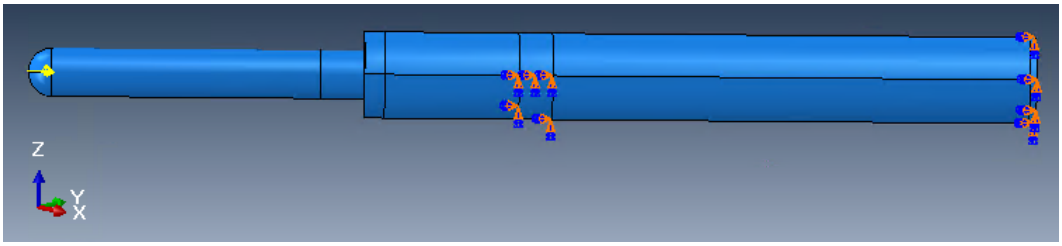

Figure 5.31: Horizontal load decay test model

Figure 5.32 shows the vertical displacement at the node which the vertical load is applied. It can be seen that the point will oscillate around 0 m and the amplitude is damping along time. The damping is caused by the friction between piston and cylinder. The vertical displacement of the roller causes horizontal movement. The friction between piston and cylinder is always working against the horizontal movement and consuming the energy of the system.

Figure 5.33 shows the spectrum of the vertical motion. The spectral density is concentrated at frequency equals to 650 rad/s (103.5 Hz), which is corresponding to the second natural frequency. There is no peak around the other natural frequency, which means they are not excited by the vertical load.

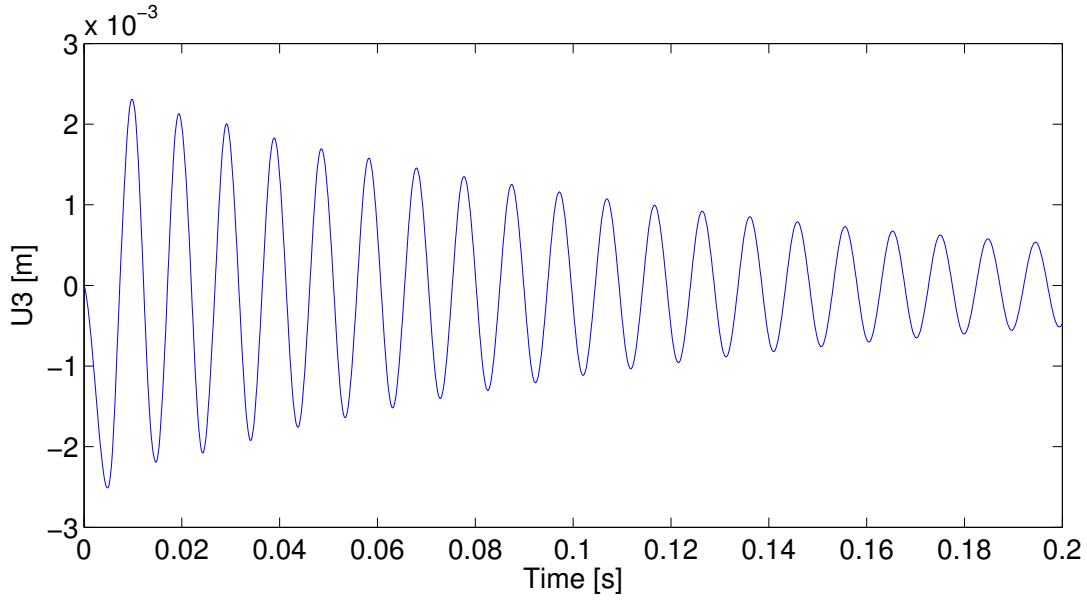

Figure 5.32: Vertical displacement

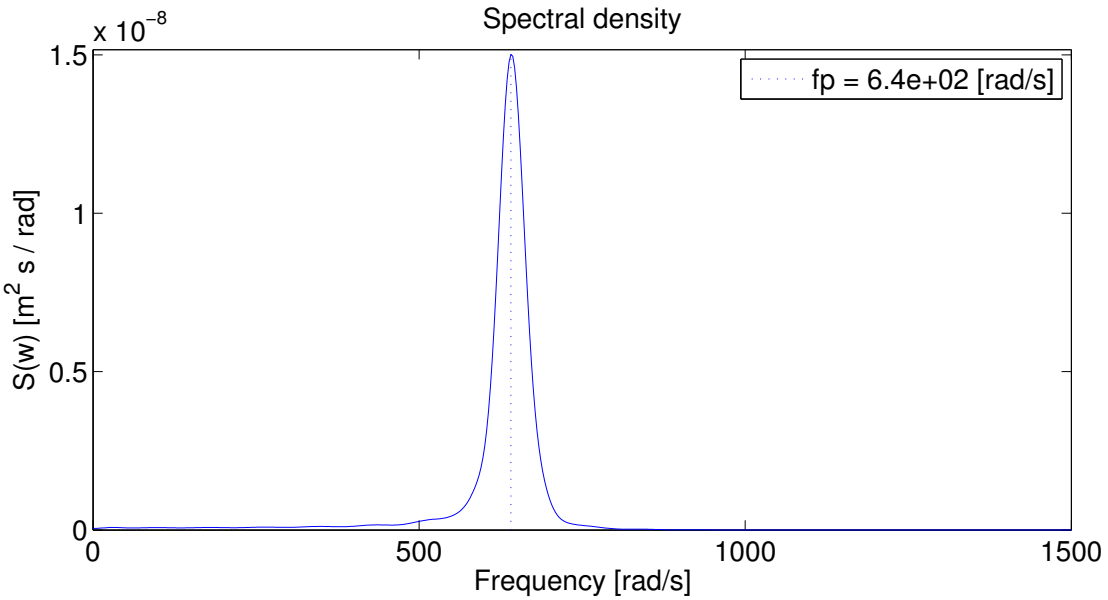

Figure 5.33: Spectrum for Vertical displacement

Figure 5.34 shows the horizontal displacement at the point, which the decay load applied on, in horizontal load decay test. The chosen point will oscillate around a mean position. There is no damping in the horizontal vibration due to removal of friction, so the amplitude of the vibration is constant. The natural frequency for the horizontal vibration is around 300 rad/s (47.7 Hz), which is smaller than the natural frequency of vertical vibration, and it matches with the

natural frequency calculated by hand in section 5.3.4. So, in axial decay test, the piston's motion can be treated as a rigid body motion where no eigenmode shape for deformation occurs.

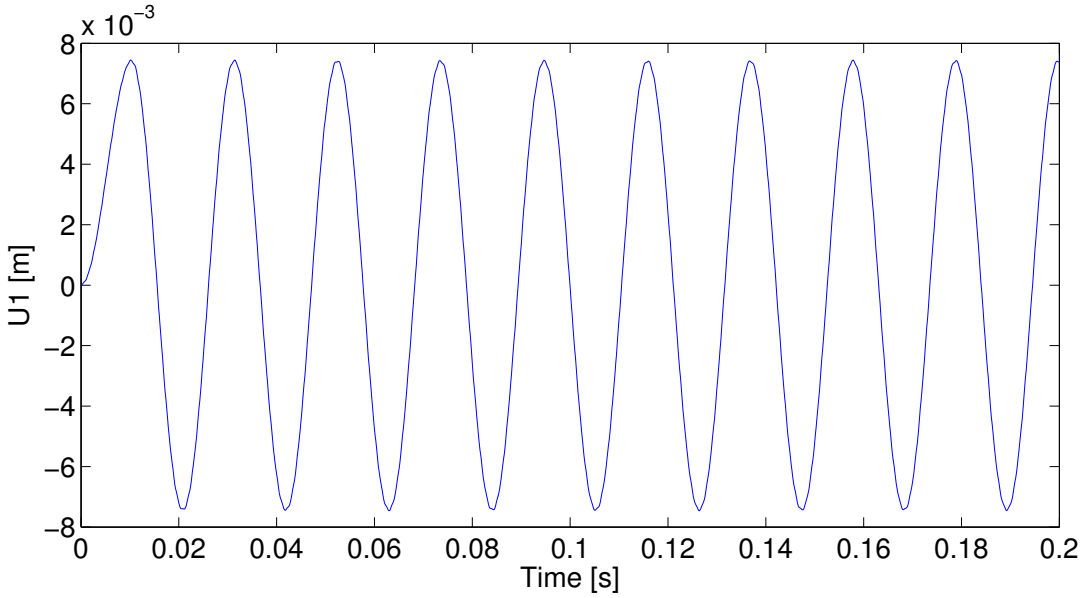

Figure 5.34: Horizontal displacement

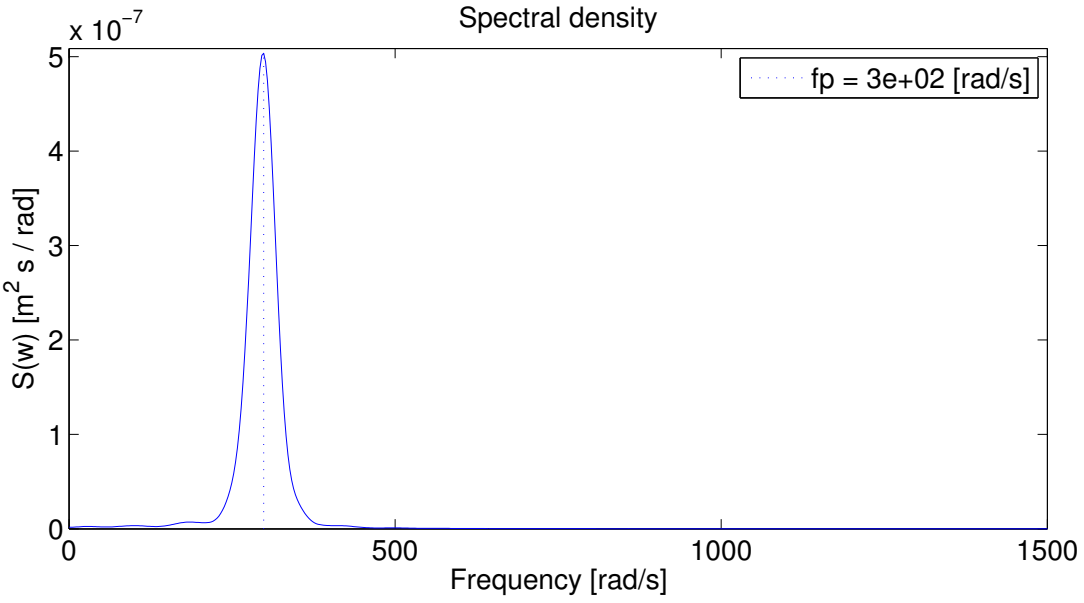

Figure 5.35: Spectrum for horizontal displacement

5.5 Choosing point for output data

In order to find whether the piston and cylinder is yielded, the maximum stress in both structure should be found. Regarding the piston as a cantilever beam (Figure 5.36), when bearing constant compressive load and vertical bending moment, the stress for the cross sectional area is not evenly distributed.

The mean value of the stress in the cross sectional area is caused by the constant compressive load. The moment causes unevenly distributed stress. At the top of the piston, the stress caused by moment is tensile stress. This stress reduces the amplitude of the stress caused by constant compressive load, which makes the top of the piston bear less load. At the bottom of the piston, the stress caused by moment is compressive stress. This stress has the same direction with the stress caused by constant compressive load, which contributes to more total load at the bottom of the structure. As a result, the horizontal stress component in horizontal direction (S11, S22) has maximum value at the bottom of the piston.

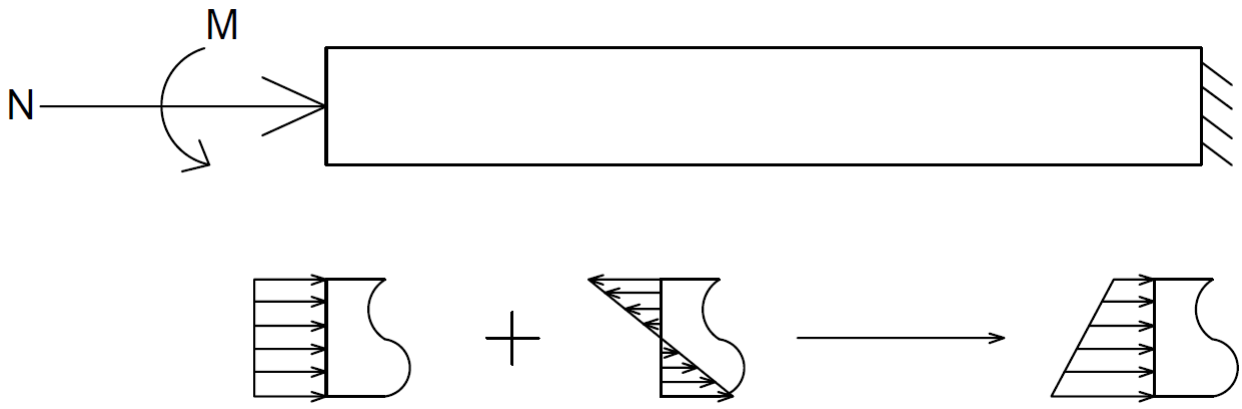

Figure 5.36: Stress distribution of a beam bearing constant compressive load and moment

In vertical direction, the piston is mainly supported by the cylinder. So, the stress component for the vertical direction (S33) has maximum value at the contact point between cylinder and piston.

Considering all stress component above, the point bearing maximum stress should be chosen as the bottom contact point between piston and cylinder.

Except for the point chosen for stress analysis, the point represents for the motion of piston

should be selected. The point which is located at the left end of the roller is chosen for the displacement analysis.

In summary, One point from piston (Figure 5.37) and one point from cylinder (Figure 5.38) is chosen for stress analysis. One point from roller (Figure 5.5) is chosen for displacement analysis.

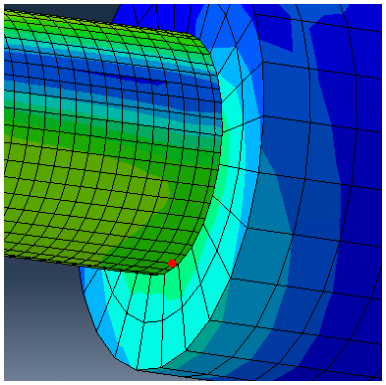

Figure 5.37: Point chosen for stress output on piston

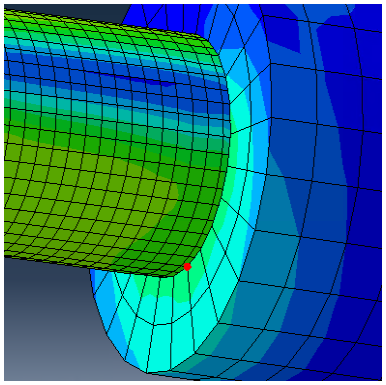

Figure 5.38: Point chosen for stress output on cylinder

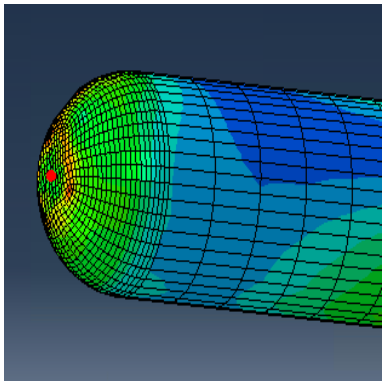

Table 5.5: Point chosen for displacement output on roller

5.6 Verification of input hammer load and soil resistance

The soil resistance and hammer loads in the finite element model is calculated by the rigid pile model. Whether these load works properly should be checked before further calculation. This case will check the motion in ABAQUS simplified model (no gripper device) and compare the motion with which calculated by rigid pile model.

Then, the stress wave theory should be examined whether it is suitable for the finite element model.

The initial condition is given as:

- initial penetration depth: 10 m,
- hammer drop energy: 200 kJ,
- time step: 2.5×10^{-7} s

The output result is abstracted from a point located 26 m below the pile top, shown in Figure 5.39.

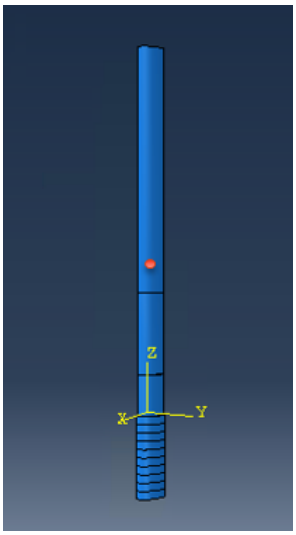

Figure 5.39: The point chosen for output result

The reflected stress wave does not overlap the incident stress wave at this point, so it is clear to see the shape of displacement, stress, particle velocity and the relationship between stress and particle velocity.

The settlement for the pile is shown in Figure 5.40. It can be seen that the blue curve, which represents for the settlement calculated by ABAQUS simplified model, has several jerks and the mean value is approximately following the settlement calculated by rigid pile model (represented by black curve). The final settlement from ABAQUS simplified model is -0.03645 m, which slightly less than the settlement calculated by rigid pile model -0.03707 m. So, this two model can be assumed in the same condition. The reason for the difference of this two final settlement is that the friction part in the finite element model is not perfectly contact with the monopile surface, especially when stress wave passes by. The horizontal strain induces horizontal deformation. The shape of the horizontal deformation depends on the stress wave pattern. In the most time, it seems like a semicircular protrusion. The semicircular shape of monopile's surface can not contacts with the flat friction part's surface perfectly, so some friction is not counted where the two surface does not contact. It is beneficial to adjust the pressure added on the friction part manually by multiplying a scaling factor.

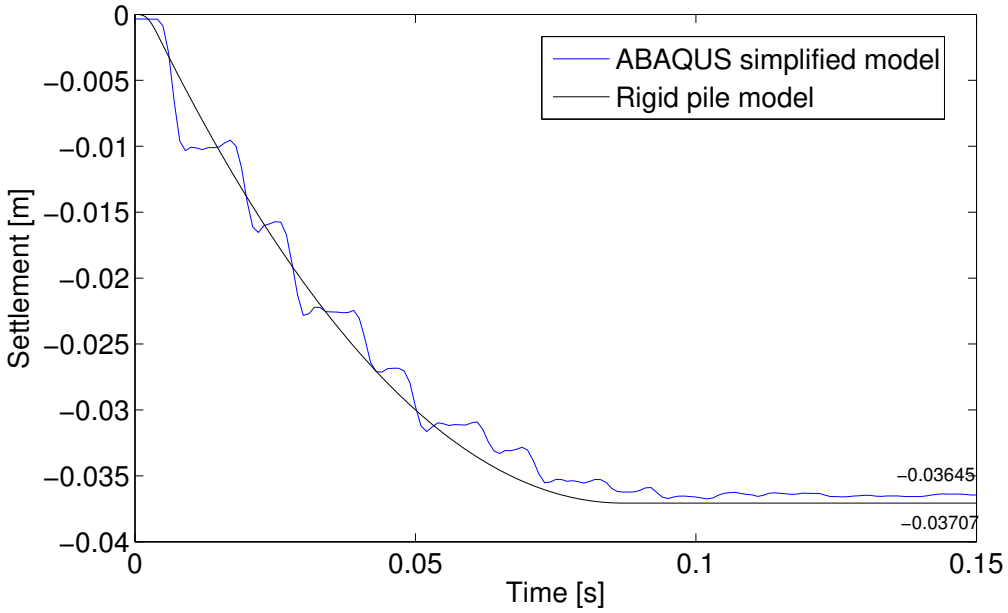

Figure 5.40: Settlement calculated by rigid pile model vs ABAQUS simplified model

The stress wave in the monopile is shown in Figure 5.41. The stress wave has a large amplitude in the center, and it is decreasing when moving far away from center. When the stress wave propagating in the monopile, it keeps the save pattern as Figure 5.41 shows. While it reaches the end of monopile, the stress at the end should be zero and the reflected stress wave neutralizes the incident stress wave, Figure 5.42.

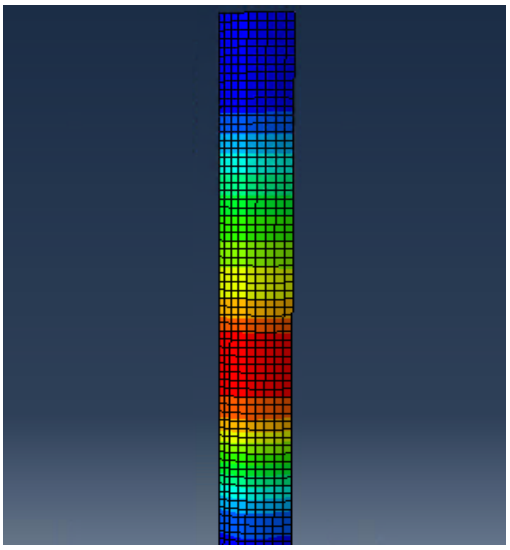

Figure 5.41: Stress wave propagating in monopile

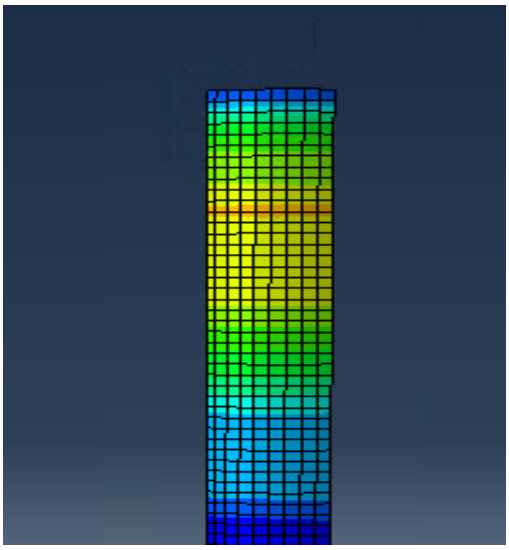

Figure 5.42: Stress wave reflecting in one end of monopile

The stress for the chosen point is shown in Figure 5.43. It can perfectly represent the stress wave propagating without overlapping. Every time the stress wave pass the point, it changes sign because of reflection. The first peak is negative, which represents a compressive stress. The second peak is positive, which represents a tensile stress. The time when the first negative stress peak encounters the point is 0.007 s. The time when the second negative stress peak encounters the point is 0.028 s. Between these two time point, the stress wave has propagated two pile length. Comparing with the result calculated by stress wave theory in chapter 4.3, which the time for stress wave to pass two pile length is 0.0212 s, the result is similar. The stress wave theory for calculating the propagation velocity is suitable for analyzing the monopile hammering problem.

It can be seen in Figure 5.43 that the stress amplitude is reduced each time it is reflected back from pile toe. The soil consumes the energy from stress wave by the work of soil resistance. The stress amplitude does not change when it is reflected at the pile top, because the pile top is free end which does not consume energy.

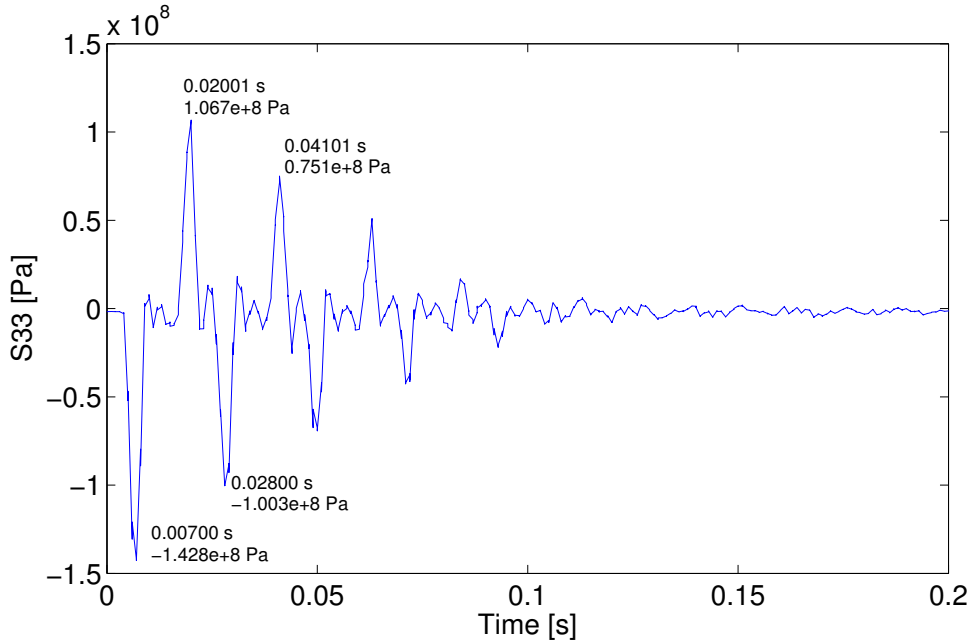

Figure 5.43: Stress calculated by ABAQUS simplified model

The particle velocity at the chosen point is shown in Figure 5.44. No matter what the peak stress sign is, the peak particle velocity is always in the same direction. When the peak stress is

negative, the particle above the chosen point pushes the point downward due to compressive stress. When the peak stress is positive, the particle below the chosen point pulls the point downward due to tensile stress.

The amplitude of the particle velocity has the same trend with the stress. The first peak particle velocity is the largest among others. The second peak particle velocity is less than the first one but equal with the third one. According to the relationship between particle velocity and stress in stress wave theory (chapter 4.4), the particle velocity is proportional to stress, and can be derived as:

$$\sigma_{33} = \sqrt{E\rho} \cdot v = 4.0602 \cdot 10^7 \cdot v \tag{5.3}$$

where,

σ_{33} = stress component in vertical direction,

v = particle velocity.

The first four peak particle velocity is checked for this theory. The amplitude for the first peak particle velocity is 3.519 m/s. The amplitude for the second peak particle velocity is 2.766 m/s. The amplitude for the forth peak particle velocity is 1.943 m/s. Substituting these three values in the Eq. 5.3, the corresponding stress is:

$$\sigma_{33,1st} = 4.0602 \cdot 10^7 \cdot 3.519 = 1.4288 \cdot 10^8 \quad \text{[Pa]}$$

$$\sigma_{33,2nd} = 4.0602 \cdot 10^7 \cdot 2.766 = 1.1230 \cdot 10^8 \quad \text{[Pa]}$$

$$\sigma_{33,4th} = 4.0602 \cdot 10^7 \cdot 1.943 = 0.7889 \cdot 10^8 \quad \text{[Pa]}$$

The comparison between theoretical stress and FEM test stress is shown in Table 5.6. It can be seen that the theoretical stress for the first peak can fit the FEM test stress perfectly. The following theoretical stress has a larger error compared with the first one, but the error is still in a allowable range.

Table 5.6: Comparison between theoretical stress and FEM test stress

	Theoretical stress [$\times 10^8$ Pa]	FEM test stress [$\times 10^8$ Pa]	error [%]
$\sigma_{33,1st}$	1.4288	1.428	0.06
$\sigma_{33,2nd}$	1.1230	1.067	4.99
$\sigma_{33,4th}$	0.7889	0.751	4.80

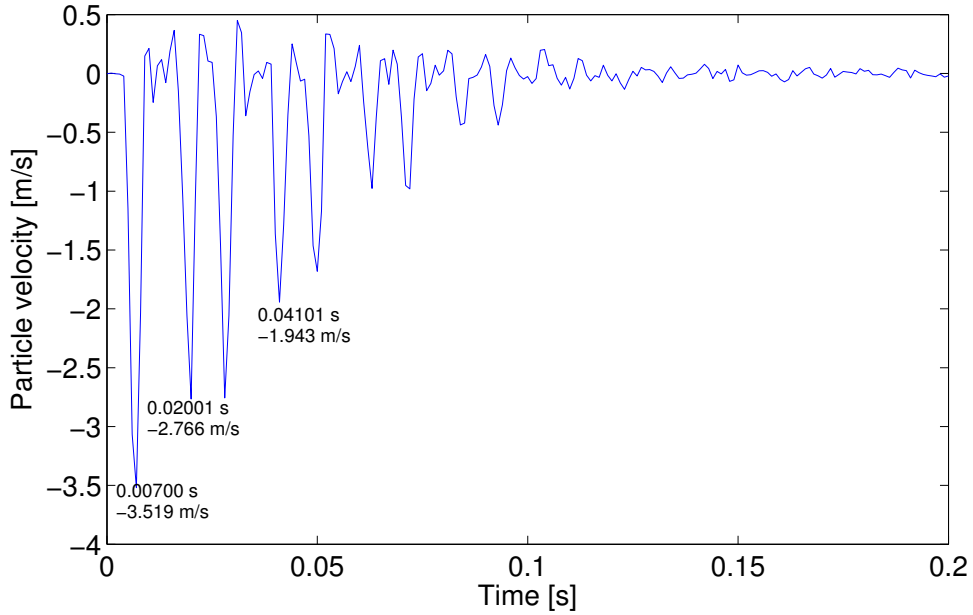

Figure 5.44: Velocity calculated by ABAQUS simplified model

So, it can be concluded that the soil resistance and hammer load inserted in the Abaqus model is verified. The stress wave theory is suitable for analyzing the monopile installation problem in Abaqus.

Chapter 6

Parametric study

6.1 Set up for load cases

Based on the finite element model built in chapter 5, some load case is set to analyze the effect of changing different parameters. The load cases is defined as Table 6.1.

Table 6.1: Set up for load cases

	Welds	No. of stroke	Initial penetration depth [m]	Welds thickness [mm]	Hammer energy [kJ]	Cylinder force [kN]	$Z_{gripper}$ [m]
Case 1	×	1	10	20	200	400	15
Case 2	✓	1	10	20	200	400	15
Case 3	✓	6	10	20	200	400	15
Case 4	✓	3	20	20	200	400	15
Case 5	✓	3	10	10	200	400	15
Case 6	✓	3	10	20	600	400	15
Case 7	✓	3	10	20	200	300	15
Case 8	✓	3	10	20	200	400	31.8

The purpose of setting up the load case is:

- Compare case 1 and case 2: the difference between piston contacting with smooth monopile surface and piston contacting with welds can be analyzed;
- Compare case 2 and case 3: the difference between single stroke and multiple stroke can be analyzed;

- Compare case 3 and case 4: the difference between 10 m initial penetration and 20 m initial penetration can be seen;
- Compare case 3 and case 5: the difference between 20 mm and 10 mm welds' thickness can be got;
- Compare case 3 and case 6: the difference between 200 kJ and 600 kJ hammer energy can be analyzed;
- Compare case 3 and case 7: the difference between 400 kN and 300 kN cylinder force can be seen;
- Compare case 3 and case 8: the difference between two gripper position can be analyzed.

6.2 Case 1

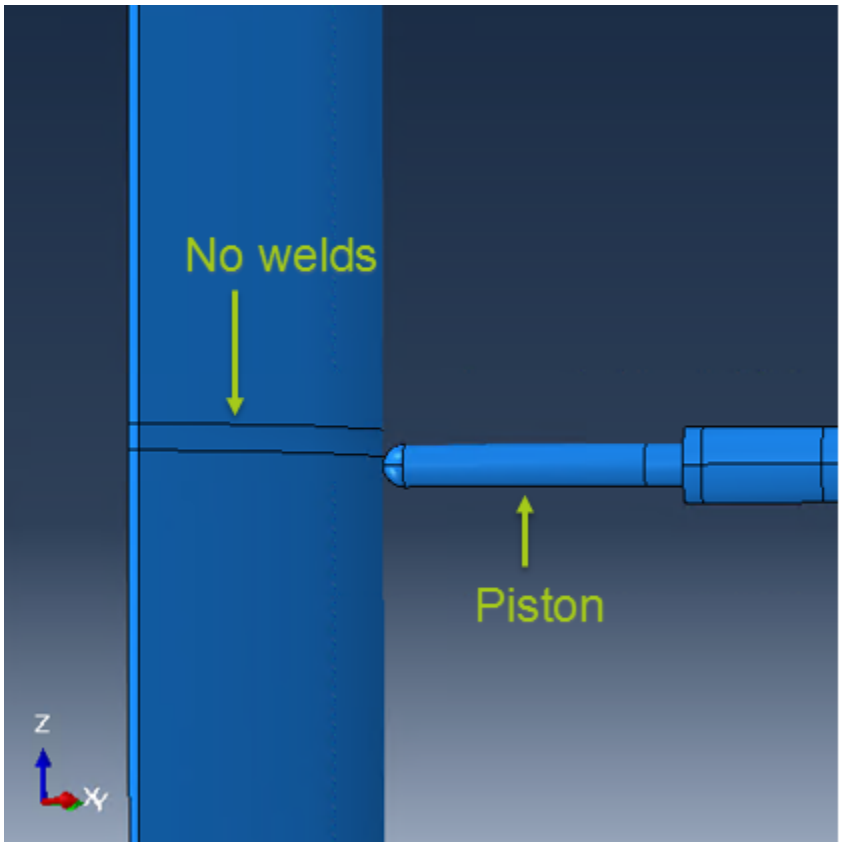

Figure 6.1: Piston contacts with smooth monopile surface in load case 1

This case will analyze the structure response when piston contacts with the smooth surface of monopile. Figure 6.2 shows the vertical displacement along time for the roller. It can be seen that the amplitude of displacement is very small, which is about 0.1 mm. The spectrum of the vertical motion is shown in Figure 6.3. Most spectral density is concentrated at frequency = 650 rad/s, which is the second natural frequency of the piston. That means, in this situation, the piston is disturbed by the stress wave, and then, when the stress wave disappears slowly, the motion follows the second eigenmode shapes. There is another peak at frequency = 23 rad/s. This corresponding period is similar to the time duration of the signal. This peak is caused by the mean offset of the signal during fast fourier transformation. The stress at cylinder is shown in Figure 6.4. The maximum stress is about 9×10^6 Pa, which is much lower than the yield stress.

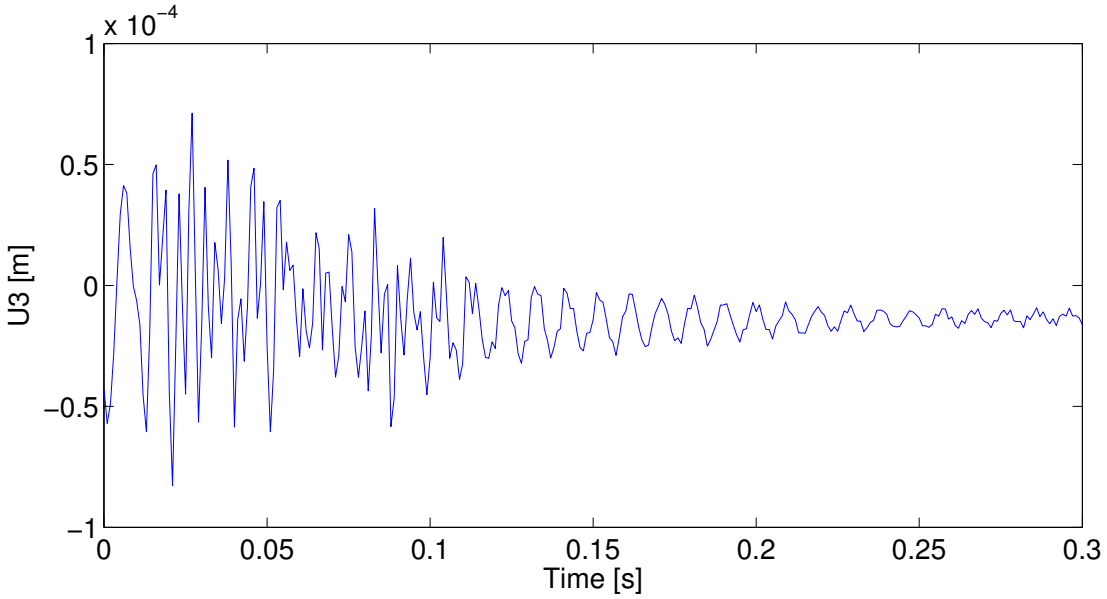

Figure 6.2: Vertical motion of roller (contacting with smooth surface of monopile)

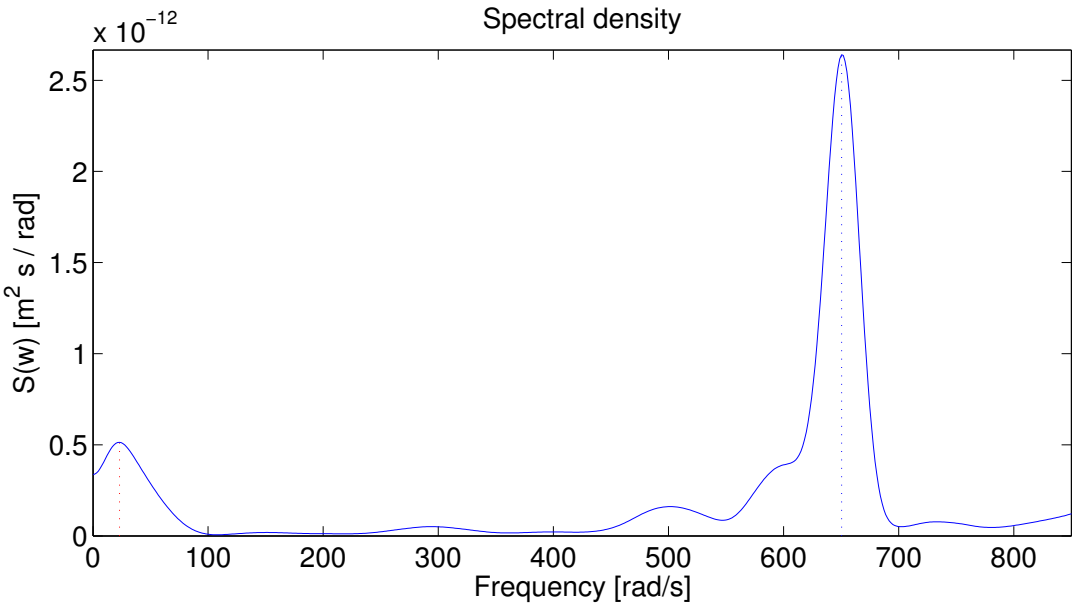

Figure 6.3: Spectrum for vertical motion of roller (contacting with smooth surface of monopile)

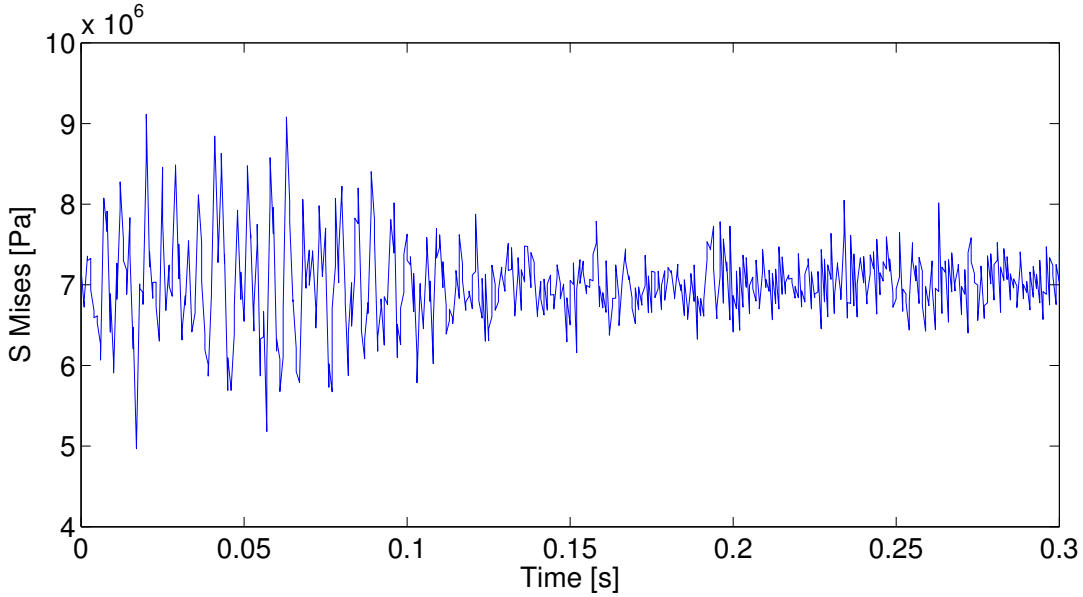

Figure 6.4: Mises stress at cylinder (contacting with smooth surface of monopile)

6.3 Case 2

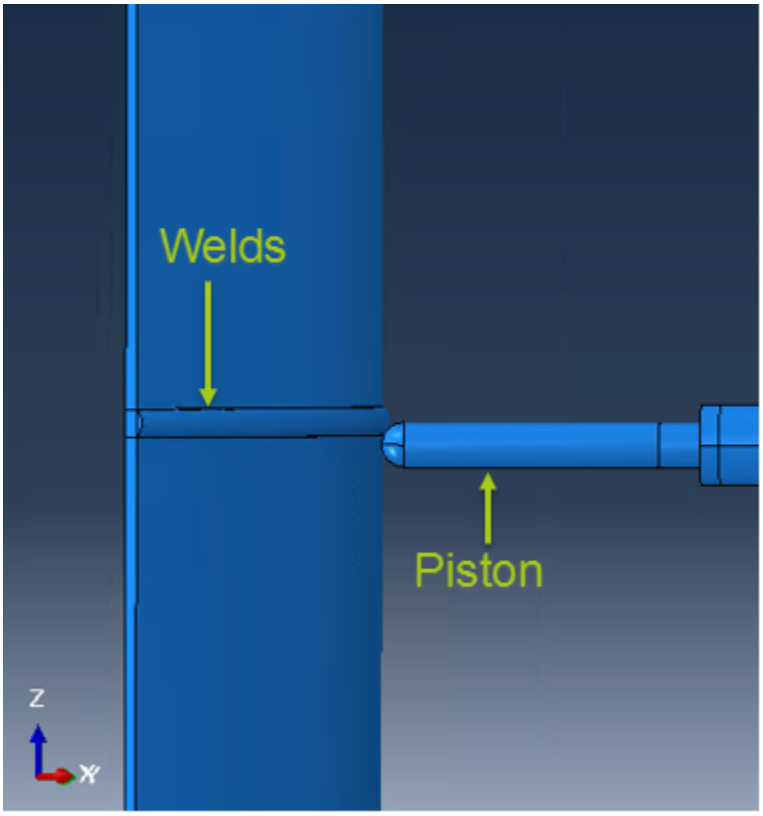

Figure 6.5: Piston contacts with welds in load case 2

When the piston collides with the welds, the displacement of the piston is shown in Figure 6.6. It can be seen that the motion of the piston follows the motion of monopile. It moves downward by several jerks. The signal for the displacement has a large mean offset from original point. This will generate a redundant peak value in spectrum with very large amplitude, which will make it difficult to read other peak values. So, the signal used for fast fourier transformation in this situation is the original signal minus a mean value signal (like the rigid body motion in section 6.1). The adjusted spectrum for the vertical motion of the piston is shown in Figure 6.7. This spectral density peak is very wide, and the second natural frequency of piston is included in its range. Whether resonance occurs in this situation will be discussed in case 6. The largest peak of the spectral density is concentrated at frequency = 540 rad/s, which is different from the second natural frequency of piston-cylinder assembly. This is caused by the stress wave propagation in the monopile. The incident stress wave passes by a point, then the reflected stress wave come

across the point again, which forms a period of excitation load. In this case, the length for the stress wave passes two times at the welds is 60 m. The corresponding frequency is:

$$f_{case2} = \frac{2 \cdot \pi \cdot C_{0,steel}}{L_{case2}} = 541.7 \qquad \text{[rad/s]} \tag{6.1}$$

This excitation frequency matches the peak spectral density in Figure 6.7. For other small peaks in the spectrum, it is difficult to distinguish whether they are caused by structure motion or by the process of reducing mean offset, so they are not discussed here.

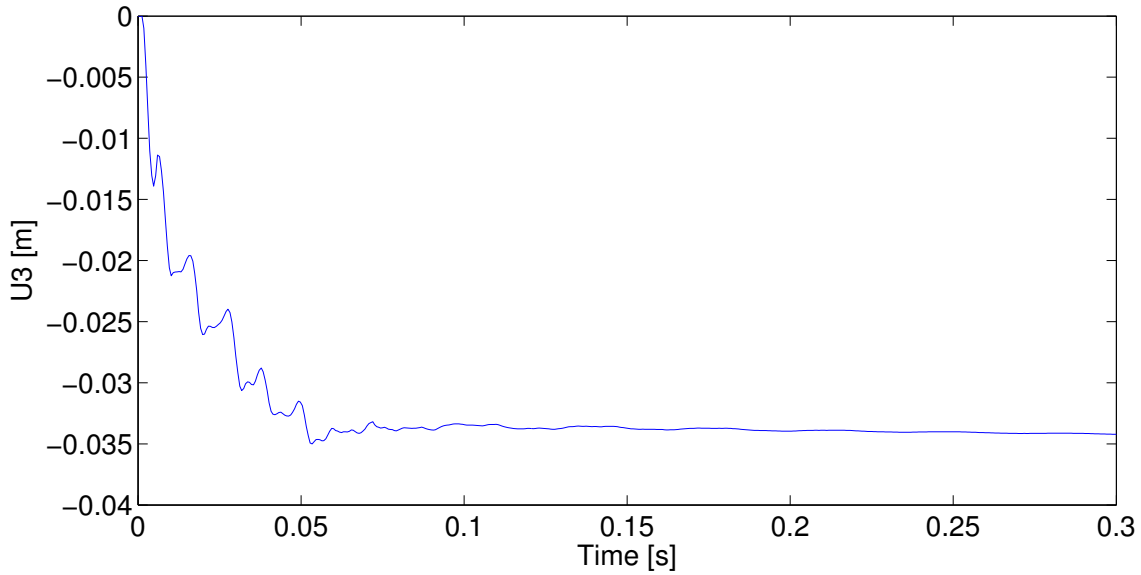

Figure 6.6: Vertical motion of roller (contacting with the welds)

Figure 6.8 shows the stress in the piston and cylinder. The stress in the cylinder is much smaller than the yield stress. But, some of the peak stress value in piston reaches the yield stress. Comparing with the stress when piston contacts with smooth surface, it is obvious to see that the stress when piston contact with welds is much larger. Yielding at the bottom contact point between piston and cylinder is very likely to occur.

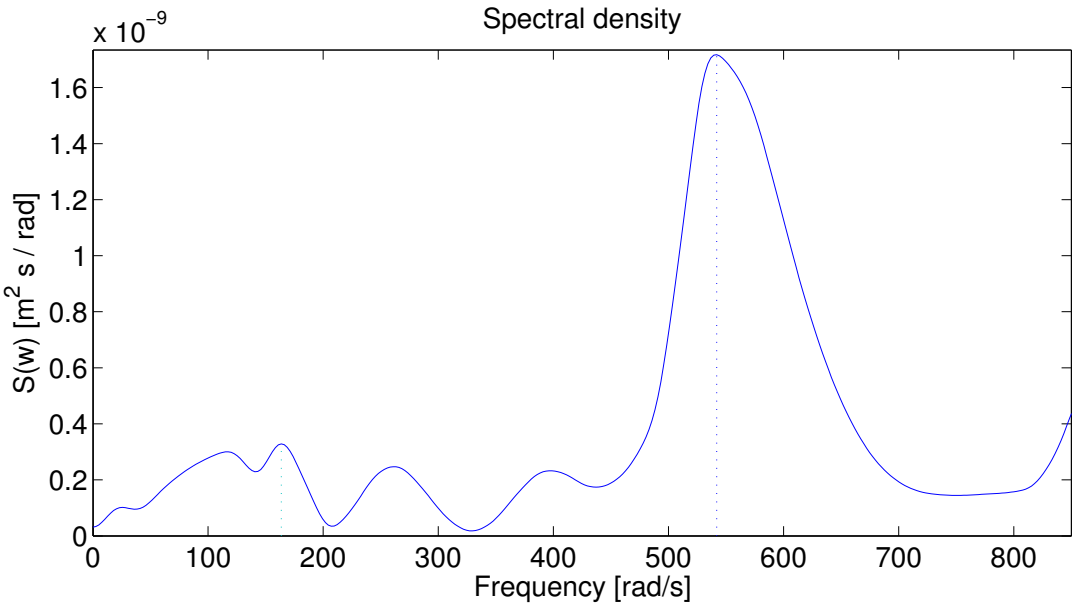

Figure 6.7: Spectrum for vertical motion of roller (contacting with the welds)

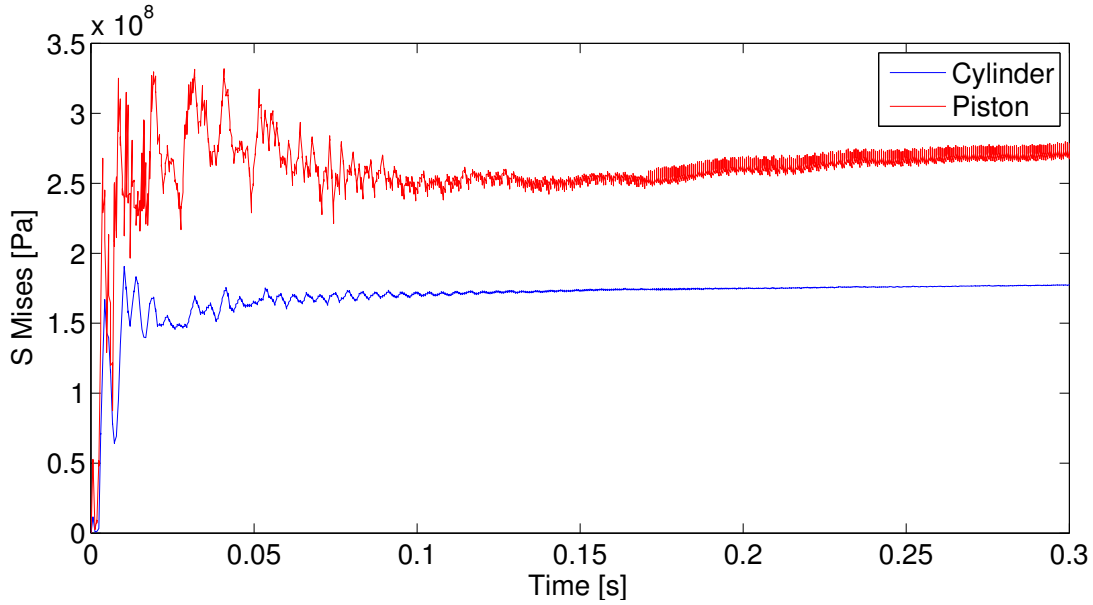

Figure 6.8: Mises stress at cylinder and piston (contacting with the welds)

6.4 Case 3

From above calculation, it can be seen that the piston's motion follows the welds's motion, which means that the welds does not go over the piston. The piston is pressed by the welds. So, cal-

culating just one stroke of the hammer is not enough for analyzing the whole colliding process. This case will compare the piston response for different stroke times.

In this case, the stroke time is 6. The time interval between two stroke is 0.1 s. Other initial conditions are the same with case 2.

Figure 6.9 shows the vertical displacement of the piston and welds for stroke number = 6. It can be seen that the piston keeps moving downwards during hammering process. Once the hammer load is applied, the piston vibrates in a large amplitude at first, then it gradually becomes stable and eventually standing still at a certain position. The total displacement caused by one single stroke decreases from the first stroke to the last stroke.

Because of the geometry of welds and piston, the vertical displacement of the piston should be larger than the vertical displacement of the welds. This can be seen in the first four strokes in Figure 6.9. But in the last two strokes, the vertical displacement of piston is smaller than the vertical displacement of welds, because the piston is gradually passing the welds.

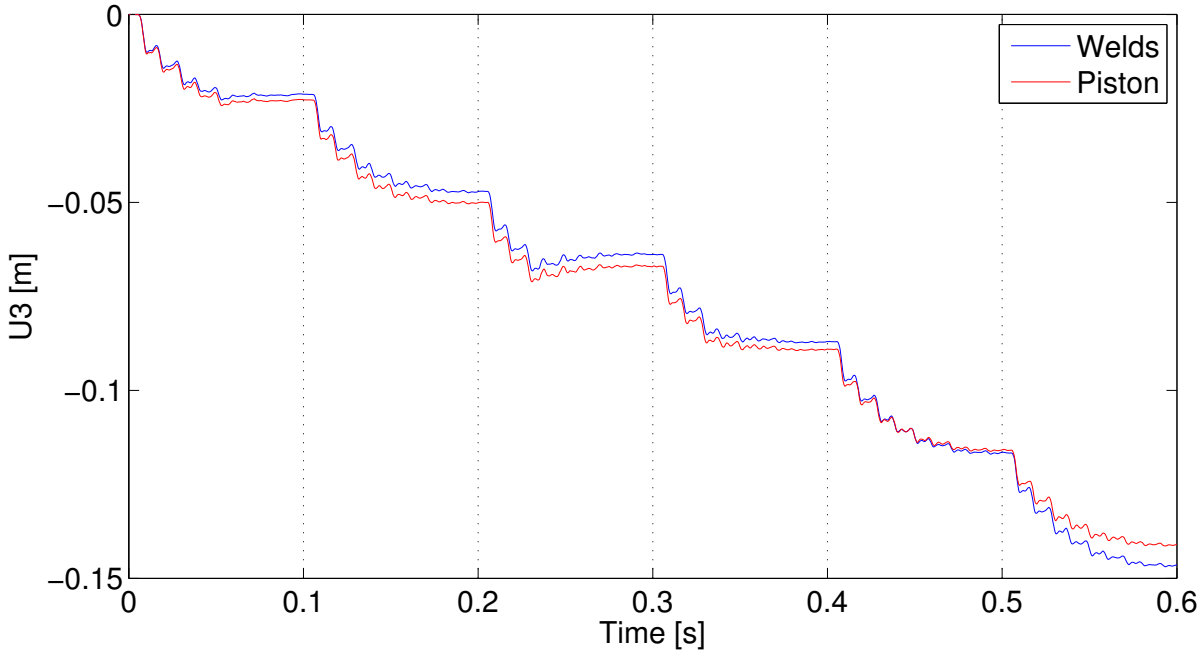

Figure 6.9: Vertical displacement of piston and welds for stroke number = 6

Figure 6.10 shows the horizontal displacement of piston and welds. It can be seen that the horizontal displacement of the welds is very small, and the disturbance is mainly caused by stress wave. The compressive stress wave causes strain in vertical direction. Due to Poisson ratio, the

vertical strain causes horizontal strain.

The horizontal displacement of the piston is relatively large. It increases with each stroke. During the piston passing the welds, it moves following the geometry of welds. So, the more piston passes welds, the farther it is compressive against the monopile. According to the Figure 6.10, the piston has been displaced 12 mm far away from monopile by welds. The capping of the welds is 20 mm, so it still does not pass the welds entirely. But, it is enough for analyzing the maximum stress in the gripper because the following geometry of the welds is more smooth than before and it will not cause larger stress than before.

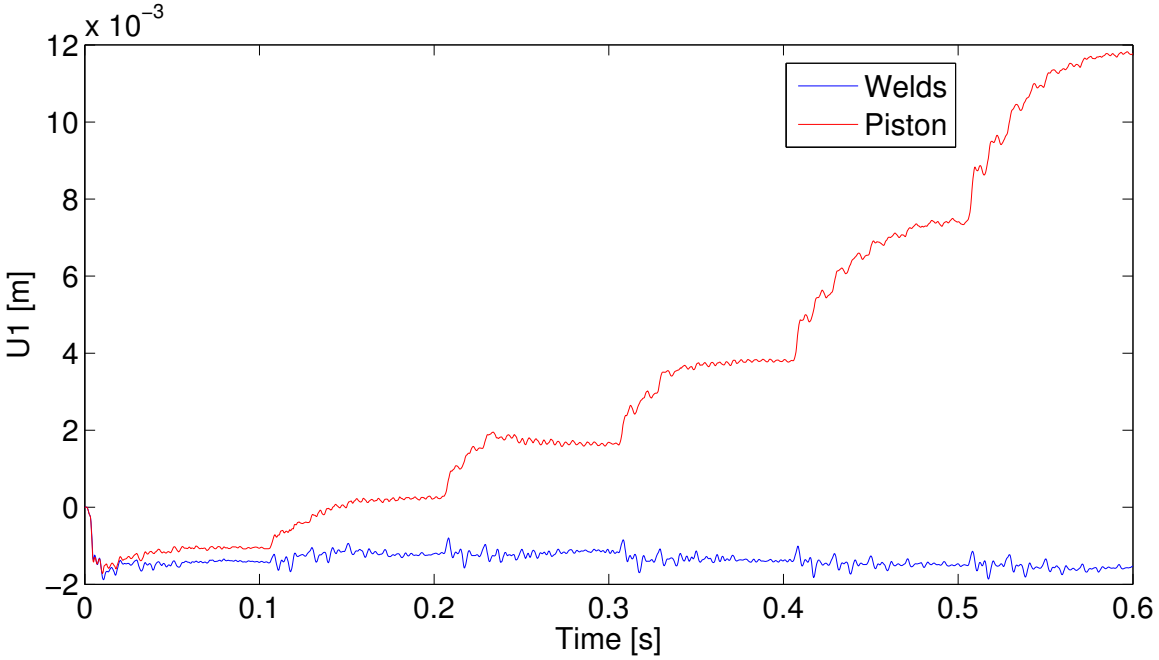

Figure 6.10: Horizontal displacement of piston and welds for stroke number = 6

Figure 6.11 shows the mises stress in the piston and cylinder. It can be seen that the mean stress will first increase then decrease with the increasing of the stroke number. The maximum stress occurs when the welds second strike the piston.

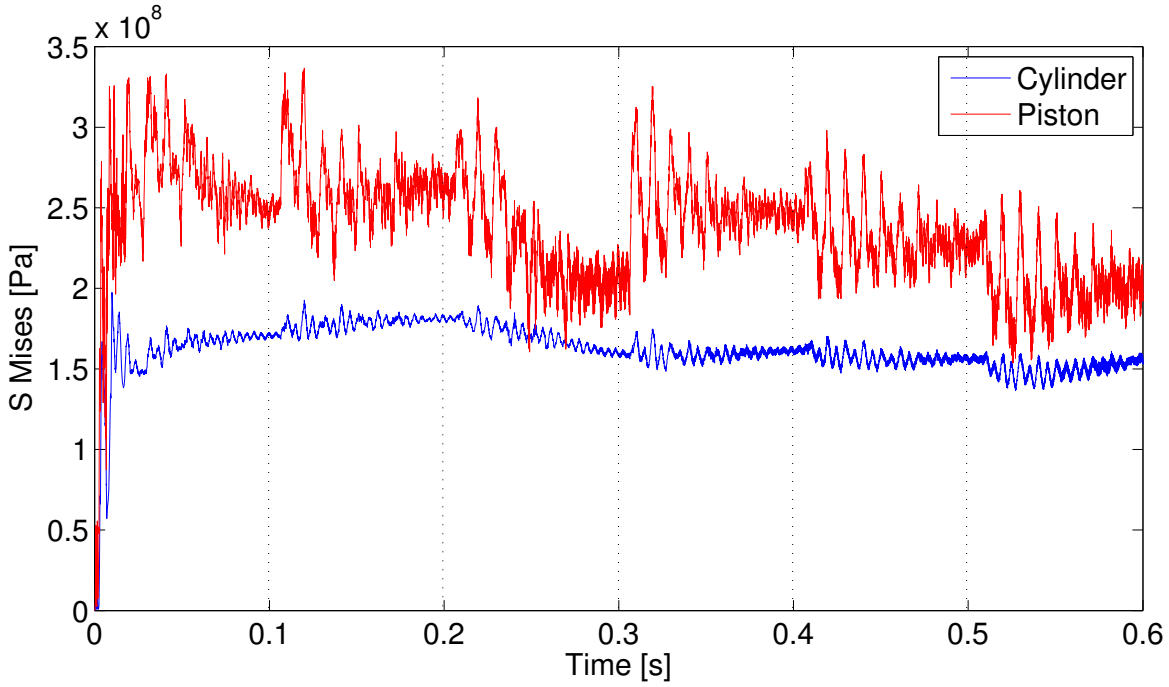

Figure 6.11: Mises stress in the piston and cylinder for stroke number = 6

6.5 Case 4

This case will analyze the stress in hydraulic cylinder for two different initial penetration depth:

- initial penetration depth: 10 m,
- initial penetration depth: 20 m.

The number of stroke is 3. The hammer drop energy used for 10 m initial penetration depth is the same with case 3. The hammer drop energy used for 20 m initial penetration depth is 600 kJ, otherwise the monopile displacement will be very small and large number of stroke should be simulated. Other initial conditions are the same with case 3.

Figure 6.12 shows the vertical displacement of piston for 10 m and 20 m initial penetration. The amplitude of vertical displacement of piston for 10 m initial penetration is less than which for 20 m initial penetration. The large soil resistance in 20 m initial penetration reduces the depth of pile penetration. The piston follows the motion of monopile, so it has smaller vertical displacement when monopile goes deeper.

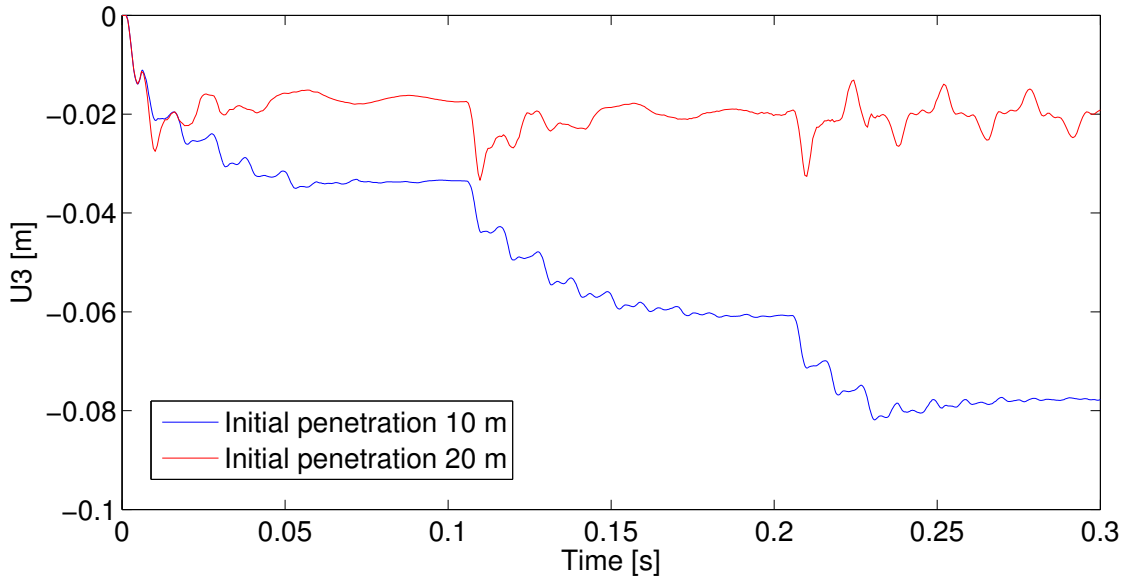

Figure 6.12: Vertical motion of roller for 10 m and 20 m initial penetration

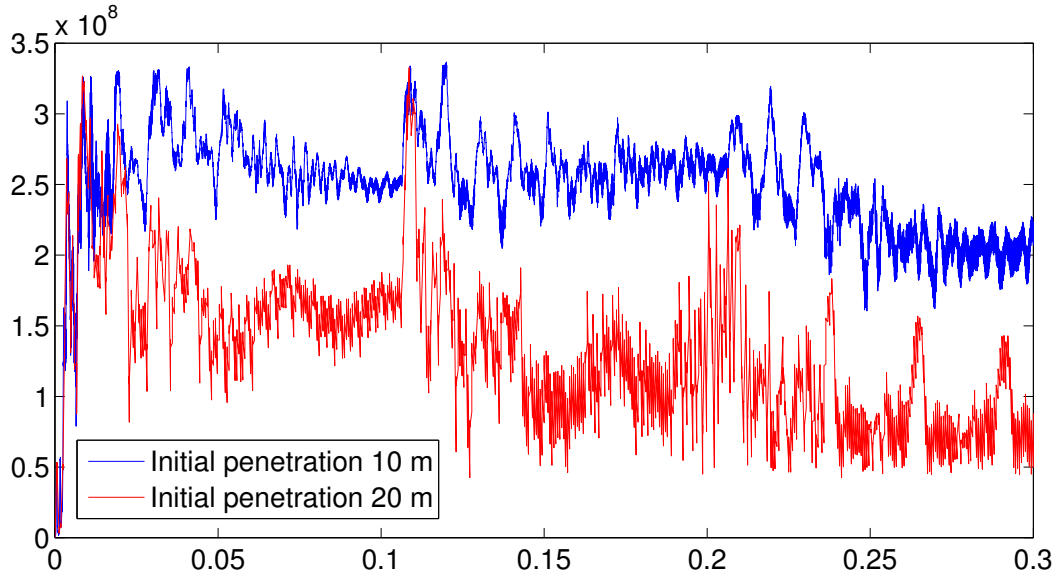

Figure 6.13: Mises stress at piston for 10 m and 20 m initial penetration

Figure 6.13 shows the mises stress in the piston for 10 m and 20 m initial penetration. It can be seen that, in general, the stress for 10 m initial penetration depth is larger than which for 20 m initial penetration depth. But, when the hammer load just acts on the monopile (Time = 0.1 s, 0.2 s, 0.3 s), some peak value of the stress for 20 m initial penetration equals to which for 10 m initial penetration. It can be seen in both curve that the stress induced by the first stroke is

larger than which induced by second and third stroke.

So, no matter what initial penetration depth is, the first stroke on the piston can induce the maximum stress. The mean stress can be effected by initial penetration depth. The deeper a initial penetration depth, the less mean stress occur in the piston.

6.6 Case 5

This case will analyze the stress in hydraulic cylinder for two different thickness of welds:

- welds' thickness: 20 mm
- welds' thichness: 10 mm

Figure 6.14 shows the vertical motion of the roller for 20 mm and 10 mm welds' thickness. It can be seen that changing the welds' thickness from 20 mm to 10 mm, the displacement of piston decreases largely and it is not perfectly follow the motion of gripper.

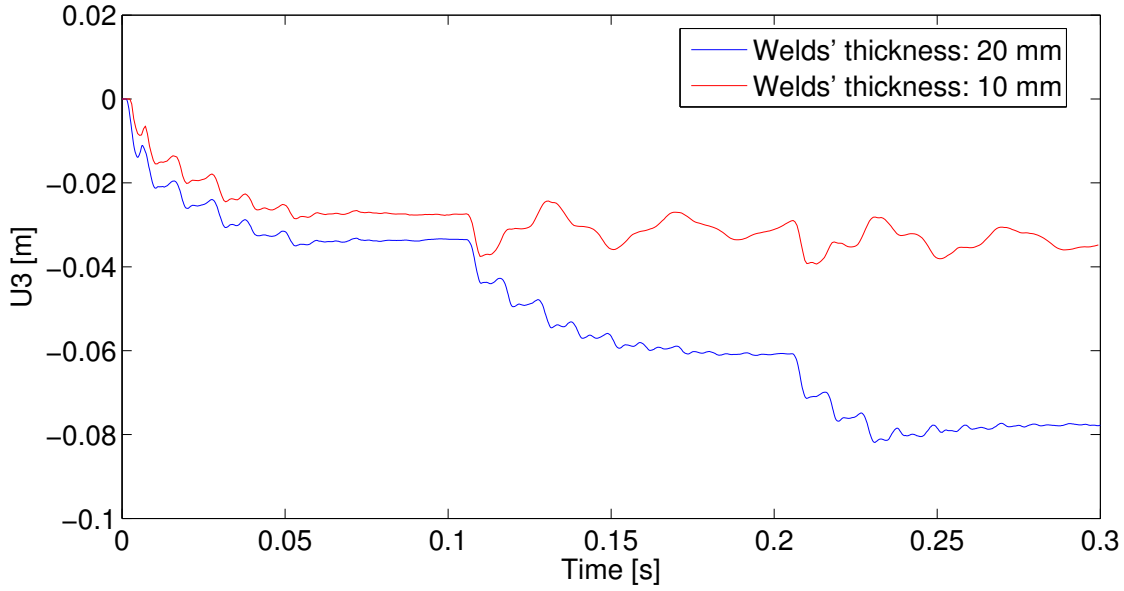

Figure 6.14: Vertical motion of roller for 20 mm and 10 mm welds' thickness

From Figure 6.15, it can be seen that at the first stroke, the stress in the piston for welds' thickness = 10 mm is almost the same with which for welds' thickness = 20 mm. For the second and third stroke, the mean stress in the piston for 10 mm welds' thickness is smaller and

the maximum stress is similar with which for 20 mm welds' thickness. So, changing the welds' thickness can influence the mean stress in the piston for one stroke, but it can not change the maximum stress.

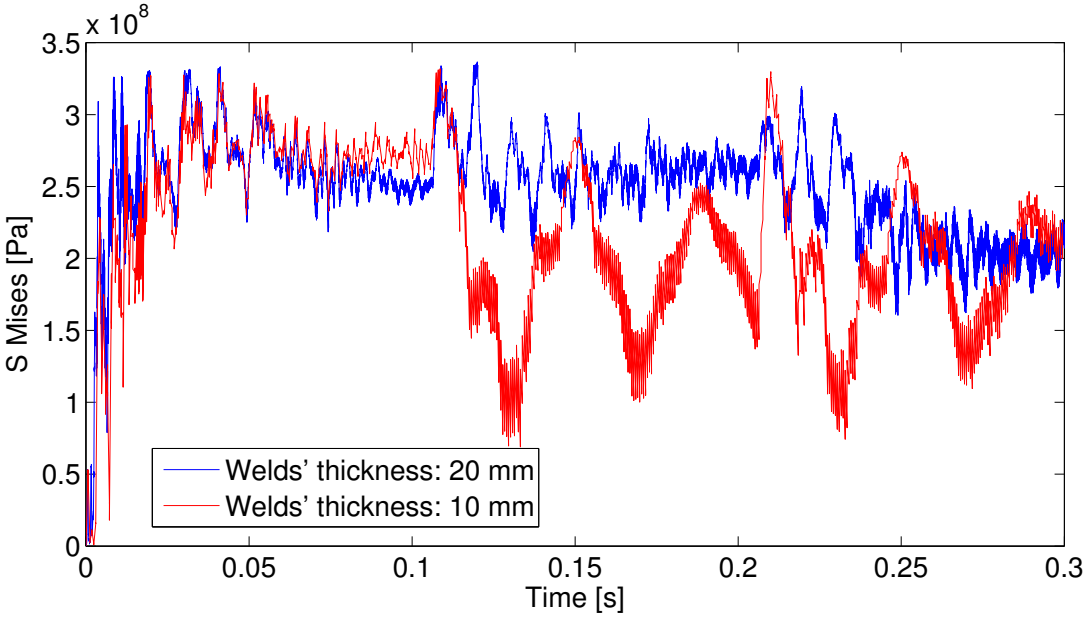

Figure 6.15: Mises stress of piston for 20 mm and 10 mm welds' thickness

6.7 Case 6

This case will analyze the structural response of different hammer drop energy:

- hammer drop energy: 200 kJ
- hammer drop energy: 600 kJ

Figure 6.16 shows the displacement of piston for 200 kJ and 600 kJ hammer drop energy. It can be seen that the displacement for one stroke for 600 kJ hammer drop energy is larger than which for 200 kJ hammer drop energy. From Figure 6.17, the maximum stress in piston for 600 kJ hammer drop energy is slightly larger than which for 200 kJ hammer drop energy for the first two stroke, but it is significantly larger than the latter in the third stroke.

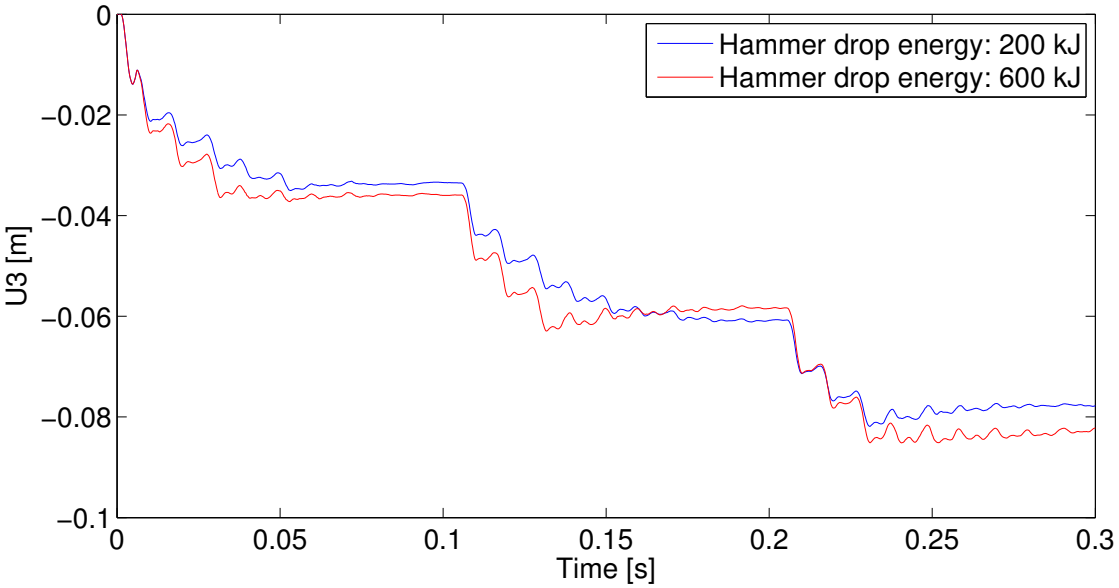

Figure 6.16: Vertical displacement of piston for 200 kJ and 600 kJ hammer drop energy

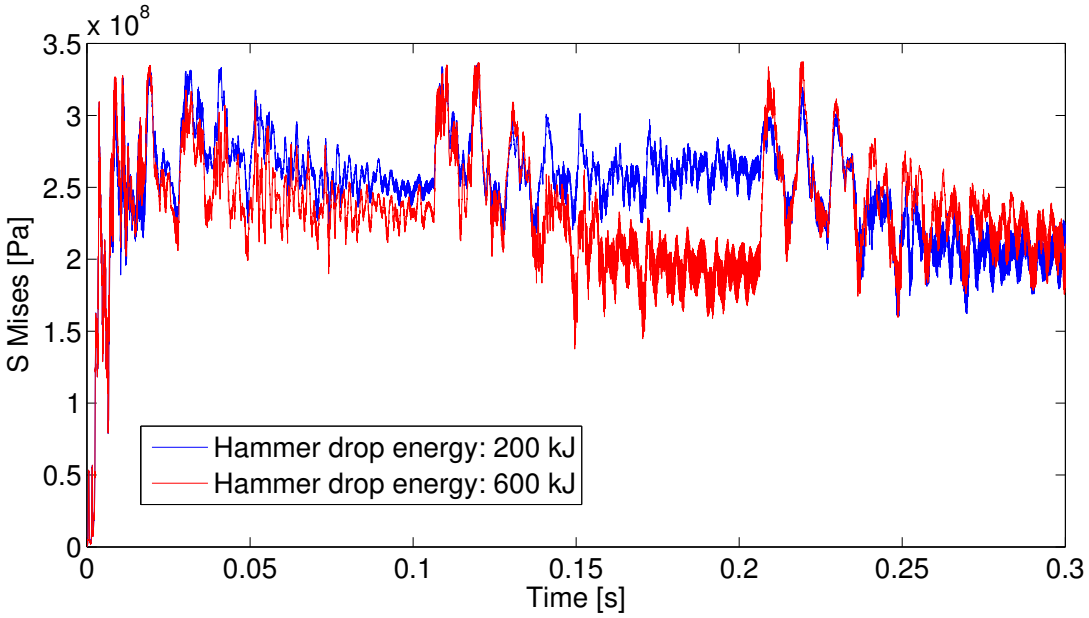

Figure 6.17: Mises stress of piston for 200 kJ and 600 kJ hammer drop energy

6.8 Case 7

This case will analyze the effect of changing environmental load:

- environmental load: 400 kN

- environmental load: 300 kN

Figure 6.18 shows the vertical displacement of the piston. It can be seen that, by decreasing the environmental load, the vertical displacement of the piston is decreasing. When decreasing the load applied to compress the piston toward monopile, the motion of piston does not follow the motion of monopile perfectly and self-vibration is a more important motion than forced vibration, shown in Figure 6.18 between 0.25 s to 0.3 s.

Figure 6.19 shows the mises stress of piston for 400 kN and 300 kN environmental load. From the first thought, it seems that decreasing the environmental load can reduce the stress in piston. But in the real case, the stress for 300 kN environmental load is larger than which for 400 kN environmental load. So, decreasing the environmental load can not effectively decrease the stress in gripper.

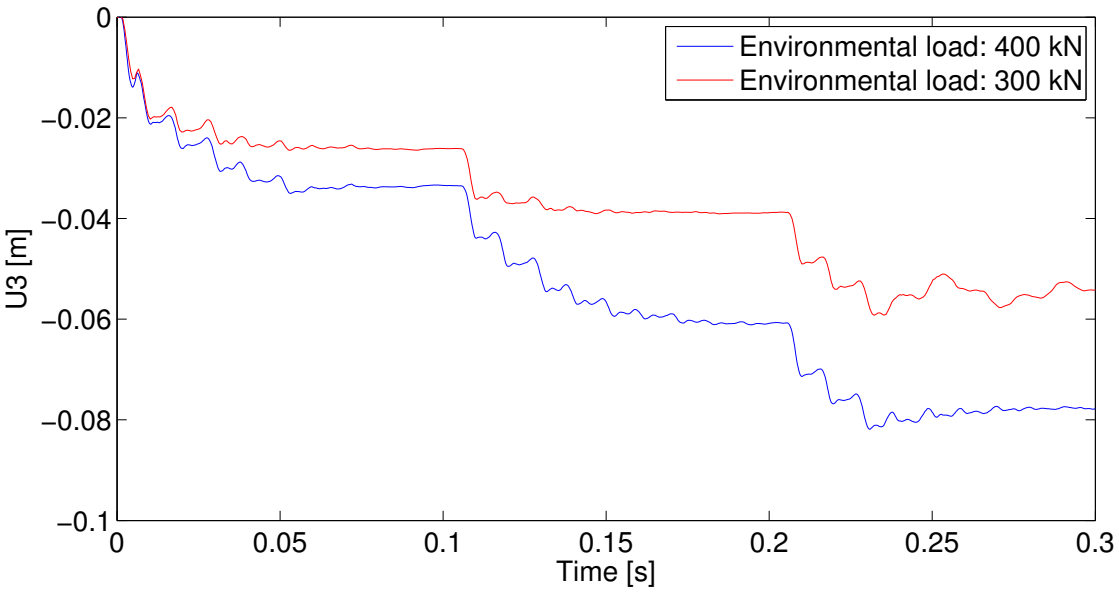

Figure 6.18: Vertical displacement of piston for 400 kN and 300 kN environmental load

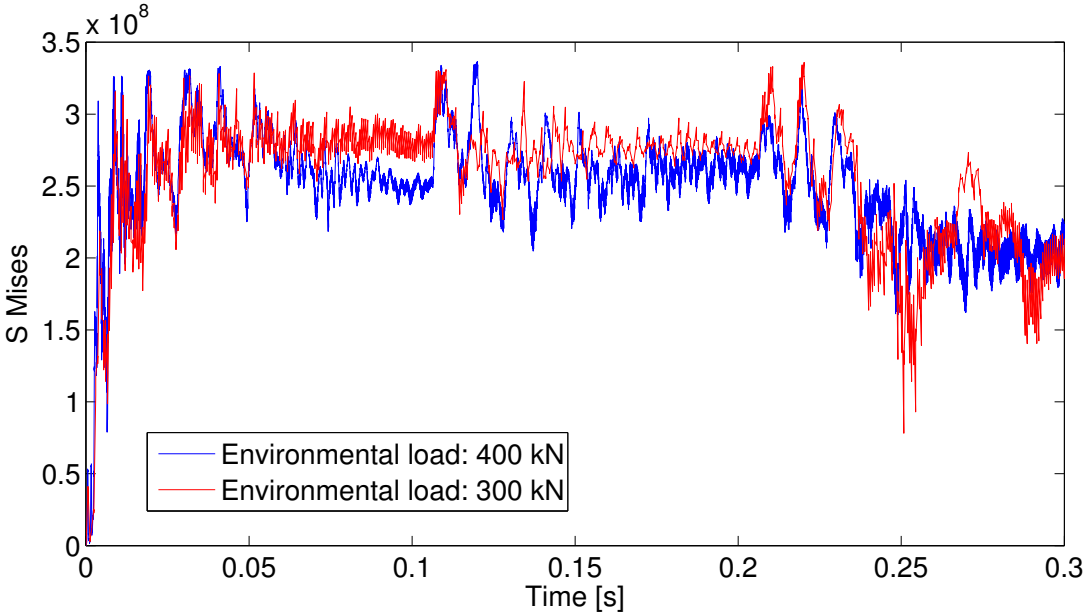

Figure 6.19: Mises stress of piston for 400 kN and 300 kN environmental load

6.9 Case 8

This case will analyze the effect of resonance.

First, the natural period of the piston-cylinder assembly is shown in the second row of Table 6.2. The distance which a stress propagates in a steel pile during the natural period (L_n) is shown in the forth row of Table 6.2. Half way of above distance ($L_{n,1/2}$) is shown in fifth row of Table 6.2.

Table 6.2: Natural frequency and period for piston-cylinder assembly

Mode No.	Natural frequency [Hz]	Natural period [s]	L_n [m]	$L_{n,1/2}$ [m]
Mode 1	70.62	0.0142	73.44	36.72
Mode 2	104.76	0.0095	49.13	24.57
Mode 3	169.51	0.0059	30.60	15.30
Mode 4	206.64	0.0048	25.03	12.52
Mode 5	267.35	0.0037	19.35	9.67
Mode 6	275.97	0.0036	18.74	9.37

The second natural frequency has the largest influence on the motion of piston. When the gripper is placed as the left figure in Figure 6.20, the incident and reflected stress wave will excite the second natural frequency. Resonance will happen in this situation. The displacement and stress in the piston-cylinder assembly will increase largely. So, this is the case which should be

highly focused on during monopile installation process. The eigenmode shape for the first and third natural frequency is suitable for horizontal motion of the piston-cylinder assembly, so it is not involved in the analysis. The maximum piston deformation for third eigenmode shape is located inside the cylinder. The displacement of roller does not appear in this eigenmode shape, so it is not concerned in this analysis. The higher motion have very short $L_{n,1/2}$. In this case, the water depth is above 15 m so the gripper can not be placed 9 m above the pile toe. When the gripper is placed 9 m below the pile head, which means the installation procedure is almost done, the gripper is retrieved from the monopile.

In order to see the effect of resonance, a resonance model and a non-resonance model are built for calculation. The initial conditions in this two model are all the same except for the height of the gripper. In the resonance model, the gripper is located at 25 m above the pile toe to excite the second natural frequency. In the non-resonance model, the gripper is placed 13.2 m below the pile toe to avoid this natural frequency.

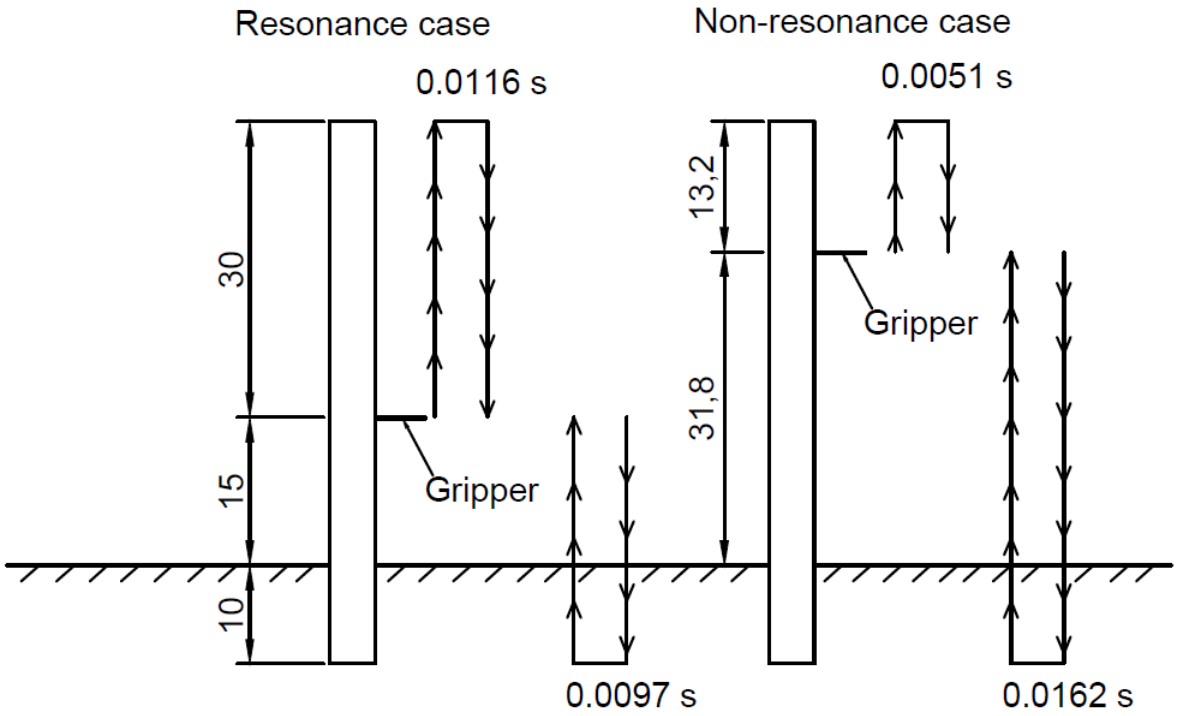

Figure 6.20: Description of resonance load in monopile hammering process

Figure 6.21 shows the vertical displacement of piston and monopile for resonance and non-resonance model. It can be seen that the piston motion for non-resonance model does not

follow the motion of monopile any more. It separate with the welds right after each stroke. After the third stroke, the piston totally disconnected with the monopile and doing free vibration. On the contrary, the motion of piston for resonance model follows the motion of monopile. According to the stress wave theory, the motion of the monopile follows the stress wave. So, the piston can be regarded as bearing an excitation in its natural frequency. The amplitude of displacement of the piston in both case is obviously shown in this figure.

Furthermore, it can be seen in Figure 6.21 that the displacement of monopile decrease in non-resonance model. Looking at the first stroke, the motion for both model are the same at the beginning. Then a small different gradually appears. In the second stroke, the different between the two model is significantly enlarged. But, in the third stroke, the difference remains the same. A guess is made for explanation of this phenomena: the collision between welds and piston weakens the stress wave, and this weakening effect is more significant in non-resonance case than resonance case.

Figure 6.22 shows the Mises stress of piston for resonance and non-resonance cases. Obviously, the one for non-resonance case is much smaller than which for resonance case.

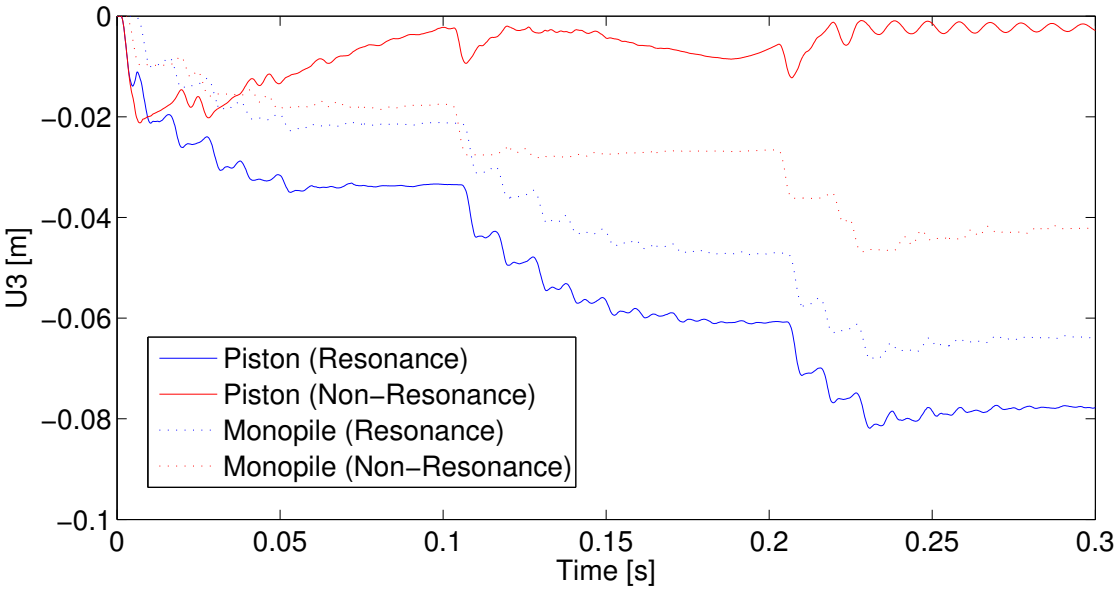

Figure 6.21: Vertical motion of roller and monopile for resonance and non-resonance cases

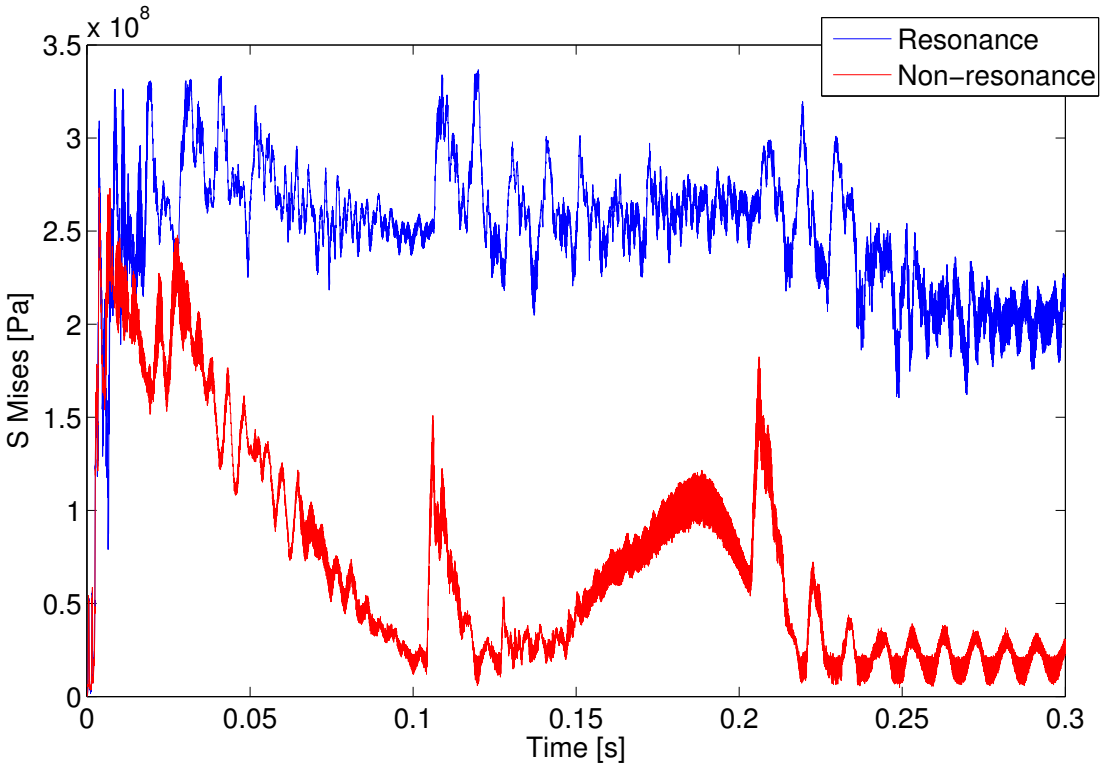

Figure 6.22: Mises stress of piston for resonance and non-resonance cases

Chapter 7

Conclusion

- During monopile installation, increasing the hammer drop energy will increase the soil penetration for the monopile for one blow. It will also increase the stress in the monopile. In order to accelerate the installation process as well as the structural reliability, the hammer drop energy should be optimized for different penetration depth.
- The stress wave propagation theory, the relationship between stress wave and partical velocity can be proved in ABAQUS finite element model. The stress wave theory is suitable for analysis of the monopile installation problem in ABAQUS.
- The gripper system is vulnerable when bearing lateral load. The most vulnerable point is the bottom contact point between piston and cylinder.
- When the piston does not collide with the welds, the stress in gripper device is very small and it vibrate freely. When the welds hit the piston, the piston will, at first, follow the motion of monopile. There will be large stress generated by the colliding load.
- The more deeper a monopile penetrate the soil, the less stress in piston will be generated by colliding load.
- With the increasing in monopile penetration depth, the mean stress in gripper device goes smaller.
- Decreasing the environmental load can not decrease the stress in gripper effectively.

- Changing the welds' thickness can influence the mean stress in gripper, but it can not change the maximum stress.
- Increasing drop energy can increase the maximum stress in gripper slightly.
- Due to stress wave reflection, resonance of the piston can take place. When there is resonance in the gripper structure, the displacement and stress are significantly enlarged.

Chapter 8

Future work

- The hydraulic liquid in the hydraulic cylinder is modelled as a spring in Abaqus model, which can not perfectly define the behavior of hydraulic liquid. It should have a more detailed study and finite element model.
- The soil resistance in this thesis is calculated by API standard for ultimate resistance. During monopile installation, the soil behavior is totally different from which in static condition. The change of pore pressure and soil deformation can influence the soil resistance largely. It is necessary to modify the soil resistance to a realistic condition.
- The effect of changing the geometry of welds and roller should be analyzed to see its influence on gripper stress.
- The roller is simplified as a semi-ball contacting with monopile surface without friction. In future work, a detailed model for the roller should be built to envolve the rotation.

Bibliography

[1] Det Norske Veritas. Design of offshore wind turbine structures. *Offshore Standard DNV-OS-J101*, 6:2004, 2004.

[2] Nishat Al Nahian. Structural analysis of the gripper connection during monopile installation. Master's thesis, NTNU, 2016.

[3] A. Verruijt. Soil mechanics. *Delft University of Technology*, 2012.

[4] Lin Li. Dynamic analysis of the installation of monopiles for offshore wind turbines. 2016.

[5] I Abaqus. Analysis user's manual volume v, prescribed conditions, constraints & interactions. *Journal of Biomedical Science and Engineering*, 6(11):898, 2008.

[6] P Arasaratnam, KS Sivakumaran, and MJ Tait. True stress-true strain models for structural steel elements. *ISRN Civil Engineering*, 2011, 2011.

[7] European Wind Energy Association et al. Pure power: wind energy scenarios up to 2030, 2008.

[8] Tomas Gintautas and John Dalsgaard Sørensen. Improved methodology of weather window prediction for offshore operations based on probabilities of operation failure. *Journal of Marine Science and Engineering*, 5(2):20, 2017.

[9] LEANWIND. Logistic efficiencies and naval architecture for wind installations with novel developments/key design parameters and criteria related to installation and maintenance vessels design; their layouts, crane operations and access systems. no. 614020, 2015.

[10] IHC. Ihc vremac cylinders cylinder catalogue 210 bar / 320 bar.

[11] Mark J Kaiser and Brian Snyder. Offshore wind energy installation and decommissioning cost estimation in the us outer continental shelf. *Energy Research Group LLC, Louisiana*, 2010.

[12] T Strandgaard and L Vandenbulcke. Driving mono-piles into glacial till. *IBCs Wind Power Europe*, 2002.

[13] Mark Randolph and Susan Gourvenec. *Offshore geotechnical engineering*. CRC Press, 2011.

[14] RP API. 2a-wsd. *Recommended Practice for Planning, Designing and Constructing Fixed Offshore Platforms-Working Stress Design*, 21, 2000.

[15] Lee Leon Lowery, Teddy James Hirsch, and T Edwards. Pile driving analysis-simulation of hammers, cushions, piles, and soil. 1900.

[16] Frank Rausche and George G Goble. Performance of pile driving hammers. *Journal of the Construction Division*, 98(co2), 1972.

[17] DV Issacs. Reinforced concrete pile formulas. *Transaction of the Institution of Engineers, Australia*, pages 312–323, 1931.

[18] EAL Smith. Tension in concrete piles during driving. *Journal Prestressed Concrete Institute*, 5:35–40, 1960.

[19] Hibbitt Karlsson and Sorenson. Abaqus/standard analysis user's manual, volume ii: Analysis. 6(11), 2008.

[20] Hibbitt, Karlsson, and Sorensen. *ABAQUS/standard User's Manual*, volume 1. Hibbitt, Karlsson & Sorensen, 2001.

[21] Charlotte Weisman. *Welding handbook*. American Welding Society, 1976.

[22] IACS No. 47–rev. 5 (2010). *Shipbuilding repair quality standard*.

[23] Hibbitt Karlsson and Sorenson. Abaqus/standard analysis user's manual, volume iv: Elements. 6(11), 2008.

Appendix A

Eigenmode shapes for piston-cylinder assembly

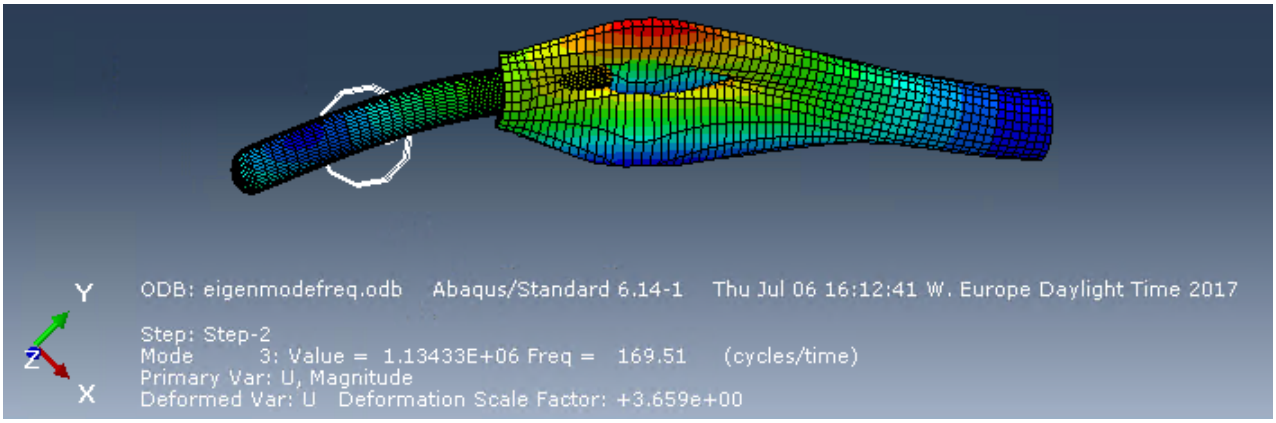

Figure A.1: Third eigenmode shape of piston-cylinder assembly

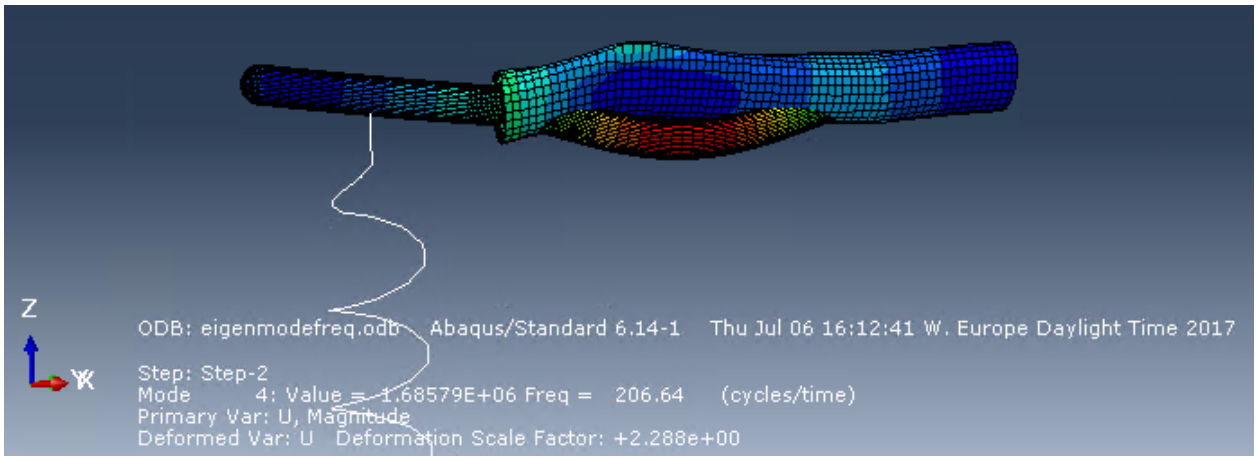

Figure A.2: Forth eigenmode shape of piston-cylinder assembly

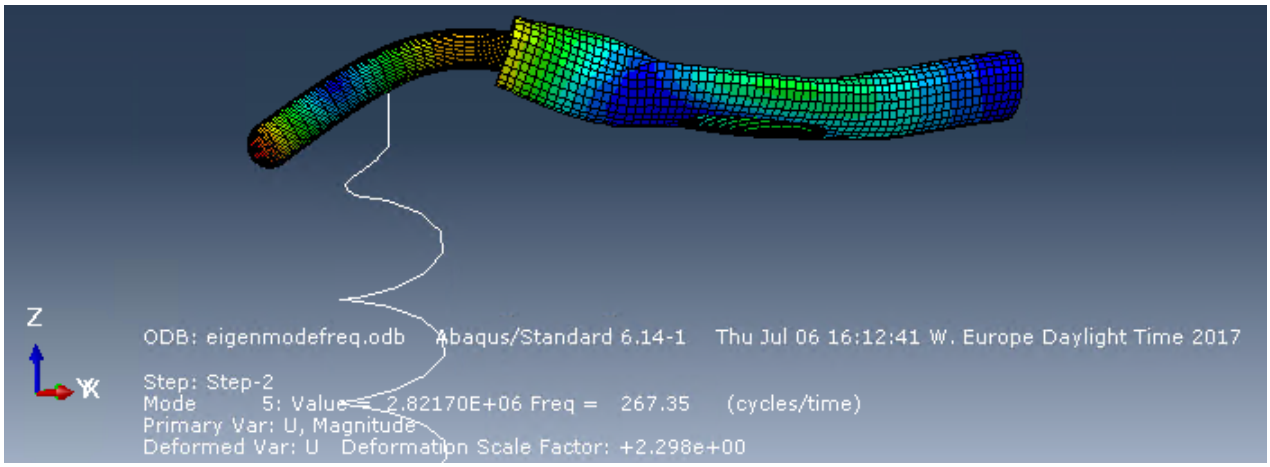

Figure A.3: Fifth eigenmode shape of piston-cylinder assembly

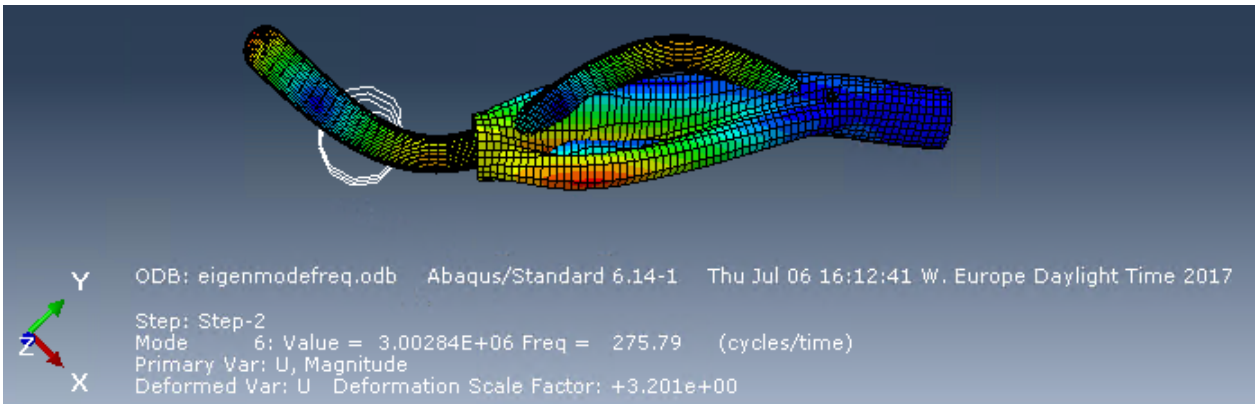

Figure A.4: Sixth eigenmode shape of piston-cylinder assembly

Appendix B

Eigenmode shapes for soil supported monopile

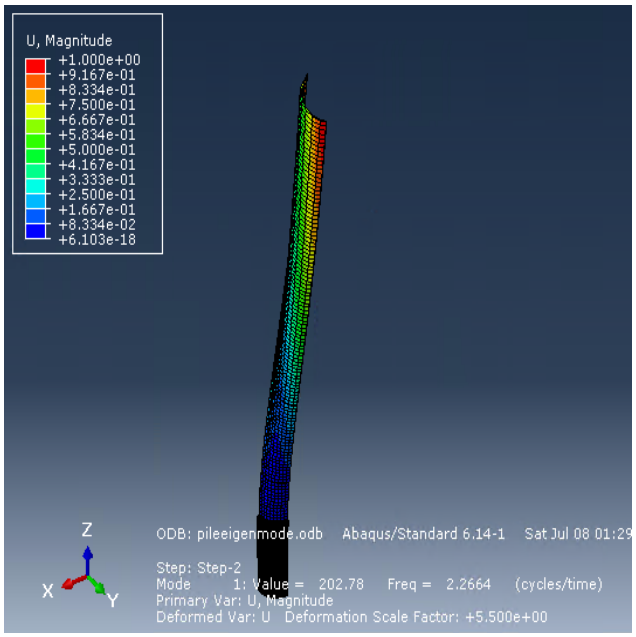

Figure B.1: First eigenmode shape for soil supported monopile

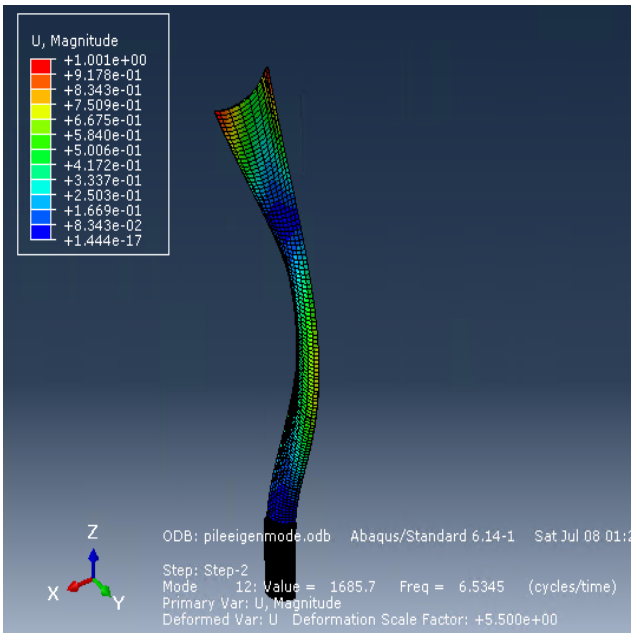

Figure B.2: Second eigenmode shape for soil supported monopile

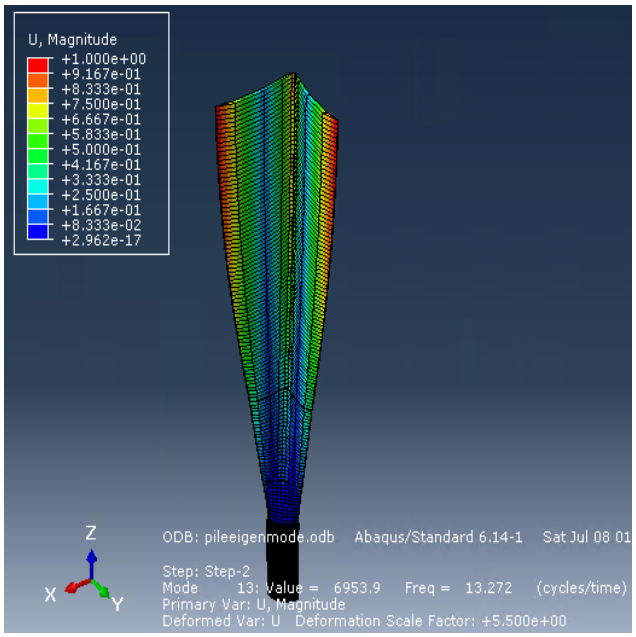

Figure B.3: Third eigenmode shape for soil supported monopile

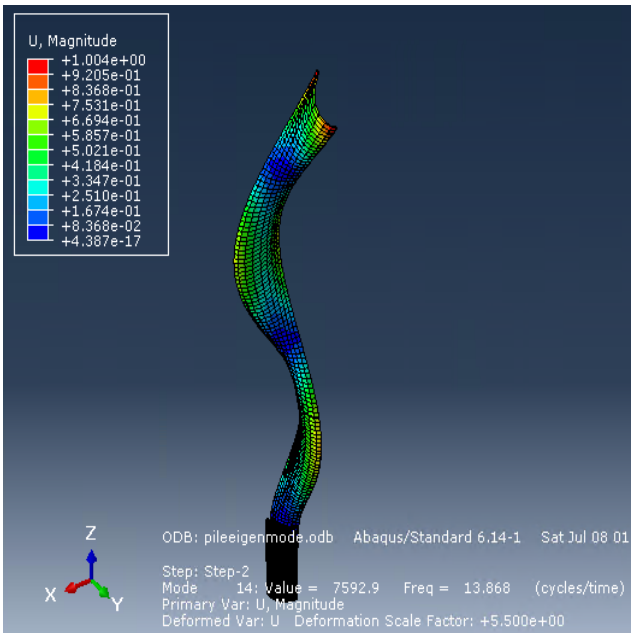

Figure B.4: Forth eigenmode shape for soil supported monopile

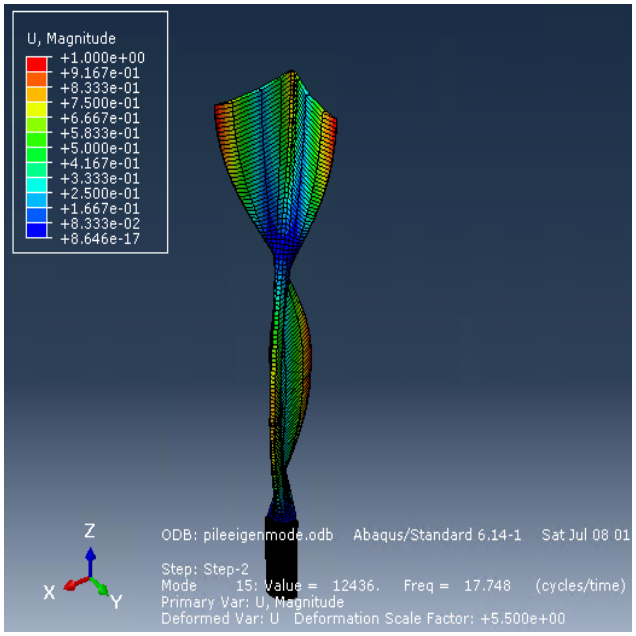

Figure B.5: Fifth eigenmode shape for soil supported monopile

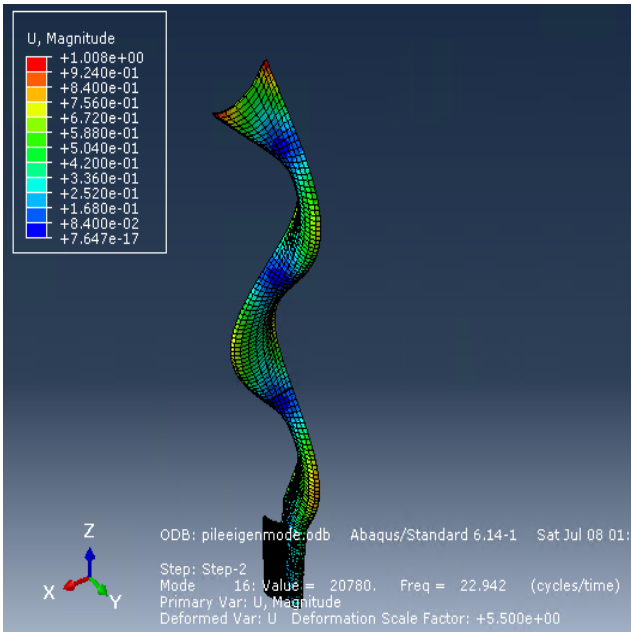

Figure B.6: Sixth eigenmode shape for soil supported monopile

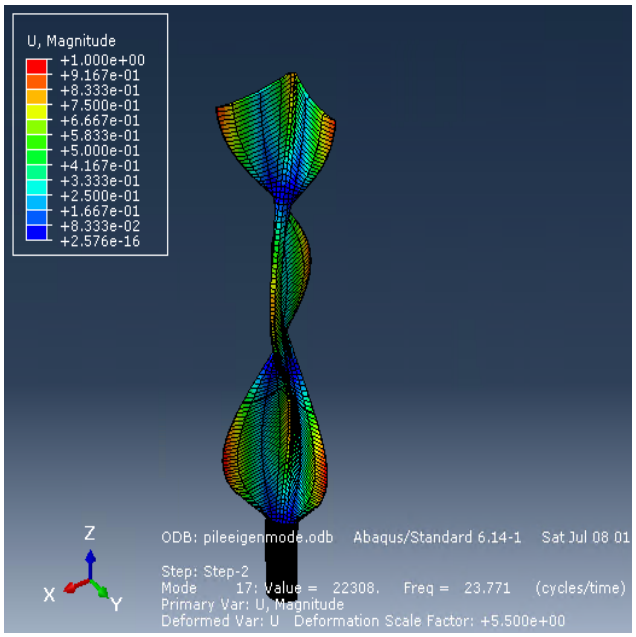

Figure B.7: Seventh eigenmode shape for soil supported monopile

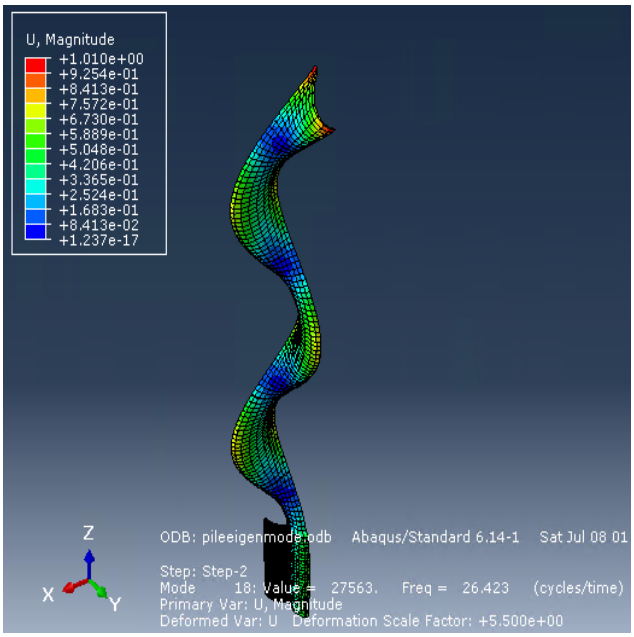

Figure B.8: Eighth eigenmode shape for soil supported monopile

Appendix C

Stiffness Calculation of the Square Arm

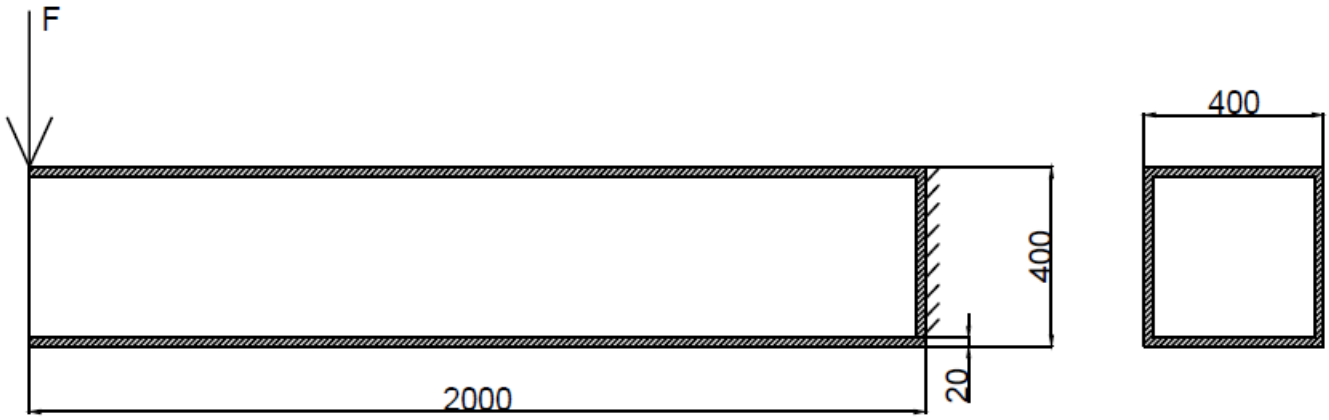

Figure C.1: Cross sectional view of support structure for piston

The maximum deflection of a cantilever beam can be derived as:

$$y = \frac{Fl^3}{3EI} \tag{C.1}$$

where,

F = applied load at the free end,

l = length of the beam,

E = Young's modulus,

I = second moment of inertia of the beam's cross sectional area.

For a square area, the I can be derived as:

$$I = \frac{b^4}{12} \tag{C.2}$$

where,

b = the breadth of the square area.

In this case, the beam is hollowed. So, the total second moment of inertia for the cross sectional area is: the second moment of inertia for the outer square I_{out} minus the second moment of inertia for the inner square I_{in}

$$I_{total} = I_{out} - I_{in} \tag{C.3}$$

Substituting the Eq. C.3 to Eq. C.1 and rearrange the equation, the relationship between the applied force and deflection can be derived as:

$$F = \frac{3E(I_{out} - I_{in})}{l^3} \cdot y = K_2 \cdot y \tag{C.4}$$

where,

K_2 = the vertical stiffness of the support structure.

Substituting the geometry parameters in Eq. C.4, the K_2 can be calculated:

$$K_2 = 4.89 \times 10^7 \qquad [\mathrm{N/m}] \tag{C.5}$$

Appendix D

Assembly of finite element model

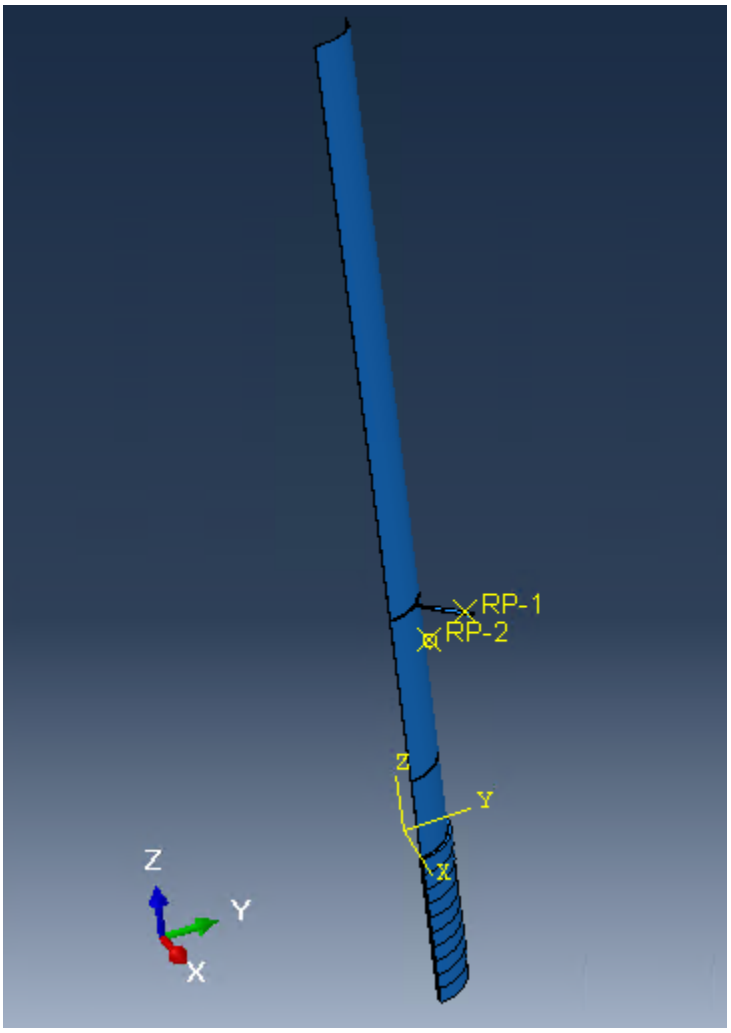

Figure D.1: Assembly of finite element model